Università degli Studi di Bologna

FACOLTÀ DI SCIENZE MATEMATICHE, FISICHE E NATURALI

Dipartimento di Astronomia

THE PARSEC SCALE PROPERTIES OF LOW POWER RADIO LOUD ACTIVE GALACTIC NUCLEI

DOTTORATO DI RICERCA IN ASTRONOMIA

XVI CICLO

Coordinatore Prof. GABRIELE GIOVANNINI

Tesi di Dottorato
di:

MARCELLO GIROLETTI

Relatore:
Chiar.mo Prof.

GABRIELE GIOVANNINI

QUESTA TESI E' STATA SVOLTA

NELL'AMBITO DELLE ATTIVITA' DI RICERCA

DELL'ISTITUTO DI RADIOASTRONOMIA

DEL CONSIGLIO NAZIONALE DELLE RICERCHE

(BOLOGNA)

Contents

Introduction

The properties of BL Lac objects are absolutely amazing at all wavelengths, from the extreme brightness temperature in the radio all the way through the electromagnetic spectrum, up to their incomparable emission at TeV energy. Besides the high brightness temperatures, the radio data present evidence for significant polarization and variability, and compact component in jets are often reported to move superluminally; optical radiation is also variable and strongly polarized, lacking significant spectral features; at higher frequency, variability is even larger, and X-ray spectra present a wide range of indexes; finally, the $\gamma-$ray data from EGRET (in the MeV/GeV domain) and from the Whipple observatory (above 100 GeV, up to 10 TeV) have revealed emission of extremely energetic photons, which contribute a major amount of the total emitted energy. Most of the properties of BL Lacs can be ascribed to non-thermal processes, such as synchrotron emission and Inverse Compton scattering. Both processes require the presence of relativistic particles, possibly located in a set of "twin" jets, originating in a compact region around a supermassive black hole.

While many of the above mentioned properties are unique to the BL Lac class, there are others that are clearly shared by a number of other Active Galactic Nuclei (AGN); moreover, since orientation can affect the observed behaviour of any non isotropic object, it is possible that different observational properties can proceed from the same intrinsic mechanism. This is at the base of *unified schemes*, a promising approach to the puzzling and amazingly large range of observed properties of Active Galactic Nuclei: radio loud or radio quiet, presenting narrow or broad emission lines, remarkably steady in flux density or rapidly variable, etc. For example, the broad emission lines present in Seyfert galaxies of type 1 would be present also in Seyfert 2, but obscured to transverse lines of sight by an absorption circumnuclear torus; taking advantage of scattering, images in polarized light have revealed these lines also in Seyfert 2, supporting this interpretation. As for radio galaxies, orientation effects would be responsible for the appearance, under a small viewing angle, of quasars and blazars (BL Lacs and FSRQ); in particular, the latter would be the aligned counterpart of low power edge dimmed Fanaroff-Riley I radio galaxies (FR I) and the former would be related to more powerful, edge brightened FR II. This scheme is meeting with success; however, there are a number of problems that need to be solved. For example, there are a few BL Lac objects showing a large total radio power, more easily comparable to that of FR II than of FR I. On the other hand, there are objects of very low total power, whose properties are poorly known. As a matter of fact, we need more observations to improve the current view on the unification of AGN and the understanding of their physics.

In particular, the situation is worsened for BL Lacs because of the paucity of data available at all wavebands. In fact, BL Lacs are probably the rarest and most extreme objects among AGN, and their physical properties are difficult to understand; furthermore, the incidence of BL Lacs in large, low-frequency surveys has historically been extremely low, mainly because of their flat spectrum; the small viewing angle makes also the BL Lacs naturally less numerous than radio galaxies, although Doppler boosting somehow compensates for this effect. Therefore, we need a sizable sample to answer a number of questions: what are the typical Doppler factors for BL Lacs? how small are the angles to the line-of-sight? what is the real difference between Low and High frequency peaked BL Lacs (LBL and HBL, respectively)? what is the parent population? do FR IIs really contribute to it? and what happens on the weak end of their luminosity function? how is the energy extracted from the central black hole?

So far, a richness of information has been obtained from the 1 Jy sample, which is one of the few relatively large (37 objects) and complete samples. The sample has been investigated in different wavebands, and it is the only BL Lac sample possessing VLBI data for all its members. However, its large flux limit has biased our knowledge for many years, providing little or no information on low power, high-frequency peaked objects, which may constitute the bulk of the population when the flux limit is lowered. In fact, other samples have been selected and new BL Lacs have been discovered. Most of these samples are based on the cross correlations of radio and X-ray surveys (e.g. REX, DXRBS), and they are expected to deliver significant results in the next years. However, there is an important issue involving the optical band as well, namely the identification and the study of the host galaxy of all these objects. Given the contamination from the non-thermal continuum and the considerable distance of the majority of objects, high angular resolution is vital to the study of the host galaxy. For this reason, we believe that the Hubble Space Telescope (HST) survey of BL Lacs has provided us with a richness of information that deserves to be fully exploited. In particular, the subset of low redshift ($z < 0.2$) objects constitutes an ideal sample to focus on. The sample is composed of 30 objects, originally selected with different methods and is largely dominated by weak HBL. Among other advantages, it is important to note that focusing on nearby objects allows us to study the weakest and least known objects as well as to achieve the best linear resolution.

Our first goal is to collect radio images for all the objects in the sample. We will use new observations as well as the literature, in order to have reliable information on the morphology and flux density distribution on a wide range of scales, from the parsec to the kiloparsec. In order to do this, we will take advantage of the best available radio interferometers and, in particular for the highest resolution study, of the *Very Long Baseline Interferometry* (VLBI) technique. Once we are provided with data of good quality for all the sources, we will be able to derive constraints on their intrinsic properties, such as the Lorentz factor and the unboosted radio power. This is of vital importance, as it will allow us to compare the properties of our sample to those of the 1 Jy sample and, above all, of a sample of FR Is of similar redshift. We will be able to establish what are the best candidates for the parent population, thus testing the assumptions of the unified model. Moreover, we want to search for systematic differences between Low- (LBL) and High- (HBL) frequency peaked BL Lacs, in order to solve the dichotomy that is still present within the class. We will look for different behaviour in the two classes (e.g. core dominance, jet bending) and discuss whether orientation effects alone are able to explain the observed differences or some intrinsic properties actually differ. This is needed to a better understanding of the blazar sequence, which relates the peak frequency to an inverse function of the total luminosity.

Furthermore, it will be important to investigate more deeply observational properties related to the black hole mass and to the accreting process. Extended radio power, jet helicity, sub-mas flux densities are a few of radio quantities that could be useful in this study. Optical Hubble Space Telescope data are also important to this goal and will be used. The comparison to new and literature broadband data may be used to explain an interesting puzzle: is it possible an unification of all the low power radio sources: FR Is, BL Lacs, LINERs, LLAGN, LPC? These objects probably share the same basic mechanism, accreting in a radiatively inefficient mode, and being dominated by non-thermal emission from the relativistic jet. There are in fact indications that the primary reason for the FR I/FR II dichotomy may lie in a different nature of their accretion disks, with a critical value of the accretion rate separating the two.

Chapter 1 summarizes the observational properties of the BL Lacs through the electromagnetic spectrum, and Chapter 2 reviews the main issues related to the unification of radio loud Active Galactic Nuclei. The sample of low redshift BL Lacs is presented and discussed in Chapters 3 to 5: Chapter 3 presents the selection and the literature, Chapt. 4 is devoted to the images on parsec and kiloparsec scale, and the results are discussed in Chapt. 5. The last two chapters are devoted to the detailed study of two interesting low power sources: the properties of the TeV BL Lac Markarian 501 are discussed in Chapt. 6, whilst in Chapt. 7 we study the Compact Symmetric Object 4C 31.04.

Unless otherwise stated, we assume $H_0 = 71\,\mathrm{km\,s^{-1}\,Mpc^{-1}}$ and $q_0 = 0.5$ throughout. Spectral indexes α are defined such that $S(\nu) \propto \nu^{-\alpha}$.

Chapter 1

The properties of BL Lac objects through the electromagnetic spectrum

It is customary to base the classification of a BL Lac object upon its "featureless" optical continuum; typically, any emission line in the optical spectrum needs to show equivalent width $W_\lambda < 5\text{Å}$. As a matter of fact, the choice of this threshold can sometimes be misleading, since it is completely arbitrary and does not correspond to any significant physical transition. Furthermore, there is a *plethora* of peculiar properties at other wavelengths that characterize equally well the class, and have indeed been used to identify and classify its members. We will therefore devote the next sections to a summary of the most relevant observational results about BL Lacs in the different wavebands of the electromagnetic spectrum.

1.1 Radio

Flux limited radio surveys, such as the 3C, the B2, and most importantly the 1 Jy, have given significant contribution in discovering BL Lac object candidates. As a matter of fact, radio properties alone can be sufficient to identify a blazar, as it has been done by Caccianiga & Marchã (2004). Typically, BL Lacs distinguish themselves from other bright radio sources by a number of observational properties: flat spectrum, large variability and polarization, compactness and dominance of a high brightness temperature core.

BL Lac radio spectra are characterized by spectral indices $\alpha \leq 0.5$. For this reason, BL Lacs are more abundant in high frequency surveys than in low frequency ones.

In the synchrotron theory, a flat spectrum can be obtained from the superposition of the convex spectra of single regions with different self-absorption frequencies. In turn, this corresponds to the superposition of regions of different angular size, all located in a similarly small volume (e.g. the base of a jet).

If this explanation holds, the source compactness and core dominance are a natural consequence and are easy to explain: when the overall spectrum is flat, the core has to be the main responsible of the total flux density, with negligible contribution from extended, non self-absorbed, steep spectrum lobes; hence, the compactness and core dominance. Giovannini et al. (2001) have studied the total and core emission for a sample of radio galaxies, finding a correlation between them. However, the two BL Lacs Mkn 421 and Mkn 501 lie significantly above the correlation, meaning that their cores are far more bright than what one would expect for a radio galaxy of similar total power. Similarly, values of the radio core dominance $R = \frac{L_{\rm core}}{L_{\rm ext}}$ are typically such that Log $R \geq 0$, including extreme values Log $R \geq 2$ (e.g. in the 1 Jy sample, Rector & Stocke, 2001).

Being responsible for most of the radio emission, the compact and self-absorbed core deserves the main attention. Very Long Baseline Interferometry (VLBI) allows observers to penetrate deep into this region. The average resolution of the VLBA at 5 GHz is 1.4 mas, equivalent to ~ 2.4 pc at a typical redshift of $z = 0.1$. Furthermore, given the flat spectrum of BL Lacs, it is not impossible to observe the best candidates also at 8.4, 15, and 22 GHz, reaching resolution of up to 0.3 mas. Development of mm-VLBI will allow in the near future to probe the very inner regions at $\lesssim 0.01$ pc, which correspond to ~ 100 Schwarzschild radii for a black hole of $10^9 M_\odot$.

VLBI images of BL Lacs reveal a compact, bright core. Typical flux densities are between a few and a few 100's mJy. Correspondingly, given the compactness on scales ≤ 1 mas, the *observed* brightness temperatures are close to the Inverse Compton limit ($T_B \sim 10^{12}$ K). Often, an one-sided jet emerges from the core. In the bulk of objects, the jet is very short (a few milliarcsecond) and is typically composed only of one single compact *blob*; in a few more favourable cases, it is possible to track the jet to larger distance and to study its "twisted" trajectory (e.g. in BL Lac itself, Stirling et al., 2003).

However, it is important to note that VLBI images are not available for all objects. Only the brightest members of the class have been studied in detail; thanks to VLBA and EVN observations (e.g. Cassaro et al., 2002, and references therein), there are VLBI images of good quality for all the members of the 1 Jy sample. A few more objects have been observed in separate projects (e.g. Kollgaard et al., 1996; Rector et al., 2003), and VLBI surveys are providing snapshot images for some more objects (Fey & Charlot, 2000; Shen et al., 1998; Kellermann et al., 1998). However, given the relatively large flux limit of such surveys (typically ~ 1 Jy), the short exposures, and modest coverage of the (u, v) plane, this is far from having provided the scientific community with a comprehensive view of the parsec scale properties of the BL Lac class.

Moreover, multi-epoch studies are available for an even smaller number of sources, often considering very few epochs, with large time gaps and a poor matching in frequency and (u, v) coverages (and hence in resolution). Furthermore, two of the few quite detailed studies have yielded contrasting results. Jorstad et al. (2001) have carried out an extensive analysis of EGRET-detected blazars, including 11 BL Lacs, concluding that superluminal motions are frequent in this class. On the contrary, systematic studies on a few TeV objects indicate that superluminal motions are not common in this sub-class (Tingay & Edwards, 2002; Piner & Edwards, 2004); the parsec scale jets of these sources present components moving at subluminal apparent speeds, often consistent with no motion at all (stationary components). It is not yet clear, and needs to be investigated, whether the discrepancy is due to the poor statistics or rather the two samples have for some reason different behaviour; in this case, the relation to the $\gamma-$ray properties needs also to be understood.

As for polarization, Very Long Baseline Polarimetry is in itself a difficult field; however, the high fraction of polarized flux in BL Lacs allows observers to study at least the brightest objects. Although results are not always easy to interpret, there seems to be a preference for transverse magnetic fields in the jets of BL Lacs (Gabuzda, Pushkarev, & Cawthorne, 2000). This can be explained in terms of a toroidal topology, as supported by Faraday rotation maps (Gabuzda & Murray, 2004). Significant core polarization ($2 - 6$ %) is also often present, either parallel or perpendicular to the direction of the jet, possibly brought about by beam confusion or by different optical depth for the two regions.

There is a couple of points that deserve to be highlighted at this point. First, most of the properties observed in the radio band can be naturally explained as signatures of synchrotron emission affected by relativistic beaming; in the following sections, we will show properties supporting such view also at other wavebands. Secondly, we note that bright radio surveys are biased in favour of Low frequency peaked BL Lacs (LBL)[1]; in fact, most LBL have been referred to as Radio selected BL Lacs (RBL) for long time. A better knowledge of the radio properties of less powerful, High energy peaked BL Lacs (HBL) is among the goals of the present thesis.

1.2 Optical

Historically, the optical band has been the principal dominion for the discovery of the class. The variability, star-like appearance, and featureless spectrum of one object (BL) in the constellation Lacerta have set the characteristic properties in defining the class. BL Lacs spectra are unusual also in that they present values of the Ca II break[2] smaller than low power radio galaxies and non active ellipticals. This break is a typical absorption feature due to stellar spectra, which causes the continuum to be strongly suppressed (about 50%) below 4000 Å. The absence of the break is explained by the presence of a non-thermal power law continuum, dominant over the spectrum of the host galaxy. Strong polarization is also typical of BL Lacs, and is ascribed to the same non-thermal continuum.

The featureless spectrum makes the redshift determination extremely difficult. Many objects still lack redshift information, even in well studied samples (e.g. 6/37 in the 1 Jy sample). Unfortunately, a missing redshift affects the determination of the absolute properties of the object and of its host. In particular, the host properties have been debated for many years, also because of the difficulty of disentangling the galaxy from the nuclear contribution.

The step forward in angular resolution produced by the *Hubble Space Telescope* (HST) has yielded a breakthrough in our knowledge on BL Lac host galaxies. Scarpa et al. (2000) have carried out a snapshot survey on 110 BL Lacs, with $z < 1.3$. Host galaxies have been detected in $\sim 2/3$ of the objects, up to $z = 0.664$; one- and two-dimensional analysis have been performed by Urry et al. (2000) and Falomo et al. (2000), respectively. The BL Lac host is typically a giant, luminous, elliptical galaxy:

[1]A working definition of the separation between LBLs and HBLs is based on the value of observed Log L_X/L_R, which is below or above -5.5, respectively. In Sect. 1.4, we analyse the two classes in better detail.

[2]This feature is defined as $C = (f_+ - f_-)/f_+$, where f_- and f_+ are the fluxes in the rest frame wavelength ranges $3750 - 3950$ Å and $4050 - 4250$ Å respectively.

exponential disk profiles are excluded in almost all objects and, even in questionable cases, never preferred; median absolute magnitude is $M_R = -23.7 \pm 0.6$; ellipticity is typically small, and disturbed morphologies unusual. This properties are very similar to those of FR I radio galaxies; furthermore, no difference between hosts of LBL and HBL has been found.

The possibility of separating the contribution of the non thermal continuum allows to investigate in BL Lacs host galaxies the well known relations that hold for other massive ellipticals. Also in this respect, the hosts of BL Lacs are indistinguishable from non active massive ellipticals. For example, the fundamental plane (a relation linking the average surface brightness, stellar velocity dispersion, and effective radius) is well verified (Falomo et al., 2003).

Therefore, the host galaxy properties can be used to estimate the mass of the central black hole. In fact, given the lack of broad lines in their spectra, the usual method of reverberation mapping of strong emission lines can not be applied to BL Lacs. Estimates for the mass of the central supermassive black hole are therefore derived by means of the relations between $M_{\rm BH}$ and (i) the bulge luminosity M_R (Magorrian et al., 1998; Kormendy & Gebhardt, 2001; McLure & Dunlop, 2002) or (ii) the central stellar velocity dispersion σ (Ferrarese & Merritt, 2000; Gebhardt et al., 2000).

Both the $M_{\rm BH} - M_R$ and $M_{\rm BH} - \sigma$ relation take advantage of the separation of the nuclear continuum from the host galaxy. The $M_{\rm BH} - \sigma$ has a smaller intrinsic scatter; however, estimates of the stellar velocity dispersion have been studied only for a few objects, and not always yielding consistent results (see Barth, Ho, & Sargent, 2003; Falomo, Kotilainen, & Treves, 2002; Falomo et al., 2003). On the other hand, the use of the fundamental plane to derive σ brings about an extra step, affected by its own scatter. For this reason, black hole mass are preferably estimated from the bulge luminosity. In any case, when a direct measurement of σ is available, Falomo et al. (2003) have shown that there is a good agreement between the two methods. Typical results for $M_{\rm BH}$ in BL Lacs are of order $10^8 M_\odot$.

As for the non-thermal continuum, the central compact component gives a significant contribution to the total luminosity. At larger z, the active core outshines the host galaxy. On the other hand, it has been possible for some near, powerful sources to discover optical jets; the sources are 0521−365, 3C 371, 2201+044 (Scarpa et al., 1999b, and references therein) and they all belong in the sample that we are going to study. Radio observations of comparable resolution have revealed that a remarkable correspondence holds between optical and radio features (e.g. knots), indicating that the emission mechanism is most likely the same in both wavebands. The radio optical spectral index is quite constant along the jet, with values of $\alpha_{\rm RO} \sim 0.7 - 0.8$. Therefore, the radio synchrotron emission seems to extend undisturbed to the optical. As a matter of fact, Chiaberge, Capetti, & Celotti (1999) have found a significant linear correlation between radio and optical compact cores in local FR I radio galaxies, and interpreted the linear slope of the correlation in terms of a common emission mechanism, synchrotron radiation indeed. It is plausible that the same correlation holds for BL Lacs and preliminary results seem to confirm it (Chiaberge et al., 2000). Taking advantage of our new high quality radio data, we will be able to further investigate this fundamental issue.

1.3 High energy

A significant number of BL Lacs have been discovered in X-ray surveys. For example, a complete sample of 42 objects has been extracted from the *Extended Medium Sensitivity Survey* (EMSS), performed by the Einstein satellite in the $0.3 - 3.5$ keV energy band (Stocke et al., 1991); a large number (62) of BL Lacs have been found also in Einstein's *Slew* survey (Perlman et al., 1996). Moreover, X-ray follow-up observations of radio selected BL Lacs have revealed high energy emission from all the objects considered. Interestingly, X-ray emission has been found for all BL Lacs selected in radio (without constraints on X-rays properties) and is therefore a characteristic property of the BL Lac class; similarly, radio emission, though occasionally extremely weak, is present in all objects selected at X-ray energy without using radio information. It is important to note, though, that there are some significant differences within the class, which distinguish quite neatly objects selected in radio and in X-rays.

This dichotomy, however, is probably due to selection effects and is not intrinsic to the class. BL Lacs of intermediate properties have been discovered and probably most of the apparent gap between the two extremes will be filled thanks to new observations. As a matter of fact, the cross correlation of radio and X-ray data is now frequently exploited to improve the efficiency in finding BL Lacs.

Padovani et al. (2004, 2001) report *BeppoSAX* observations in the broad energy range 0.1 - 10 keV for objects in the 1 Jy sample. Spectra are typically flat ($\alpha_X \sim 0.7$), with occasional steepening at lower energy. This is in agreement with soft X-ray spectra obtained by Urry et al. (1996) with the ROSAT Position Sensitive Proportional Counter (PSPC). The PSPC observations in the 0.1-2.0 keV energy band are well fitted by power laws with steep photon indices $1 < \Gamma < 3$. It must be noted, however, that the average properties are quite different in the two subclasses: typically, LBLs have X-ray spectra flatter than HBLs. Similar results stem from ASCA observations between 2 and 10 keV. Kubo et al. (1998) observed 18 blazars, finding softer spectra for HBLs ($\alpha \sim 1-2$) and intermediate values for LBLs. Finally, spectral lines blazars possess the hardest spectra ($\alpha \sim 0.6$).

This is interpreted as the superposition of an Inverse Compton component to the high energy end of the synchrotron emission. In LBLs, the synchrotron component is limited to energies below 2 keV, with the Compton component being dominant above it (hence the hard spectrum). Conversely, X-ray HBLs spectra are fully explained as the high energy tail of the synchrotron component, with the signature of Inverse Compton becoming relevant only at the very highest energy.

As a matter of fact, in a number of HBLs the high energy component is not detected even in the GeV dominion, and becomes relevant only at TeV energy. In the Third EGRET Catalog of High-Energy Gamma-Ray Sources (Hartman et al., 1999), LBLs outscored HBLs 14 to 2 above 100 MeV. However, the opening of a new window at Very High Energy (VHE) has yielded exciting results: Markarian 421 has been the first TeV detection (Punch et al., 1992), followed by Mkn 501 (Quinn et al., 1996), which was actually the first TeV source not previously detected by EGRET. In the following years (1995-2000), the Whipple telescope has observed 29 blazars at VHE, detecting three more sources: 1426+428 (Horan et al., 2002) 1959+650 (Holder et al., 2003), and 2344+514 (Catanese et al., 1998); for the other sources, it has been only possible to provide upper limits (Horan et al., 2004). Other observations (e.g. HEGRA, Crimea) confirmed these detections or even anticipated them, e.g. in the case of 1959+650 (Nishiyama et al., 2000). In total, considering also 2155−304 (Chadwick et al., 1999) and the unconfirmed detection of 3C66A and BL Lacertae itself, BL Lacs make up almost 50% of the sources reported to emit at TeV energy (8 out of 18 sources as of 2003, Horan & Weekes, 2003). Interestingly, they are all at $z < 0.2$ and, except for PKS 2155−304 and the unconfirmed 3C66A, they are part of the sample studied in this thesis.

The detection of $\gamma-$rays from BL Lacs has some important consequences. First, its very existence implies that the sources are transparent to it, with little absorption by the $\gamma - \gamma \longrightarrow e^+e^-$ process. Given the *observed* photon densities, this means that relativistic beaming occurs in the source (see Sect. 2.2). Secondly, although the number of photons collected in this band are small, their energy is so extreme that the total power output in this band becomes very large. During outbursts, it can even exceed the power emitted in the rest of the spectrum.

1.4 Broadband Spectral Energy Distribution and the blazar sequence

We have repeatedly mentioned HBLs and LBLs in the previous sections and we have shown some differences between this two subclasses. However, we have only given a working definition and we need to focus on this widely discussed issue. Originally, BL Lacs used to be divided into two categories, according to the waveband they were selected in. Radio selected BL Lacs (RBL) are more polarized, variable, and core dominated, whilst X-ray selected BL Lacs (XBL) display somehow less extreme properties; on the other hand, XBLs seem to evolve negatively, which is rather peculiar for an AGN class. Only the X-ray flux are comparable in the two subclasses.

The availability of large samples and of multi-wavelength data made clear that this dichotomy is purely a selection effect, and the division in RBL and XBL unphysical. A synchrotron spectrum can fit both classes, with a large scatter in peak frequency; when $\nu_{\rm peak}$ is in the IR/optical, α_{RX} is large, and the object is easy to find in radio surveys; conversely, when the spectrum peaks in the UV/X-ray, flatter α_{RX} are found, and the object is more likely discovered in X-rays. As a matter of fact, the ratio between radio and X-ray flux densities constrains the peak frequency and is a valuable tool for the classification. Typically, when Log $f_X/f_R \geq -5.5$, the object is an HBL, and vice versa, although some authors put the threshold at Log $f_X/f_R \geq -6$.

However, the availability of several large samples and broadband data have refined this situation. First, there is actually a continuity of objects, and the threshold between LBLs and HBLs is also rather arbitrary (Laurent-Muehleisen et al., 1999). Moreover, high energy satellites and ground based Cherenkov telescopes have

Table 1.1 Schematic summary of average properties of LBLs and HBLs

	LBL	HBL
Synchrotron component peak frequency	LOW (IR)	HIGH (X)
Inverse Compton component peak frequency	LOW (GeV)	HIGH (TeV)
Compton dominance (L_C/L_S)	HIGH ($>> 1$)	LOW ($\lesssim 1$)
Inverse Compton photons	external (EC)	self (SSC)
Total Luminosity	HIGH	LOW

provided data in X− and γ−rays. These data have greatly improved our knowledge of the spectral energy distribution, clearly showing the presence of a second, high energy component. The peak of this high energy component can also occur over a broad range of frequency. However, its behaviour is strictly related to the characteristic of the low energy part and it is most easily explained in terms of Inverse Compton scattering. The mean properties of the two subclasses are accordingly quite different over the whole electromagnetic spectrum (see Tab. 1.1).

In particular, LBLs possess: low peak frequency for both the synchrotron (in the IR/optical) and the Inverse Compton ($\sim$ GeV) component; large Compton dominance ($L_C/L_S >> 1$), which means that most of the total power is emitted in the Inverse Compton component; significant contribution from external photons (EC) to the seed population for the Inverse Compton. Conversely, in HBLs we have: high $\nu_{\rm peak}$ of the synchrotron and the Inverse Compton SED components (in the UV/X and TeV bands, respectively) and a smaller L_C/L_S ratio; typically, the Inverse Compton peak can be explained solely by Doppler-boosted synchrotron self-Compton (SSC) emission (Kubo et al., 1998).

Finally, Fossati et al. (1998) have shown that also the SED of BL Lacs (and emission line blazars) form a continuum, and that the peaks shift to higher frequency as the bolometric luminosity decreases. Donato et al. (2001) confirmed this trend considering more sources and hard X−ray data. Among possible explanations, Ghisellini et al. (1998) proposed that an increase in luminosity causes the emitting particle to suffer of more severe radiative losses; in turn, this explains the shift of the peaks to lower frequency.

There are however some problems with this scenario. Padovani et al. (2003) considered a large sample of ~ 500 blazars, following the discovery of a significant number of FSRQs with flat α_{RX} in a deep survey (the DXRBS, see Landt et al., 2001, and Sect. 3.2). Although Padovani et al. (2003) focus mainly on flat spectrum radio quasars, the result affects also BL Lacs. Among their claims, they found no evidence of anticorrelations between ν_{peak} and radio power (or other related quantities), as expected from the blazar sequence.

Finally, Caccianiga & Marchã (2004) present a few examples of low radio power BL Lacs with steep α_{RX}. Combining the results of the two works, it seems that there may exist sources with a peak at low frequency and steep α_{RX}, as well as objects peaking at high frequency but still displaying flat α_{RX}.

Chapter 2

The Unification of Active Galactic Nuclei

The term "active galactic nucleus" (AGN) is generally used to refer to extragalactic sources in which a large amount of energy is emitted within small scales and can not be ascribed to the thermal continuum of stars alone. There are several possible signatures of the nuclear activity, which have historically led to the classification of many types of AGN. In Chapter 1 we have described the broadband spectral properties of BL Lacertae objects; Seyfert galaxies, quasars, radio galaxies are a few of other AGNs, each displaying different properties. In this chapter, we describe the approach that several authors have proposed in order to interpret the different observed properties and to unify them in a unitary view. We will discuss some of the observational methods supporting this scheme, focusing on low power radio loud objects, and the way they can be used to infer the physical parameters of the sources.

2.1 The unified model for radio loud AGN

The typical amount of energy emitted by an AGN in the visible part of the spectrum ranges between $\sim 10^{11} L_\odot$ and $\sim 10^{13} L_\odot$. However, this is only a part of the total luminosity emitted by an AGN in all the electromagnetic spectrum. In particular, some AGN possess emission in the radio band that is 10 or more times stronger than in the optical. These objects are called radio loud, and they make up about 10% of the total number of AGN. The radio emission in these objects can present a wide range of properties: it can originate in compact regions of (sub-)galactic size or extend for hundreds of kiloparsec; the spectrum can be steep, flat, or even inverted.

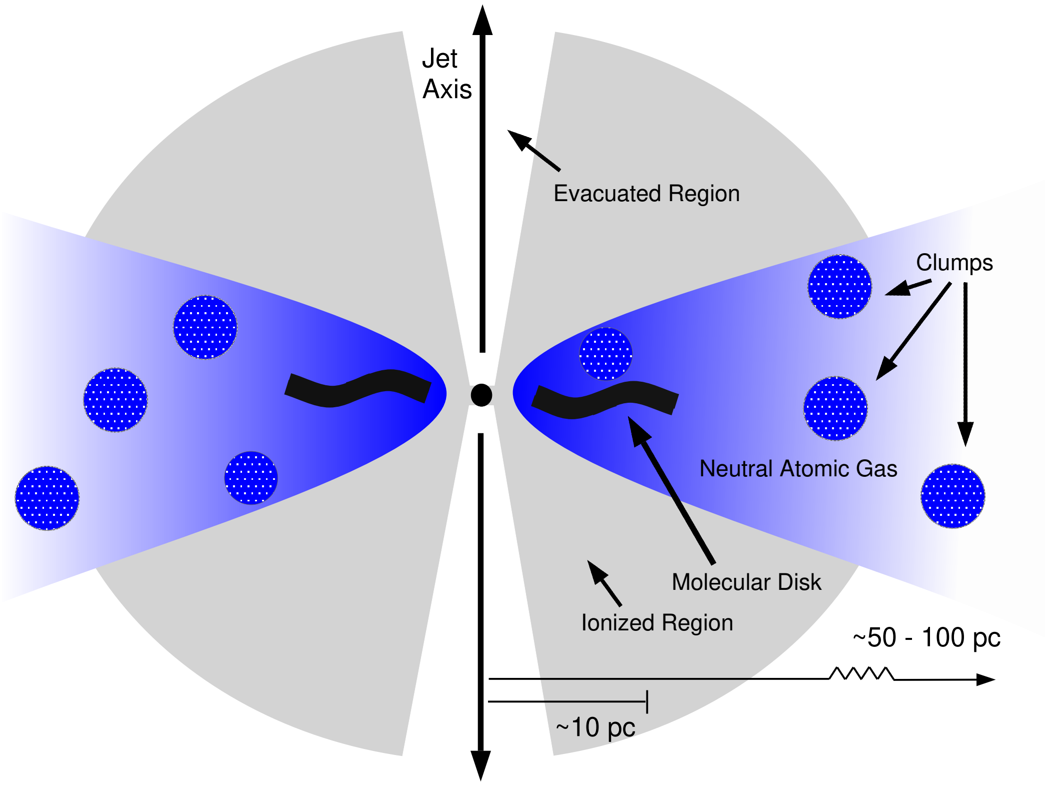

Figure 2.1 Cartoon reproducing the picture of a radio loud AGN (Taylor, 2000)

Furthermore, the optical object associated to the radio source can also belong to different categories: elliptical galaxies or quasi stellar objects; with broad, narrow, or even absent emission lines. When investigated on arcsecond or even milliarcsecond scales, more differences become apparent and call for explanations: objects can be symmetric with respect to a central core or develop only on one side of the host galaxy; the core itself can be the dominant component or barely detectable.

Some features common to different classes suggest that it may be possible to achieve a unitary view of these sources. Indeed, the possibility to unify the different types of objects has been explored since the early 80's (Orr & Browne, 1982); after many years of study, much evidence has been found in favour of a scheme in which orientation affects the *observed* properties of objects that are intrinsically similar, except for a possibly broad range of intrinsic power. Figure 2.1 illustrates a possible parsec scale model of the central region of an AGN. Basically, the ultimate responsible of the nuclear activity is thought to be a supermassive black hole (e.g. a black hole with mass $10^8 M_{\odot}$) accreting matter through a hot rotating disk.

The released gravitational energy is turned into thermal emission, mainly in the ultraviolet and soft X-ray. Clumps of atomic gas situated in the surrounding region are responsible for broad emission lines, while the narrow features in the spectra are probably originated in more external regions. Finally, a relativistic plasma is ejected along the main axis of the torus in two symmetrical collimated jets; radio emission is produced by electrons in the jets via the synchrotron mechanism. Although this is a rather simplistic view and sophisticated models have been developed for its details, it has been successful in explaining observational properties of most of the radio loud AGN (see e.g. Urry & Padovani, 1995, for a famous comprehensive review).
This anisotropic structure turns into the observed variety of objects mainly thanks to two key elements:

- **obscuration** from a thick region (possibly a torus) external to the accretion disk and the broad line clouds, which absorbs the radiation coming from the inner region;
- **beaming effects** brought about by the relativistic motion of the plasma in the jets.

Basically, obscuration can explain some properties of the cores: when they are observed from large viewing angles, broad line clouds are not accessible and can be observed only in polarized light (thanks to scattering); observed X-ray luminosity is also consistent with absorption from a circumnuclear structure. As for beaming, we present in the next section some effects that stem from the laws of special relativity and that successfully account for observed properties of radio loud AGN.

2.2 Relativistic effects in Astrophysics

When the measuring process can not be directly operated on the targets of the experiment, as is clearly the case in astrophysics, it is necessary to consider information carried by photons; when the source of the photon is moving relativistically, the well known Lorentz transformations must be somehow reconsidered. In particular, we want to show two simple results in which the main parameter is the *Doppler factor* δ, a function of *both velocity and viewing angle*. We will then show how these effects can be exploited to account for several observed properties of radio loud AGN.

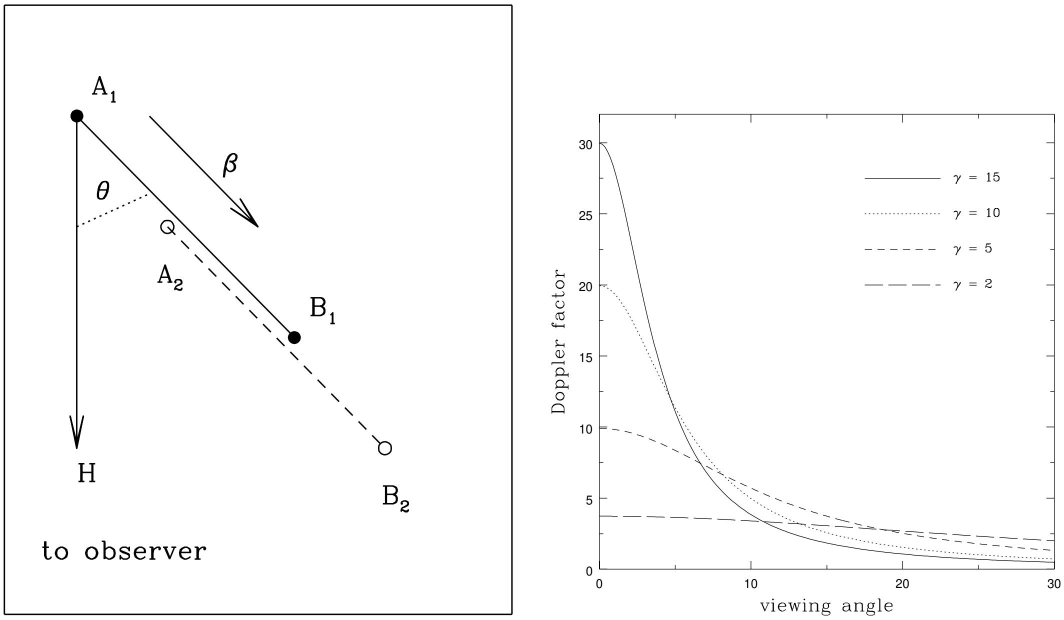

Figure 2.2 Left: bar moving at relativistic speed in a transverse direction; the observer receives simultaneously photons emitted at different times. Right: Doppler factor as a function of viewing angle, for different Lorentz factors.

2.2.1 Lengths and flux densities

Length of a moving bar

Let us consider a bar A_1B_1, with length ℓ' in the co-moving frame, in motion along its direction with velocity v ($\beta = v/c$); let θ be the angle between this direction and the line of sight (Fig. 2.2, left). Consider a photon emitted in A_1 at time $t = 0$; after an interval Δt it is at the same distance from the observer as B_2. A photon emitted at this time in B_2 will reach the observer simultaneously to the one coming from A_1. Δt can be calculated by substituting in $A_1H = A_1B_2 \cos\theta$ the following relations:

$$A_1H = c\Delta t \qquad B_1B_2 = v\Delta t = c\beta\Delta t \qquad A_1B_2 = \ell + c\beta\Delta t = \frac{\ell'}{\Gamma} + c\beta\Delta t \tag{2.1}$$

This yields

$$c\Delta t = (\frac{\ell'}{\Gamma} + c\beta\Delta t)\cos\theta \tag{2.2}$$

i.e.

$$\Delta t = \frac{1}{c}\frac{\ell'\cos\theta}{\Gamma(1-\beta\cos\theta)} \tag{2.3}$$

Finally, we have

$$A_1H = c\Delta t = \frac{\ell' \cos\theta}{\Gamma(1-\beta\cos\theta)} \tag{2.4}$$

which yields an *observed* length

$$A_1B_2 = \frac{A_1H}{\cos\theta} = \frac{\ell'}{\Gamma(1-\beta\cos\theta)} \equiv \delta\ell' \tag{2.5}$$

We have introduced the *Doppler factor* $\delta = \dfrac{1}{\Gamma(1-\beta\cos\theta)}$. Some particular values are noteworthy: if the motion of the bar is perpendicular to the line of sight, then $1-\beta\cos\theta = 1$ and we find $\ell = \ell'/\Gamma$, as in the ordinary Lorentz case. As a matter of fact, this case is equivalent to measure the bar directly, since the photons track equal paths. In the case that viewing angle and velocity are related by $\cos\theta = \beta$, the denominator in 2.5 is unitary, and the observed bar lengths is ℓ', i.e. the same as the rest frame one.

Flux densities

Let us consider a source moving at $\beta = v/c$, along a direction that forms an angle θ to the observer's line of sight; let $\nu_{\rm em}$ be the frequency of the signal emitted by the source.

Pure relativistic time dilation effects will redshift the frequency by a factor $1/\Gamma$, while the Doppler effect will cause the frequency to be rescaled by $(1-\beta\cos\theta)^{-1}$, i.e. red- or blue-shifted according to the direction of the motion (i.e. the sign of $\cos\theta$). The combination of the two effects corresponds to rescaling the rest frame frequency by a factor δ:

$$\nu_{\rm obs} = \nu_{\rm em} \times \frac{1}{\gamma} \times \frac{1}{1-\beta\cos\theta} = \delta\nu_{\rm em} \tag{2.6}$$

The flux density observed at frequency $\nu_{\rm obs}$ is given by the number of photons received and h times the observed frequency (where h is the Planck's constant). From the above relation and the fact that the number of photons is conserved, we get:

$$S(\nu_{\rm obs}) = n(\nu_{\rm obs}) \times h\,\nu_{\rm obs} = n'(\nu_{\rm em}) \times h\,\delta\nu_{\rm em} = \delta\, S'(\nu_{\rm em}) \tag{2.7}$$

By integrating on the whole spectrum, we obtain:

$$
\begin{aligned}
S_{\mathrm{tot}} &= \int S(\nu_{\mathrm{obs}})\, d\nu_{\mathrm{obs}} = \int S'(\nu_{\mathrm{em}})\, \delta\, d\nu_{\mathrm{obs}} = \int S'(\nu_{\mathrm{em}})\, \delta^2\, d\nu_{\mathrm{em}} = \\
&= \int \frac{L(\nu_{\mathrm{em}})}{4\pi d'^2}\, \delta^2\, d\nu_{\mathrm{em}} = \int \frac{L(\nu_{\mathrm{em}})}{4\pi d^2}\, \delta^4\, d\nu_{\mathrm{em}} \qquad (2.8)
\end{aligned}
$$

i.e.

$$
S_{\mathrm{obs}} = \frac{L_{\mathrm{em}}}{4\pi d^2}\, \delta^4 = S_{\mathrm{em}}\, \delta^4 \qquad (2.9)
$$

The factor δ^4 can amplify the total flux by extremely large values, for particular values of Γ and θ (see 2.2, right panel), favouring the observation of faint sources, when their jet points toward the observer (*Doppler favoritism*).

2.2.2 Estimating the Doppler factor

The unified scheme relies heavily on the existence of relativistic plasma flowing through channels from the innermost region to the outer lobes. As a matter of fact, relativistic beaming is needed to account for a number of observational properties, among which:

- jet sidedness and bending: by moving in opposite directions with respect to the observer, the two intrinsically identical jet and counterjet of a relativistic source possess opposite velocity ($+v$ and $-v$), resulting in different Doppler factors: the ratio of their observed brightness can therefore largely deviate from unity; similarly, a bent jet changes angles and therefore Doppler factor, with projection contributing to amplify the intrinsic bending further.

- the scatter in the relation between total and core radio luminosity: although the detailed velocity structure of jets is still poorly understood, we know that the plasma flows relativistically in the inner part of the jet and is slowed down to non relativistic speed in the large scale lobes; similar extended powers can therefore be associated to a large range of nuclear observed power, depending on the viewing angle of the inner, relativistic part of the jet.

- high brightness temperature of radio cores, e.g. with respect to observed X-ray luminosity: the synchrotron emission from the jets inevitably produces X-rays via Inverse Compton scattering; since VLBI observations show that the emitting region are compact on very small scales, the observed X-ray fluxes can be reproduced by SSC models only if the radio emission is subject to boosting.

- rapid variability at all wavelengths, including γ-ray emission: the $\gamma - \gamma \longrightarrow e^+e^-$ process is the main responsible for the decay of $\gamma-$rays and, given the observed luminosity of AGN, it should prevent us from observing high energy emission. EGRET detection of $\gamma-$rays, in particular for blazars, can be explained only if the observed photon density is enhanced by beaming. Variability observed on short timescales is also calling for relativistic beaming to be explained.

- superluminal motion of jet components: components in relativistic motion toward the observer run after their own emitted photons, so that the observed time lag is smaller and the apparent velocity can be larger than c: $\beta_{\rm app} = \dfrac{\beta \sin\theta}{1-\beta\cos\theta}$; note however that in this case we are not dealing with the jet *bulk* velocity but only with a *pattern* velocity, possibly related to shocks or blobs moving in the jet with a different speed.

Of course, the exact amount of beaming needed to account for each of the previous effects is not easy to constrain. Furthermore, changes in orientation or Lorentz factor may take place in different parts of the jet, resulting in different requirements for the Doppler factor. Radio data can be used to constrain δ on a broad range of scales, from the parsec to the kiloparsec. In particular, we will make use in the rest of this thesis of three main indicators: jet/counterjet ratio, core dominance, and SSC model. Proper motion will also be considered in the multi epoch study of Markarian 501 (Chapter 6).

Jet/counter-jet ratio

Let us consider two identical jets originating from the core in opposite directions; let $+v$ e $-v$ be their velocity with respect to the observer for the approaching and receding jet, respectively. The relative Doppler factors are then $\delta = \dfrac{1}{\gamma(1-\beta\cos\theta)}$ and $\delta = \dfrac{1}{\gamma(1+\beta\cos\theta)}$. For a synchrotron jet, the spectrum is described by a power law $S(\nu) \propto \nu^{-\alpha}$ and the observed brightness is δ^p times the rest frame one. $p = 2+\alpha$ is preferred for a continuous jet, while $p = 3+\alpha$ is more appropriated in the case of a moving sphere (e.g. a *blob*). The brightness ratio between jet and counterjet is then

$$R = \left(\frac{1+\beta\cos\theta}{1-\beta\cos\theta}\right)^p \tag{2.10}$$

In presence of relativistic jets, a small values of θ can make this ratio rather large. It is then possible that the counter-jet is deboosted below the sensitivity of the observation, and we observe one-sided sources.

Core dominance

The core dominance is a typical estimator of beaming (Ghisellini et al., 1993; Morganti et al., 1995; Rector et al., 2000). As we noted, the base of the jet is more affected by relativistic beaming than the extended lobe emission. We can apply to the core luminosity an approach similar to the jet/counterjet argument. In this case, the comparison is between the observed value and an average "expected" core power. This value can be derived from the total low frequency luminosity via the best-fit relation studied by Giovannini et al. (1988, 2001). In a statistical sense, this is the value expected for a source oriented at 60°, which is the most likely case. The correlation has the form:

$$\mathrm{Log}\ P_c = (0.62 \pm 0.04)\mathrm{Log}\ P_t + (7.32 \pm 1.09) \tag{2.11}$$

Let P_i be the *intrinsic* radio power of the core and θ the angle formed by the jet and the line of sight. Then

$$P_c(\theta) = P_i\,\delta^{2+\alpha} = \frac{P_i}{\Gamma^{2+\alpha}(1-\beta\cos\theta)^{2+\alpha}} \tag{2.12}$$

and the best-fit value is related to the intrinsic one by

$$P_c(60°) = \frac{P_i}{\Gamma^{2+\alpha}(1-\beta/2)^{2+\alpha}} \tag{2.13}$$

Solving for P_i, we obtain:

$$P_c(\theta) = P_c(60°)\left(\frac{1-\beta/2}{1-\beta\cos\theta}\right)^{2+\alpha} \tag{2.14}$$

Let $\alpha = 0$ (which is typical for radio cores), and $K = \left(\frac{P_c(\theta)}{P_c(60°)}\right)^{0.5}$; the observed values can then be used to put a constraint on β and θ, which must satisfy:

$$\beta = \frac{K-1}{K\cos\theta - 0.5} \tag{2.15}$$

SSC model

The observed radio flux can be used to estimate how much X-rays should be produced via the Synchrotron Self-Compton process (SSC). If we measure a different X-ray flux, we can constrain the amount of beaming required to reproduce a radio flux consistent with the X-ray data.
From Marscher (1987), the Doppler factor is:

$$\delta = f(\alpha)F_m \left[\frac{\ln(\nu_b/\nu_m)}{F_X\,\theta^{6+4\alpha}\,\nu_X^{\alpha}\,\nu_m^{5+3\alpha}}\right]^{1/(4+2\alpha)} (1+z) \tag{2.16}$$

where: $f(\alpha) = 0.08\alpha + 0.14$; F_m and F_X are the radio and X-ray flux densities (in Jy) at the frequency ν_m and ν_X (in GHz and keV, respectively); θ_d is the VLBI angular size of the core (in mas); ν_b the synchrotron high frequency cutoff (in GHz).

2.3 Unification in the low power regime

Among the many types of Active Galactic Nuclei, properties such as flat spectrum, large variability, and high polarization identify the group of compact radio loud sources collectively named blazars; this group includes the BL Lacs, which have the additional property of lacking optical emission lines. The above mentioned relativistic effects account for their observational properties, and suggest that these objects are oriented at small angles to the line of sight. By contrast, radio galaxies are extended, two sided objects, with little flux variability, and possess therefore the characteristics of objects lying in the plane of the sky. Radio galaxies are divided into two groups, according to their total radio power: sources with low frequency radio power $P_{178\mathrm{MHz}}$ below or above $10^{25}\,\mathrm{W\,Hz^{-1}}$ belong to Fanaroff-Riley class I (FR I) or II (FR II), respectively (Fanaroff & Riley, 1974). Although the separation in total luminosity is actually not so sharp, the two class undoubtedly possess quite different average properties. One of these properties, which was actually at the base of the original separation, is the different spatial distribution of the flux density. In

FR I, the core and the inner jets are more luminous than the lobes (edge dimmed sources); in FR II, the inner jets are barely visible and the well confined lobes host compact, bright hot-spots (edge brightened sources). The host galaxy properties are also different: although both types are hosted in large elliptical galaxies, FR I hosts are typically brighter; Ledlow & Owen (1996) proposed that the dividing radio luminosity increases with the host magnitude. Finally, FR I radio galaxies possess emission lines that are underluminous with respect to FR II (Zirbel & Baum, 1995). If BL Lacs are aligned objects, and radio galaxies are not, it is natural to try and associate aligned and misaligned populations. For all the mentioned properties, Fanaroff-Riley I radio galaxies are the most likely candidates as BL Lacs *parent population* (Urry & Padovani, 1995). However, this picture is somehow uncomplete. Rector & Stocke (2001) have shown that some BL Lacs in the 1 Jy sample have extended radio powers more similar to FR II, and broad emission lines have occasionally been observed in the spectra of some BL Lacs. Furthermore, the Lorentz factors required for this unification span a large range, and it would be important to constrain it better. Chapter 5 is devoted to discuss the Lorentz factor and the parent population of our low-redshift sample of BL Lacs.

Finally, projection is not the only responsible for the observed compactness of a radio source. Compact Steep Spectrum (CSS) sources make up a significant fraction of bright radio surveys ($\sim 10\%$) and their small angular size is intrinsic, rather than due to projection (Fanti et al., 1995). When observed with VLBI, these sources display all the features of an extended radio galaxy rescaled by a factor $10^{-2} - 10^{-3}$; hence, they are frequently referred to as Compact Symmetric Objects (CSO). The size of these objects is sub-galactic, and anticorrelates with the peak of the convex spectrum. Gigahertz Peaked Spectrum sources (GPS) are therefore less extended than CSS, and High Frequency Peakers (GPS, peaking at $\gtrsim 10$ GHz) are even smaller. Owsianik & Conway (1998) have revealed advance of the hot-spots in 0710+439, consistent with an age $\lesssim 10^4$ yrs, suggesting that this is actually en evolutionary sequence, and that age is a key parameter that needs to be considered for a unitary view of radio loud AGN. While all CSO studied so far are expected to evolve into FR II (Conway, 2002), we will present in Chapter 7 an analysis of 4C 31.04, whose radio power is among the weakest in these sources ($P_{5\mathrm{GHz}} \sim 10^{25}\ \mathrm{W\ Hz^{-1}}$).

Chapter 3

Low redshift BL Lacs: sample selection

In this chapter we discuss the need for new, better observations of a sample of low redshift BL Lacs; we consider different catalogues of objects and present the most suitable choice and its selection process; finally, we summarize some results from the literature. In the following chapters, we will describe our new observations (Chapter 4) and discuss the results (Chapt. 5).

3.1 Introduction

In Chapter 2 we have shown how the viability for a comprehensive view of Active Galactic Nuclei (AGN) has been actively debated, ever since the first suggestions of a possible unification of radio sources (e.g. Orr & Browne, 1982). A major achievement is the formulation of the scheme in which BL Lac objects and quasars are the aligned counterparts of edge darkened (FR I) and edge brightened (FR II) radio galaxies, respectively (see e.g. Urry & Padovani, 1995). However, many important issues still need to be worked out, in particular within the class of BL Lac objects.
For example, we are still trying to solve the apparent dichotomy present within the BL Lac population. It is clear that the distinction based on the selection criterion (RBL vs. XBL) is unphysical and out of date, and multi-wavelength studies on large samples seem to have solved also the discontinuity based on the position of the low energy peak in the spectral energy distribution (SED). This framework had BL Lacs classified as either low (LBL) or high (HBL) frequency peaked objects: LBL have the peaks of emitted energy (νF_ν) in the infrared/optical and MeV/GeV bands while HBL peak at higher frequencies, namely UV/X-ray and GeV/TeV. Fossati et al.

(1998) discovered that the position of the peaks are related to an inverse function of the total luminosity and several works afterward have tried to explain this sequence.

In spite of our advances in understanding, the jet physics and main properties are still matter of debate. On one hand, we have constraints from the detection of highly energetic (TeV) photons, which requires Doppler factor values $\delta > 10$ (Tavecchio et al., 1998); on the other, lower values are preferred from radio observations and from the lack of measured superluminal motions (Piner et al., 1999; Tingay & Edwards, 2002; Piner & Edwards, 2004). This discrepancy suggests that the γ-rays and the radio photons may be produced in different regions of the jet, moving at different bulk velocities or differently oriented with respect to the line of sight. Furthermore, it is also possible that the jet has a dual *transverse* velocity structure; this may be needed to explain the different behaviour of optical cores in BL Lacs with respect to FR I radio galaxies (Chiaberge et al., 2000). In particular, the optical radiation would come from a faster spine, whilst the radio emission would originate in a slower, external layer of the jet.

As a matter of fact, radio interferometry technique is an unique tool to determine the parameters of the jet in the region from a few parsec out to the kpc scale structure. In Sect. 2.2, we have reviewed some means to infer the beaming factor, such as jet sidedness, core dominance, SSC models, proper motion of knots (see also Giovannini, 2003). However, systematic and detailed VLBI studies on sizable samples of BL Lacs are mostly based on bright, flux limited catalogues, such as the 1 Jy sample (Stickel et al., 1991). By its very own definition, this sample consists mostly of powerful and distant objects. Furthermore, the selection is only in one waveband and, therefore, it can not include objects with high $\nu_{\rm peak}$, which is a severe limit in a comprehensive study of the BL Lac class. On the other hand, detailed studies focused on weaker objects are still missing or based on small numbers of objects (Rector et al., 2003).

The need for a sample of low-z objects is therefore clear. Low-z objects are preferentially weak in the radio, typically peaking at high $\nu_{\rm peak}$. They are then mostly HBL, and some of them are TeV emitters in their high energy spectral component. By contrast, their radio power is extremely low, which would make them comparable to radio quiet objects, when de-beaming were taken into account.

In order to investigate the above issues and to extend the current view to the low-

z objects, we want to consider a sample without any significant selection bias. We carried out new radio observations of this sample, to look for differences in morphology with more powerful objects and to derive parameters for jet physics. In this chapter, we review some samples discussed in the literature and focus on the selection of our sample, summarizing data from the literature.

3.2 BL Lac samples and biases

Historically, BL Lac samples have been selected in one band only, leading to the dichotomy between Radio and X-ray selected BL Lacs. In particular, there are two major samples that have driven our early knowledge. They are:

- **1 Jy** The first sizable, homogeneous sample of radio bright BL Lacs was selected by Stickel et al. (1991) out of the 1 Jy survey at 5 GHz (Kuehr et al., 1981). The relatively high frequency of the survey favours the presence of BL Lacs, since flat/inverted radio spectrum is one of the selecting criteria; bright optical counterparts (< 20 mag) and weak emission lines (rest frame EW ≤ 5 Å) are the other requirements. Rector & Stocke (2001) present final spectroscopy and VLA radio images for the sample. The properties of the objects are quite peculiar: moderately luminous emission lines are present and extended radio powers are frequently larger than in FR Is; these properties make objects in the 1 Jy sample more similar to FSRQ than to X-ray selected BL Lacs (see the EMSS sample below). VLBI studies have been carried out for all the objects in the sample (Cassaro et al., 2002, and references therein), revealing bright cores and one-sided jets. A high occurrence of large bending between pc and kiloparsec scale structure has also been noted (Cassaro et al., 2002; Appl et al., 1996); thanks to the availability of pc scale images, the 1 Jy sample is an ideal target to compare our sample with.

- **EMSS** The *Einstein* Medium Sensitivity Survey has produced a relatively deep ($f_X > 7\times10^{-14}\,\mathrm{erg\,cm^{-2}\,s^{-1}}$) catalogue of sources emitting in the soft (0.3 - 3.5 keV) X-ray band. Morris et al. (1991) have extracted a sample of 22 objects, complete at $f_X > 5 \times 10^{-13}\,\mathrm{erg\,cm^{-2}\,s^{-1}}$. The selection criteria are basically only on the optical spectrum: equivalent width of emission lines ≤ 5 Å and Ca II break contrast $\leq 25\%$ (Stocke et al., 1991). Rector et al. (2000) completed optical and VLA radio observations for this sample, and extended it to a total of 44 objects ($f_X > 2 \times 10^{-13}\,\mathrm{erg\,cm^{-2}\,s^{-1}}$). Spectral, radio, and evolutionary properties of this sample are in agreement with the unification of BL Lacs and FR I radio galaxies. However, an important result coming out from this work is the relatively high average core-to-extended flux ratio $\langle f \rangle \geq 4.2$, which posed some problems with an unification based solely on orientation effects. On the other hand, the comparison between the properties in the shallow and deeper sample does not support the existence of a blazar sequence. The EMSS sample is therefore important as it shows the need to focus on weak objects.

As we mentioned, these samples have selection criteria that are typically limited to one single waveband, with the only additional requirement of a strong non thermal optical continuum (weak or absent emission lines and/or calcium break). This selection process is quite inefficient and has two consequences that somehow bias the results. First, this method samples only a part of the SED and therefore favours the selection of extreme objects; secondly, flux limited samples are subject to a well known bias which affects the average properties of the sample: at high distances, these samples include only exceedingly bright objects.

However, it is interesting to note that follow up observations have revealed that all objects emit both in radio and X-rays, regardless of the selection criteria. As a consequence of this interesting result, the combination of information in the two wavebands has been largely exploited afterward, also favoured by the availability and development of on-line services. By cross-correlating radio and X-ray catalogues, many projects have been undertaken to select large BL Lac samples:

- **Einstein Slew survey** Elvis et al. (1992) have catalogued 819 sources (including 313 new detections) obtained from slew observations with the *Einstein* satellite. Schachter et al. (1993) identified ten new BL Lacs from this survey, exploiting broadband properties, i.e. requiring $0.3 \leq \alpha_{\mathrm{RO}} \leq 0.6$ and $0.55 \leq \alpha_{\mathrm{OX}} \leq 1.2$. Finally, Perlman et al. (1996) used the same criterion to extend the sample to 62 objects. Note that the Slew data are somehow shallower than the EMSS, having a typical flux limit of a few $10^{-12}\,\mathrm{erg\,cm^{-2}\,s^{-1}}$.

- **the Sedentary Survey** Carried out by Giommi, Menna, & Padovani (1999), it is a rather large catalogue of X-ray selected BL Lacs candidates. It is based on the cross correlation of the *ROSAT* Bright Source Catalog (RASS-BSC, Voges et al., 1999) in the 0.5 – 2.0 keV band and of the NRAO VLA Sky Survey (NVSS, Condon et al., 1998) at 1.4 GHz. As other X-ray all-sky surveys, the RASS is not very deep (count limit of 0.05 count s^{-1}), whilst the NVSS goes down to low radio flux density. This yields a total of 218 extreme HBL candidates, including a complete sample of 155 objects with flux limit in radio $f_r > 3.5$ mJy. Similar selection criteria have been adopted for the **HRX** BL Lacs sample (Beckmann et al., 2003), which is composed of 109 objects. These samples are important because they contain large numbers of extreme HBLs, which seem to display an unexpected negative evolutionary behaviour. Unfortunately, they both are biased toward HBL (the limiting flux is $f_X \geq 1.05 \times 10^{-12}\,\mathrm{erg\,cm^{-2}\,s^{-1}}$ in the Sedentary Survey) and lack optical high quality information.

- **RASS Green Bank (RGB)** This catalogue is based on the correlation of the ROSAT All-Sky Survey with a 5 GHz survey obtained with the Green Bank telescope; the radio catalogue has a flux limit of $\sim$ 25 mJy, i.e. it is much shallower than the NVSS. Extreme HBLs are therefore not as dominant in the RGB sample as they are in the Sedentary Survey. As a result, the 127 BL Lacs presented by Laurent-Muehleisen et al. (1999) display properties intermediate between LBL and HBL. In particular, the distribution of Log f_X/f_R peaks at $\sim$ 5.5, which is usually suggested as the the threshold separating the two subclasses. Raising the limits in radio or in X-ray selection of the RGB, the distribution would be consistent with that of the 1 Jy or of the Slew, respectively. This of course points to explain the bimodality as a result of solely selection effects. The RGB sample has however the limit of being selected from a single dish radio catalogue, and therefore completely lacks information on the nuclear properties.

- **REX Survey** The previous samples are affected by the large flux limit of the RASS. Caccianiga et al. (1999) try to improve the state of the art by cross correlating the NVSS to an X-ray catalogue derived from pointed ROSAT PSPC images; the flux limit at 0.5 – 2.0 keV is $\sim 5 \times 10^{-14}\,\mathrm{erg\,cm^{-2}\,s^{-1}}$.

In this way, they select a complete sample of Radio-Emitting X-ray sources (hence the name REX), containing about 1600 objects. The optical follow-up and classification is underway and is expected to deliver a sample of ~ 200 BL Lacs with intriguing properties; for example, a handful of newly discovered BL Lacs (or candidate) display hybrid optical spectra, with only weak optical non thermal continuum.

- **Deep X-ray Radio Blazar Survey (DXRBS)** Similarly to the REX survey, also the DXRBS (Perlman et al., 1998; Landt et al., 2001) considers deep X-ray observations from the ROSAT PSPC; however, in order to favour the selection of blazars, it also puts a constraint on the radio spectra, which has to be flat ($\alpha_R \leq 0.7$). This requires to consider more radio catalogues and has the effect of raising the radio flux limit to ~ 50 mJy at 5 GHz; in turns, this greatly enhance the efficiency in discovering faint blazars.

- **CLASS blazar survey** Based on the Cosmic Lens All Sky Survey (CLASS, Myers et al., 2003), Marchã et al. (2001) have selected ~ 300 sources down to $S_5 \geq 30$ mJy, with flat radio spectrum ($\alpha_{1.4}^{4.8} \leq 0.5$) and red magnitude $R \leq 17.5$. This sample does not pose any requirement on the X-rays properties; however, since it contains a large number of BL Lacs, it is included in the present list for completeness. As a matter of fact, it has been selected in order to study objects with steep α_{RX} among faint radio sources.

All these samples are contributing significant advance in the BL Lac field; some of them are also exploited to investigate the cosmological evolution and to test the blazar sequence. However, the optical information is rather poor: spectroscopy has not always been completed and information on host galaxies is available for a few objects at most. On the other hand, there is a large number of snapshot observations of BL Lacs performed with the Hubble Space Telescope (Scarpa et al., 2000). This has provided high resolution images that represent a wealth of information deserving to be carefully considered.

3.3 The HST snapshot survey of BL Lacs and the low redshift sample

Scarpa et al. (2000) have undertaken a large project to investigate the host galaxies of BL Lacs. The study of the host galaxy is a crucial test bed for unified schemes. Orientation is irrelevant to the host properties; their investigation provides therefore an useful check for the comparison of a population with its possible misaligned counterparts. The investigation of AGN hosts can also shed light on the possible triggers of the nuclear activity; merging events are among suspects and the presence of any unusual feature (e.g. disturbed morphology) could confirm it. Last but not least, several years of ground based observations did not help in solving the question whether BL Lacs could be hosted in disks.

By merging 7 flux limited samples, Scarpa et al. (2000) have collected a total of 132 BL Lac objects to study with the HST. The 7 samples are: 1 Jy (Stickel et al., 1991); S4 (Stickel & Kuehr, 1994); PG (Green et al., 1986); HEAO-A2 (Piccinotti et al., 1982); HEAO-A3 (Remillard et al., 1999); EMSS (Morris et al., 1991); Slew (Schachter et al., 1993; Perlman et al., 1996)

Starting from the 132 objects list, HST snapshot observations have been obtained for 110 objects. The selection of the observed targets from the original list is based only on the suitability to the HST schedule, so this does not introduce any bias. The observations have been done with the Wide Field and Planetary Camera 2 (WFPC2) through the F702W filter (occasionally in the F606W or F555W filter), providing a homogeneous set of short-exposure, high-resolution images. Main results have been published in Urry et al. (2000); we summarize them in section 3.4.

From this large dataset, Falomo et al. (2000) extracted a sub-sample of 30 low redshift ($z < 0.2$) objects for which it was possible to perform a detailed study of the properties of the host galaxy. We concentrated our attention on this work, since the redshift limit presents all the characteristics that suit our goals:

- it effectively reduces the bias toward brightest, unrepresentative objects
- conversely, it includes the weakest, least studied objects
- all the objects detected at TeV energy so far are at $z < 0.2$ and 5 of them belong to this sample

- all host galaxies have been resolved, separating the contribution of the host and of the non thermal continuum
- in this redshift range, the high angular resolution of VLBI techniques allows observers to investigate the very innermost regions (1 mas $\sim$ 1.7 pc at $z = 0.1$)

Thus, we undertook the project of obtaining parsec and kpc scale radio images for all the objects in this sample, either from the literature or from new radio observations. However, we first discarded three objects from the sample of Falomo et al.: 1853+671 and 2326+174, which have a redshift slightly larger than 0.2 ($z = 0.212$ and 0.213, respectively), and 2005−489, which is too south to be observed with comparable quality high resolution imaging. Conversely, we add three more objects, which also have $z < 0.2$ and high quality HST observations available. The objects are 1215+303 ($z = 0.130$, Perlman et al. private communication), 2254+074 ($z = 0.190$), and 1652+398 (Mkn 501, $z = 0.034$). In total we have 30 objects. Although the sample cannot be considered complete, the selection process appears free from significant biases with respect to source orientation and jet velocity.
Table 3.1 presents the full list of objects in the sample. HBLs are clearly dominant, and most objects have been originally selected at X-ray energies. This selection is significantly different from most previous studies at radio frequencies. We note that HBLs have lower total luminosities and are particularly weak in the radio. Figure 3.1 plots, as histograms, the distributions of total power at 1.4 GHz for objects in the present sample compared to the 1 Jy sample. The two distributions are significantly different, being that $\langle \mathrm{Log}P_{1.4\mathrm{GHz}} \rangle = 24.7 \pm 0.6\,\mathrm{W\,Hz^{-1}}$ and $26.7 \pm 0.9\,\mathrm{W\,Hz^{-1}}$, respectively (some objects in the 1 Jy sample lack redshift information and were not considered). As discussed above, this is largely due to the large flux limit of the 1 Jy sample; furthermore, with no cut in redshift, it contains a number of high-z BL Lacs that bias the sample toward more powerful objects.
However, we note that there is some overlap between the two populations. Six of the objects belong to both samples (1418+546, 1514−241, 1652+398, 1807+698, 2200+420, 2254+074); indeed, these are well known objects, such as BL Lac itself, Mkn 501, and 3C 371. By contrast, most of the weakest HBL lack radio images on the parsec and/or kiloparsec scale.

Table 3.1. Objects in the Sample

Num.	Name (IAU)	Name (other)	z	RA	Dec	Class	Sample
1	0145+138		0.125	01 48 29.7	+14 02 18	H	Slew
2	0229+200		0.140	02 32 48.4	+20 17 16	H	HEAO-A3
3	0347−121		0.188	03 49 23.2	−11 59 27	H	HEAO-A3
4	0350−371		0.165	03 51 53.8	−37 03 46	H	EMSS
5	0521−365		0.055	05 22 58.0	−36 27 31	L	HEAO-A3
6	0548−322		0.069	05 50 40.8	−32 16 18	H	HEAO-A2
7	0706+591		0.125	07 10 30.0	+59 08 20	H	HEAO-A3
8	0806+524		0.137	08 09 49.1	+52 18 59	H	Slew
9	0829+046		0.180	08 31 48.9	+04 29 39	L	HEAO-A3
10	0927+500		0.188	09 30 37.6	+49 50 26	H	Slew
11	1101+384	Mkn 421	0.031	11 04 27.3	+38 12 32	H	HEAO-A3
12	1133+704	Mkn 180	0.046	11 36 26.4	+70 09 27	H	HEAO-A3
13	1212+078		0.136	12 15 10.9	+07 32 04	H	Slew
14	1215+303		0.130	12 17 52.1	+30 07 01	H	Slew
15	1218+304		0.182	12 21 21.9	+30 10 37	H	HEAO-A2
16	1229+643		0.164	12 31 31.4	+64 14 18	H	EMSS
17	1255+244		0.141	12 57 31.9	+24 12 40	H	Slew
18	1418+546	OQ 530	0.152	14 19 46.6	+54 23 15	L	PG
19	1426+428		0.129	14 28 32.6	+42 40 21	H	HEAO-A3
20	1440+122		0.162	14 42 48.2	+12 00 40	H	Slew
21	1514−241	AP Lib	0.049	15 17 41.8	−24 22 19	H	1 Jy
22	1652+398	Mkn 501	0.034	16 53 52.2	+39 45 37	H	1 Jy
23	1728+502	I Zw 187	0.055	17 28 18.6	+50 13 10	H	HEAO-A3
24	1807+698	3C 371	0.051	18 06 50.6	+69 49 28	L	1 Jy
25	1959+650		0.048	19 59 59.8	+65 08 55	H	HEAO-A3

Table 3.1 (cont'd)

Num.	Name (IAU)	Name (other)	z	RA	Dec	Class	Sample
26	2200+420	BL Lac	0.070	22 02 43.3	+42 16 40	L	1 Jy
27	2201+044		0.027	22 04 17.6	+04 40 02	L	HEAO-A3
28	2254+074		0.190	22 57 17.3	+07 43 12	L	1 Jy
29	2344+514		0.044	23 47 04.8	+51 42 18	H	Slew
30	2356−309		0.165	23 59 07.8	−30 37 40	H	HEAO-A3

Note. — Col. 7: H – High frequency peaked BL Lac, L – Low frequency peaked BL Lac. Col. 8: 1 Jy (Stickel et al., 1991); HEAO-A2 (Piccinotti et al., 1982); HEAO-A3 (Remillard et al., 1999); EMSS (Morris et al., 1991); Slew (Schachter et al., 1993; Perlman et al., 1996)

3.4 A summary of host galaxy properties

For these low-z objects it was possible with the Hubble Space Telescope to investigate features and structures in the host galaxy that are undetectable with ground-based observations (Falomo et al., 2000). The host galaxy can be investigated within less than 1 kpc from the nucleus (corresponding to $\sim$0".3 at $z = 0.2$). In particular it is possible to search for slight offsets of the nucleus with respect to the galaxy center, to determine the presence of sub-components in the host galaxy, to investigate the detailed shape of the isophotes, and to search for dust features and close companions.

The detailed analysis of HST images indicates that, in spite of the presence of the active nucleus, the host galaxy appears in most cases to be a completely "normal" elliptical. Both the ellipticity and the isophotal shape distributions are similar to those for radio galaxies and radio-quiet ellipticals. This suggests that tidal interactions are very infrequent or are short-lived with respect to the nuclear activity time scale.

There are no indications of displacements and/or off-centering of the galaxy isophotes with respect to the nucleus, meaning that the unresolved nuclear source truly sits in the center of the galaxy. This rules out the micro-lensing hypothesis for BL Lacs, which predicts frequent offsets for the nucleus with respect to the host galaxy.

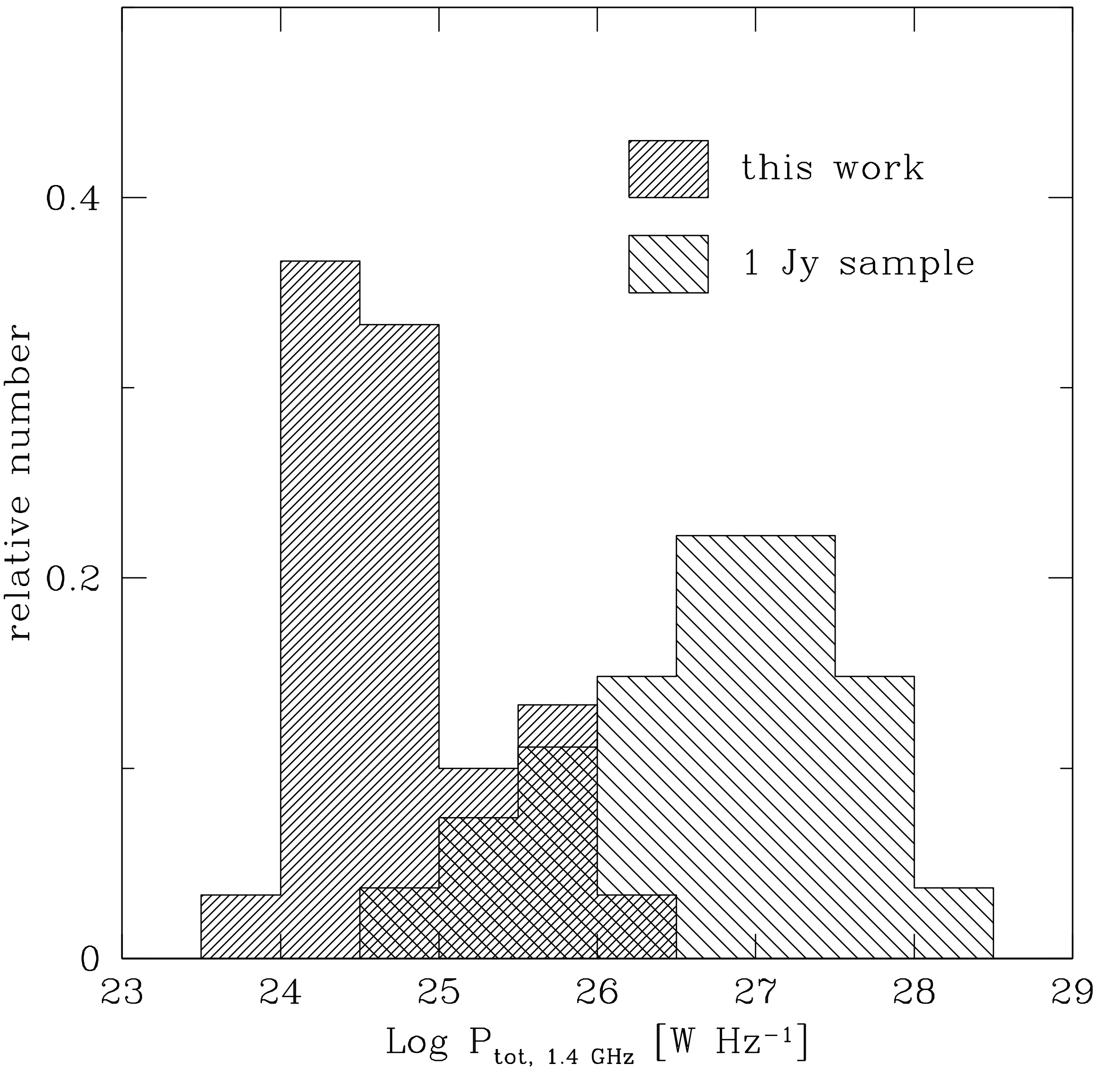

Figure 3.1 Histogram of total power distribution at 1.4 GHz for objects in our sample and in the 1 Jy sample. Data from the NVSS survey (Condon et al., 1998) for our sample and from Rector & Stocke (2001) for the 1 Jy sample.

The HST images have consistently shown that BL Lac hosts are virtually all massive ellipticals (average luminosity $M_R = -23.7 \pm 0.6$ and effective radius $R_e = 10$ kpc) located in poor groups. Moreover, these data have shown that no significant difference is present between the hosts of HBL and those of LBL, in spite of the remarkable difference of their SED (Urry et al., 2000).

There are some objects in the sample presenting interesting features in the HST images: 0521−365, 1807+698, and 2201+044 possess an optical synchrotron jet (Scarpa et al., 1999b, and references therein), while 0145+138 does not present any compact core (Scarpa et al., 2000); this makes its classification as a BL Lac questionable and we discuss this issue in Sect. 5.1. As for peculiarities in the host galaxy, we have noted that most objects are extremely regular and undisturbed; two possible exceptions are discussed by Scarpa et al. (1999a): 0806+524 is hosted in a galaxy containing an uncommon arclike structure and 1959+650 resides in a gas-rich elliptical galaxy, possessing a prominent dust lane of $\sim 5 \times 10^5 M_\odot$. Finally, compact and/or resolved companions are present in nine sources, which corresponds to an incidence that is interestingly high (Falomo et al., 2000).

Chapter 4

Low redshift BL Lacs: radio observations

Our low redshift sample is composed of 30 objects and we want to consider their properties on both parsec and kiloparsec scale. At the low distance of the objects, one arcsecond corresponds to linear scales varying from 0.5 kpc at $z = 0.027$ (2201+044) to 3 kpc at $z = 0.190$ (2254+074). Therefore, observations with the Very Large Array (VLA) and with Very Long Baseline Interferometers (both the VLBA and the EVN) are ideal for our purposes. We describe in this chapter the details on our new observations on both scales; in total, we observed 19 objects with the VLA at 1.4 GHz (either in A or C configuration, or both), 15 objects with the VLBA at 5 GHz, 8 sources with the EVN at 1.6 GHz, and two of them also in combination with the MERLIN at 5 GHz.

We present the results for each source, shortly describing the parsec and the kpc scale morphology. Finally, we compare the average properties of the whole sample on the two scales.

4.1 Observations and data reduction

Observations were aimed at completing the imaging for all the sources in the sample, both on arcsecond (Table 4.1) and milliarcsecond (Table 4.2) scale. We present the final images in Fig. 4.1–4.6 (see Tab. 4.3 and 4.4 for image parameters). Objects with good images available in the literature were not re-observed; see Table 4.5 for a summary of references.

Table 4.1. Summary of 1.4 GHz VLA Observations

Date	Conf.	hrs.	Targets
2002 Feb 22	A	5	0706+591, 0806+524, 0829+046, 0927+500, 1133+704, 1212+078, 1218+304, 1229+643, 1255+244, 1426+428, 1728+502, 1959+650
2002 May 03	A	2.5	0145+138, 0229+200, 0347−121, 0350−371, 2254+074, 2344+514, 2356−309
2002 Oct 08	C	4.5	0145+138, 0229+200, 0347−121, 1728+502, 1807+698, 1959+650, 2254+074, 2344+514, 2356−309

4.1.1 VLA observations

We obtained observations with the NRAO Very Large Array (VLA) at 1.4 GHz on 2002 February 22 and May 3 in A configuration and on 2002 October 8 in C configuration (see Table 4.1 for a summary of the observations). In order to optimize the (u, v) coverage we observed in snapshot mode with two or three scans per source at different hour angles. On average, each source was observed for about 16 minutes after allowing for observations of calibrators and slewing of the telescope. We used the NRAO Astronomical Image Processing System (AIPS) to reduce the data and perform imaging with the standard phase self-calibration technique. Amplitude self-calibration was used only for the strongest sources ($>$ 100 mJy). The final restoring beam is typically $\sim 1.9'' \times 1.2''$ for A configuration and $\sim 15'' \times 11''$ for C configuration data; the average noise is $\sim 70\,\mu$Jy/beam and $\sim 140\,\mu$Jy/beam, respectively. Images of sources in the southern hemisphere have more elliptical beams and slightly higher noise.

In total, we imaged 19 objects with the array in A configuration and 9 in C configuration. For the eight sources observed with both arrays, we combined the two data-set using AIPS task `DBCON`. This yields better sensitivity (about a factor $\sqrt{2}$) and intermediate resolution. However, the (u, v)-coverage is not optimal, and the process of self-calibration can fail to converge, especially when extended flux detected in C configuration is over-resolved by the A array. For this reason, we only present images for five sources (0145+138, 0229+200, 0347−121, 1959+650, and 2356−309).

Table 4.2. Summary of 5 GHz VLBA Observations

Date	hrs	Targets
2002 Feb 17	6	0145+138, 0229+200, 0347−121, 0350−371, 2344+514, 2356−309
2002 Feb 18	4	0521−365, 0548−322, 0706+591, 0806+524
2002 Feb 19	5	1212+078, 1218+304, 1229+643, 1255+244, 1440+122

4.1.2 VLBA observations

Very Long Baseline Interferometry (VLBI) observations have been performed with the NRAO Very Long Baseline Array (VLBA) for 15 sources on 2002 February 17, 18, and 19, at a frequency of 5 GHz (see Table 4.2 for a summary of the observations). A single VLA antenna was substituted for the VLBA antenna at Pie Town. We recorded 4 IFs in full polarizations and the data were correlated in Socorro. Data reduction was performed in AIPS. Often, the VLA observations in A configuration provided us with new and precise position measurements. Since we had good positions for our target sources, we were able to avoid fringe-fitting the data, which fails on weak sources.

On average, we have 45 minutes of useful data for each source, providing a nominal thermal noise of $\sim 0.11\,\mathrm{mJy\,beam^{-1}}$. All our images have noise figures within a factor 2 from this. All sources are detected above the 3σ level, even the weakest. For 6 sources, a detection was the most that could be accomplished. For the remaining 9 sources, we imported the (u, v) data into Difmap (Shepherd, Pearson, & Taylor, 1994, 1995) for further self-calibration and imaging.

4.1.3 EVN and MERLIN observations

We observed eight BL Lacs with the European VLBI Network (EVN) at 18 cm in single polarization on 2002 June 7th. The objects are 0706+591, 0806+524, 1133+704, 1215+303, 1218+304, 1229+643, 1426+428, and 1728+502. The stations involved were Effelsberg (100 m), Jodrell Bank (MkII, 25 m), Medicina (32 m), Noto (32 m), Onsala (25 m), Shangai (25 m), Torun (32 m), Westerbork (14×25 m), and Urumqi (25 m). Each source was observed for $\sim$ 55 minutes, divided into four scans at different hour angle; this yields a good (u, v) coverage and an average beam

Table 4.3. Image Parameters

	VLA (A conf.)		VLA (C conf.)		VLBA		EVN	
Name	noise	peak	noise	peak	noise	peak	noise	peak
0145+138	0.15	2.8	0.24	11.2	0.55	3.5	...	
0229+200	0.30	40.4	0.35	52.9	0.49	15.7	...	
0347−121	0.30	8.7	0.50	10.4	0.53	7.7	...	
0350−371	0.30	22.3	...		0.72	11.9	...	
0521−365	...		...		5.50	1034.9	...	
0548−322	...		...		0.90	33.3	...	
0706+591	0.15	62.6	...		0.38	33.2	0.5	33.5
0806+524	0.20	157.6	...		0.38	78.9	2.0	98.0
0829+046	0.25	736.2	...		...		...	
0927+500	0.11	19.9	...		...		...	
1133+704	0.18	111.6	...		...		3.0	67.2
1212+078	0.12	83.2	...		0.36	33.1	...	
1215+303	...		...		...		1.0	224.5
1218+304	0.20	65.6	...		0.41	44.1	1.0	48.7
1229+643	0.12	53.0	...		0.61	19.6	1.3	44.1
1255+244	0.10	6.5	...		0.55	2.9	...	
1426+428	0.10	31.9	...		...		1.4	28.8
1440+122	...		...		0.47	17.1	...	
1728+502	0.30	201.0	0.30	196.7	...		1.0	107.4
1807+698	...		0.60	1348.8	...		...	
1959+650	0.25	198.5	0.24	241.2	...		...	
2254+074	0.30	407.0	0.90	490.4	...		...	
2344+514	0.30	195.8	0.40	220.2	0.39	89.7	...	
2356−309	0.25	39.2	0.30	40.2	0.66	14.2	...	

Note. — Noise levels (3σ) and peak flux densities for Fig. 4.1 and 4.2 (Col. 2, 3), for Fig. 4.4 (Col. 4, 5), for Fig. 4.5 (Col. 6, 7), and for Fig. 4.6 (Col. 8, 9). All units are mJy/beam.

Table 4.4. Summary of 5 GHz EVN+MERLIN Observations (2002 May 26th)

Source	Array	beam (mas × mas)	BPA (°)	Noise $\left(\frac{\mathrm{mJy}}{\mathrm{beam}}\right)$	Peak $\left(\frac{\mathrm{mJy}}{\mathrm{beam}}\right)$
1215+303	MERLIN	52×55	29	0.35	315
	EVN+MERLIN	8.2×11.7	12	0.40	294
	EVN	1.9×5.2	7	0.38	274
1728+502	MERLIN	47×51	−31	0.40	163
	EVN+MERLIN	6.4×7.6	38	0.27	116
	EVN	1.6×2.2	15	0.43	92

of 10.1 mas × 4.5 mas. The data were correlated at the Joint Institute for VLBI in Europe (JIVE) in Dwingeloo. We imported the data in AIPS and performed the a priori calibration. Finally, we edited the data and produced the images within DIFMAP; the peak and the 3σ noise levels are reported in Table 4.3.

We also observed 1215+303 and 1728+502 at 6 cm with the EVN and the MERLIN simultaneously on 2002 May 26th. The EVN array involved in the experiment includes the same telescopes of the EVN only observation, plus the 32 m antenna in Cambridge; this antenna provides a baseline to Jodrell Bank, common to the MERLIN array as well. Each source was observed for 6 hours, in 42 scans, switching between the two targets. The MERLIN data have been processed at Jodrell Bank Observatory with the local `dprograms`; DIFMAP has been used to produce the images. The EVN data were correlated in Dwingeloo and reduced in the standard manner within AIPS (for initial calibration) and DIFMAP (for the imaging part). Finally, the combination of the two dataset has been done within AIPS, using the task `DBCON`. For the combined dataset, we have modified the weights of the original data, in order to optimize the compromise between resolution and sensitivity, by means of the adverb `REWEIGHT` in `DBCON`; in particular, the EVN data have been rescaled by a factor of 20.

4.2 Results

4.2.1 arcsecond scale

We present our final images in Fig. 4.1–4.4 (see Tab. 4.3 for image parameters) and a list of flux densities for all objects in Tab. 4.5. We also include low frequency (325 MHz) data (Column 3), as measured in the Westerbork Northern Sky Survey (WENSS, Rengelink et al., 1997) or from the Texas Survey (Douglas et al., 1996). For sources lacking flux density measurement from both surveys, we estimate the flux density from the NRAO VLA Sky Survey (NVSS, Condon et al., 1998) assuming the average spectral index obtained from other sources, i.e. $\alpha = 0.11$. This is a sensible choice as all values obtained are below the sensitivity threshold (or out of the sky coverage) of both surveys. For 0521$-$365 only, whose radio data is missing because of its location, we interpolate the large number of measured fluxes available in the literature from 80 MHz to 8800 MHz. Columns 5 and 6 give the total and core flux densities at 1.4 GHz, and Column 7 lists the ratio between these values. For the sake of homogeneity, the total flux densities are all measured on data from the NVSS. We used however information from our higher resolution observation in order to separate possible contribution from confusing sources: the A array images show that this is needed only in 0145+138, in which we therefore subtracted 8 mJy from the NVSS total. For objects observed also in C configuration, we consider the total flux density measured on our images as well. The deviation from the NVSS datum is always within $\pm$10%, without any suggestion that the NVSS systematically overestimates the total flux density. The core value has been measured using `JMFIT` in AIPS on our A configuration images (or from the literature, as given in the notes). In general, the core is the strongest component and accounts for most of the flux. In two objects (1418+546 and 1514$-$241), the core flux density is even larger than the total; this is probably due to variability of the core. On the other extreme, there are a number of sources (10/30) where a significant fraction of flux ($> 50\%$) is found in extended regions or in secondary components. We report the core flux density at 5 GHz in Col. 8 and a reference in Col. 9. Finally, in Col. 10 we classify sources according to their arcsecond scale morphology. We find 9 sources where the core is the dominant component; 8 objects with a core-jet morphology; 4 with a core-halo morphology; 7 objects with more than one compact component – possibly a hot spot or a background source; and 2 objects (0548$-$322 and 0829+047) which are located

Table 4.5. Flux Densities

N.	Name (IAU)	z	$S_{325\mathrm{MHz}}$ (mJy)	$S_{\mathrm{t,1.4GHz}}$ (mJy)	$S_{\mathrm{c,1.4GHz}}$ (mJy)	c/tot	$S_{\mathrm{c,5GHz}}$ (mJy)	ref.	type
1	0145+138	0.125	42 ± 8[a]	35.8	3	0.08	2.1	(1)	j
2	0229+200	0.140	110 ± 22[a]	94.2	42	0.44	45	(1)	x
3	0347−121	0.188	30 ± 6[a]	25.7	9	0.35	8.4	(1)	j
4	0350−371	0.165	46 ± 9[a]	40.1	23	0.57	17	(2)	c
5	0521−365	0.055	42920 ± 480[b]	17620	3124[d]	0.18	2581	(3)	x
6	0548−322	0.069	1463 ± 293[c]	505	76[e]	0.15	68	(4)	w
7	0706+591	0.125	371 ± 3.8	160	65	0.41	80	(5)	j
8	0806+524	0.137	165 ± 4.1	183	160	0.87	172	(1)	c
9	0829+046	0.180	671 ± 31[c]	1257	643[d]	0.51	1230	(6)	w
10	0927+500	0.188	12 ± 3.7	22.3	21	0.94	15	(7)	c
11	1101+384	0.031	1374 ± 3.3	889	548[e]	0.62	640	(8)	j
12	1133+704	0.046	529 ± 5.2	337	115	0.34	125	(9)	h
13	1212+078	0.136	175 ± 35[a]	150	85	0.57	94	(5)	c
14	1215+303	0.130	1175 ± 2.9	593	355[d]	0.60	445	(10)	h
15	1218+304	0.182	82 ± 2.7	71.3	67	0.94	56	(10)	c
16	1229+643	0.164	72 ± 3.7	63	55	0.87	42	(11)	c
17	1255+244	0.141	19 ± 4[a]	16.6	6.5	0.39	6.9	(1)	c
18	1418+546	0.152	962 ± 3.4	835	1058[d]	1.27	1189	(12)	x
19	1426+428	0.129	64 ± 3.1	61.3	32	0.52	22	(9)	h
20	1440+122	0.162	80 ± 16[a]	68.5	60	0.87	41	(1)	c
21	1514−241	0.049	1792 ± 43[c]	2177	2562[d]	1.18	1480	(13)	x
22	1652+398	0.034	1936 ± 4.7	1630	1376[d]	0.84	1250	(8)	j
23	1728+502	0.055	317 ± 4.2	232	200	0.86	134	(9)	j
24	1807+698	0.051	4015 ± 4.4	2129	1350[d]	0.63	1507	(14)	h
25	1959+650	0.048	252 ± 3.5	260	200	0.77	252	(1)	j

in rich clusters and are clearly wide-angle-tail (WAT) radio sources.

The objects span a range in total power of about 2.5 orders of magnitude at 1.4 GHz. The weakest object is 1255+244, which has $\mathrm{Log}P_{\mathrm{t}} = 23.88\,\mathrm{W\,Hz^{-1}}$; while the most powerful is 0521−365, with $\mathrm{Log}P_{\mathrm{t}} = 26.07\,\mathrm{W\,Hz^{-1}}$.

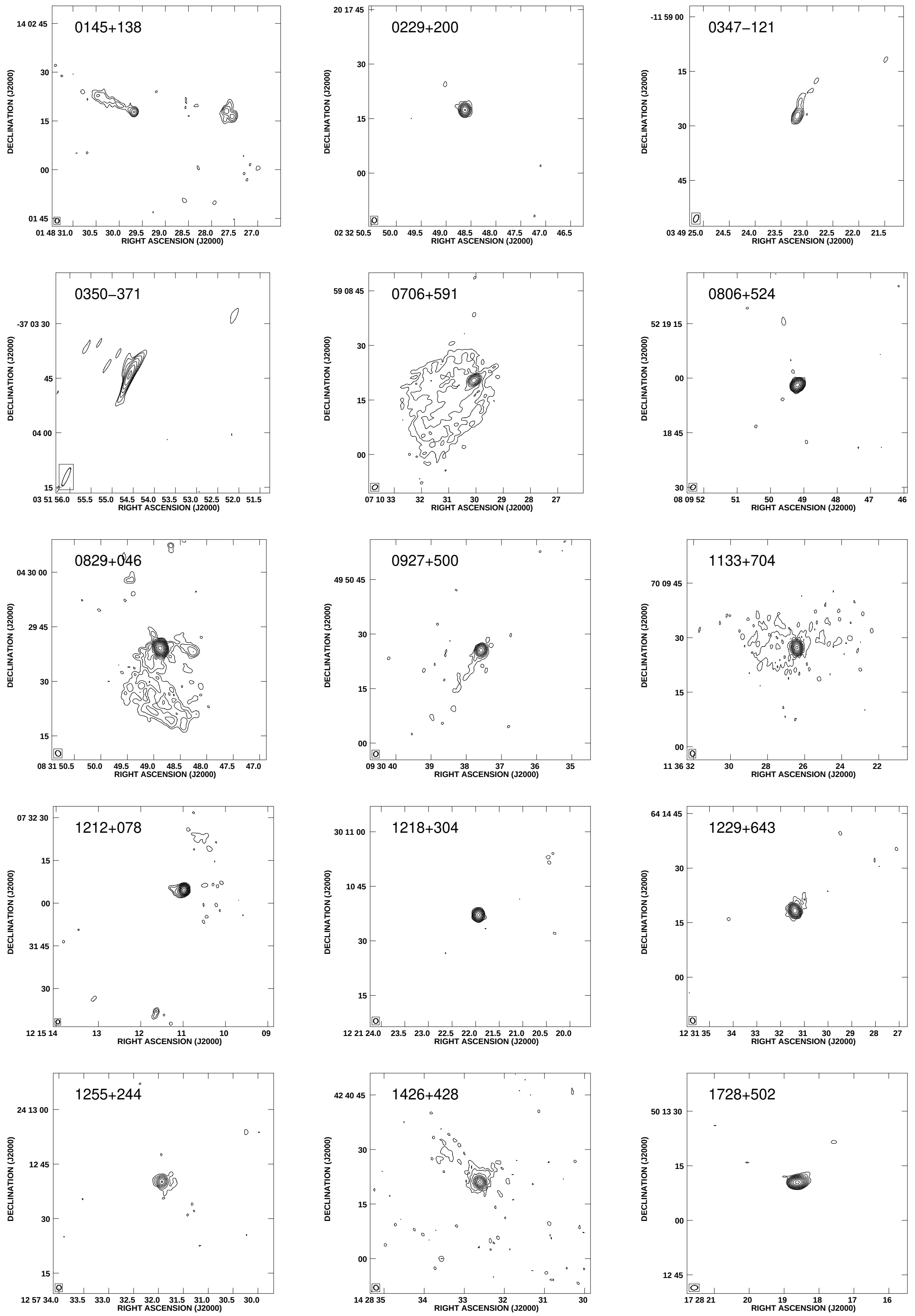

Figure 4.1 VLA images taken in A configuration page 1 of 2. Contours are drawn at (1, 2, 4, 8, 16, ...) times the noise level. Noise levels and image peaks are given in Tab. 4.3.

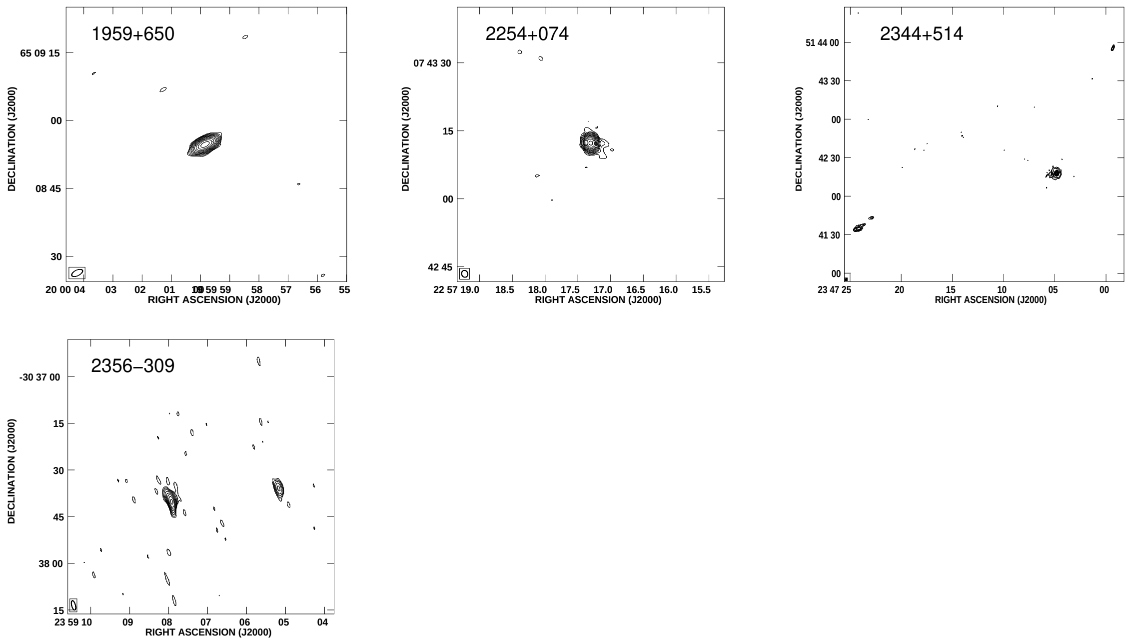

Figure 4.2 VLA images taken in A configuration continued. Contours are drawn at (1, 2, 4, 8, 16, ...) times the noise level. Noise levels and image peaks are given in Tab. 4.3.

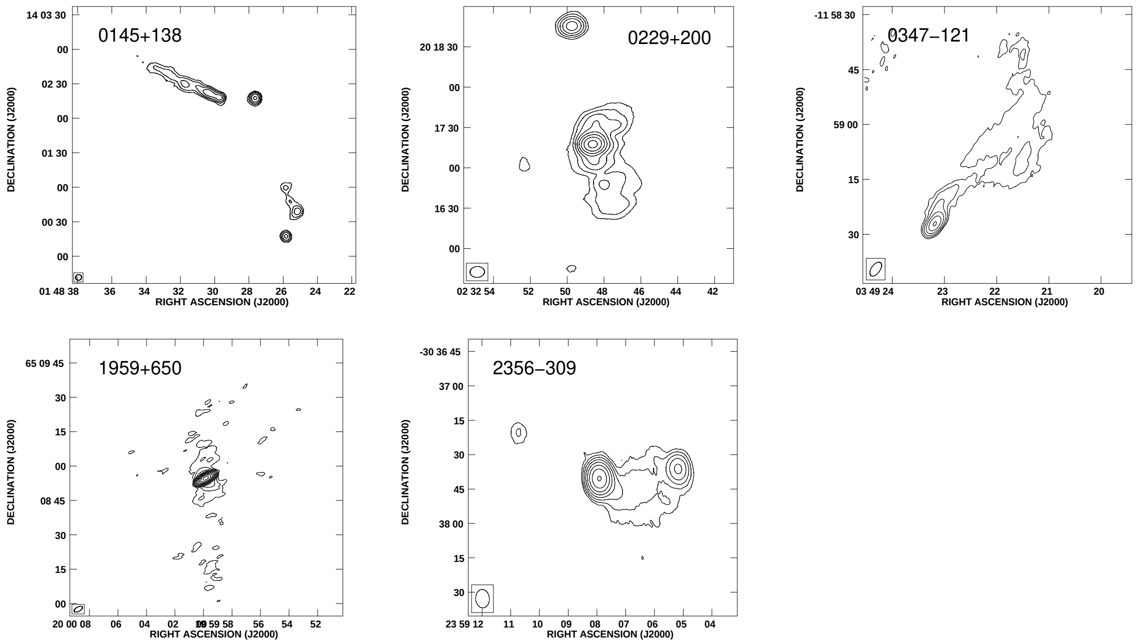

Figure 4.3 VLA images made from a combination of data from the A and C configurations.

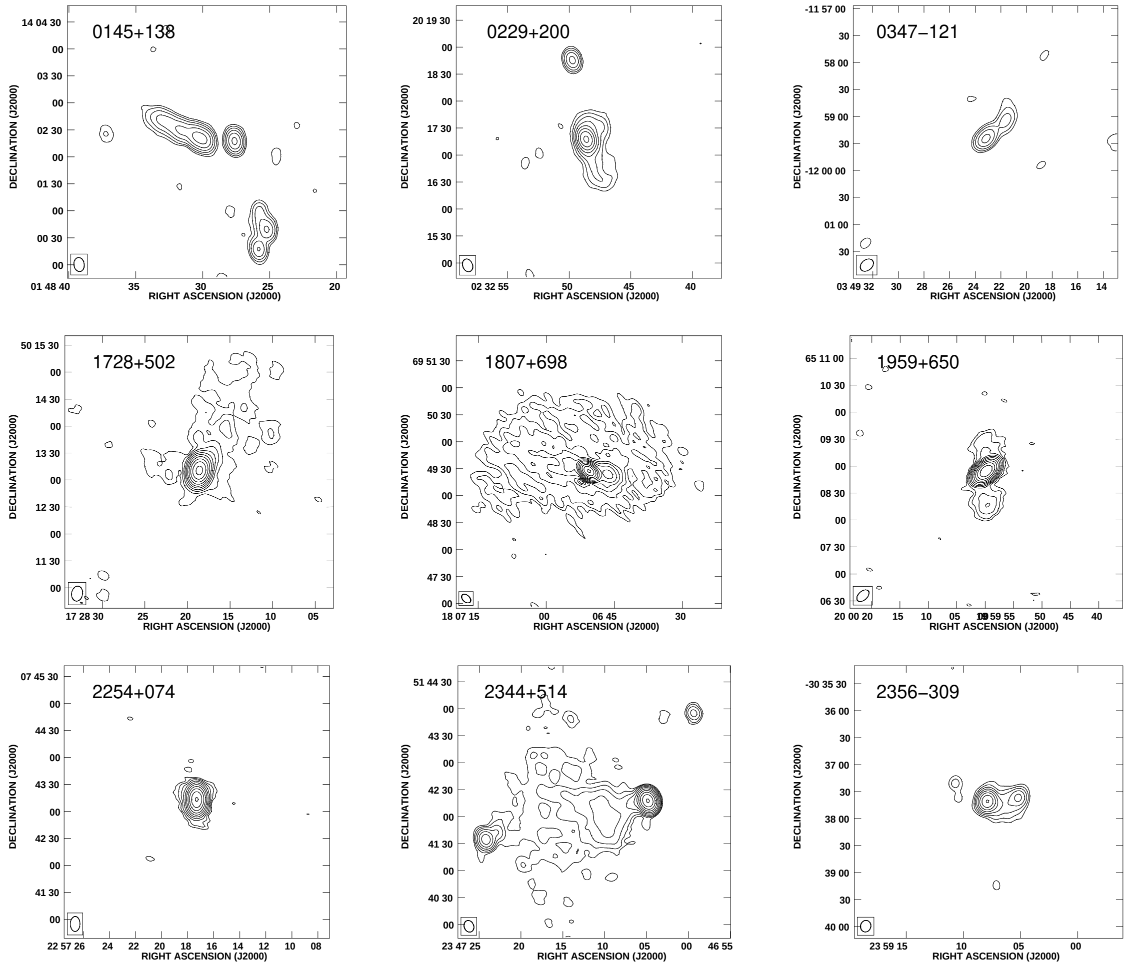

Figure 4.4 VLA images taken in C configuration. Contours are drawn at (1, 2, 4, 8, 16, ...) times the noise level. Noise levels and image peaks are given in Tab. 4.3.

Table 4.5 (cont'd)

N.	Name (IAU)	z	$S_{325\mathrm{MHz}}$ (mJy)	$S_{\mathrm{t,1.4GHz}}$ (mJy)	$S_{\mathrm{c,1.4GHz}}$ (mJy)	c/tot	$S_{\mathrm{c,5GHz}}$ (mJy)	ref.	type
26	2200+420	0.070	1819 ± 4.1	6250	3310[d]	0.53	4857	(10)	x
27	2201+044	0.027	1222 ± 58[c]	835	179[d]	0.21	168	(9)	j
28	2254+074	0.190	405 ± 25[c]	404	405	1.00	1216	(10)	c
29	2344+514	0.044	569 ± 4.2	410	196	0.48	212	(1)	x
30	2356−309	0.165	75 ± 15[a]	66.2	39	0.59	29	(5)	x

Note. — Col. 4: total source flux density at 325 MHz from the WENSS, except as noted: (a) extrapolated from the 1.4 GHz flux density (Col. 5) with $\alpha = 0.11$, (b) interpolated from NED data between 80 and 8800 MHz, (c) Texas Survey (Douglas et al., 1996). Col 5: total source flux density at 1.4 GHz from the NVSS. Col 6: arcsecond core flux density at 1.4 GHz from VLA A configuration data or (d) Antonucci & Ulvestad (1985), (e) Laurent-Muehleisen et al. (1993). Col. 7: ratio between core and total flux density at 1.4 GHz. Col 8: arcsecond core flux density at 5 GHz, with references as given in Col. 9. Col. 9: (1) Perlman et al. (1996), (2) Veron-Cetty & Veron (1993), (3) interpolated from data between 1.4 GHz and 15 GHz, (4) Reid et al. (1999), (5) NED, (6) MERLIN archive data, (7) Nass et al. (1996), (8) Giovannini et al. (2001), (9) Laurent-Muehleisen et al. (1993), (10) Fossati et al. (1998), (11) Padovani & Giommi (1995), (12) Murphy et al. (1993), (13) Morganti et al. (1993), (14) Cassaro et al. (1999). Col. 10: (c) unresolved; (j) core+jet(s), (h) core+halo, (x) extended, complex structure, (w) wide angle tail

4.2.2 milliarcsecond structure

On parsec scales, our VLBA 5 GHz observations have a typical resolution of $\sim 3.8 \times 1.5$ mas. Figure 4.5 presents the images; Table 4.6 summarizes the most significant parameters: peak flux density, total intensity, presence of a jet, and jet position angle (PA).

All objects are dominated by a strong, compact component. In five sources this component is responsible for all the correlated flux density and in two cases (0548−322 and 1440+122) there is little ($\sim 10\%$) flux density in extended structures that we could not image. Short one-sided jets (typically < 10 mas) are present in seven sources and only 0521−365 presents a longer jet; in any case, the core is always the strongest component. No counter-jet is detected in any of the sources.

The 1.6 GHz EVN observations (average beam 10.1 mas $\times$ 4.5 mas, Fig. 4.6) yield similar results: the compact core makes up the largest fraction of the total flux density; jets are detected in six out of eight sources, always single sided. The rate of jet detection is slightly higher in the EVN observations, which have both longer exposure and brighter targets. This is suggestive that jets are present in all sources but deep observations are required to reveal them. Finally, Fig. 4.7 presents the EVN+MERLIN images of 1215+303 and 1728+502 at 5 GHz. These sources possess bright cores and long (> 100 mas) one-sided jets. The jets are well aligned on scales from a few to some hundreds of parsecs.

We have model-fitted the visibilities of both VLBA and EVN data in DIFMAP. In most cases, we need only one component (in addition to the core) to describe the jet. When two or more components are required, they usually align on a straight path, without showing significant bending. We use the results of our model-fit to determine the jet brightness B_j and the jet/counter-jet ratio R_min, which are presented in Columns 7 and 9 of Table 4.6. Since no object in the sample has a detectable counter-jet, the values presented are only lower limits based on the noise of the images. This is also true for objects with values derived from literature data (see notes to Table 4.6).

For the six objects that have both a 5 GHz (either VLBA or EVN) and 1.6 GHz EVN observations (0706+591, 0806+524, 1215+303, 1218+304, 1229+649, and 1728+502), we compare the results. Details are given along with the source description in Sect. 4.3; however, we can summarize the main results as follows:

- **cores:** the peak of the images are always higher in the EVN images, by less than 1% in 0706+591 to more than 100% in 1229+649 (see Table 4.3); if we consider the DIFMAP model-fits for the core component, similar results are obtained. Clearly, the different observing frequency brings about this excess mostly as a result of the different size of the synthesized beams. For a spectral index measurement, we therefore consider our 5 GHz images (either VLBA or EVN), limiting the $(u,v)-$range to $0-40$ Mλ; this yields a resolution comparable to the 1.6 GHz images. Results are presented in Table 4.7, with $\alpha^{5}_{1.6}$ in the range between -0.1 and 0.5. Note that the observations at 1.6 and 5 GHz are not simultaneous, so variability can account for part of the differences.

- **jets:** except for 1229+649, which has only a 3σ tentative jet detected, all the sources display single-sided jets in both VLBA and EVN data. The jet position angles present some difference; since the jets at 1.6 GHz have PA measured at larger distance, this is suggestive of the presence of some bending, though of

Table 4.6. VLBI data @5 GHz

n	Name	z	S_t (mJy)	S_c (mJy)	$\frac{S_{\rm t,mas}}{S_{\rm c,''}}$	B_j $\left(\frac{\rm mJy}{\rm beam}\right)$	PA$_{\rm jet}$ (°)	R (≥)	$\beta\cos\theta$ (≥)	ref.
1	0145+138	0.125	3.3	3.2	1.61	···	···	···	···	(1)
2	0229+200	0.140	18.2	17.0	0.40	···	···	···	···	(1)
3	0347−121	0.188	8.5	8.1	1.01	···	···	···	···	(1)
4	0350−371	0.165	16.9	14.0	0.99	2.40	46	8	···	(1)
5	0521−365	0.055	1747	995.0	0.68	142.5	−44	119	0.74	(1)
6	0548−322	0.069	41.7	36.3	0.61	···	···	···	···	(1)
7	0706+591	0.125	42.0	33.8	0.53	3	−158	25	···	(1)
8	0806+524	0.137	136.8	66.0	0.80	40	20	333	0.82	(1)
9	0829+046	0.180	740	440.0	0.60	90	65	90	···	(2)
10	0927+500	0.188	···	···	···	···	···	···	···	
11	1101+384	0.031	400	200	0.63	10	−32	100	0.73	(3)
12	1133+704	0.046	137.9	82.7	1.10	9.5	105	16	···	(4)
13	1212+078	0.136	50.0	34.5	0.53	3.0	92	23	···	(1)
14	1215+303	0.130	372.0	276.0	0.84	9.4	140	157	0.77	(3)
15	1218+304	0.182	56.9	39.8	1.02	3.2	73	25	···	(1)
16	1229+643	0.164	35.7	26.9	0.85	5.0	−43	28	···	(1)
17	1255+244	0.141	2.8	2.8	0.40	···	···	···	···	(1)
18	1418+546	0.152	1090	209.0	0.92	40	120	40	···	(5)
19	1426+428	0.129	21.2	19.1	0.96	2.1	20	3	···	(4)
20	1440+122	0.162	18.5	17.2	0.45	···	···	···	···	(1)
21	1514−241	0.049	1100	1100	0.74	···	···	···	···	(6)
22	1652+398	0.034	1118	491	0.89	100	150	400	0.83	(7)
23	1728+502	0.055	171	110.0	1.28	18.0	−55	200	0.79	(3)
24	1807+698	0.051	780	560.0	0.52	50	−102	38	···	(2)
25	1959+650	0.048	220	181.7	0.87	1.6	−5	8	···	(8)

quite little amount ($\lesssim 30°$).

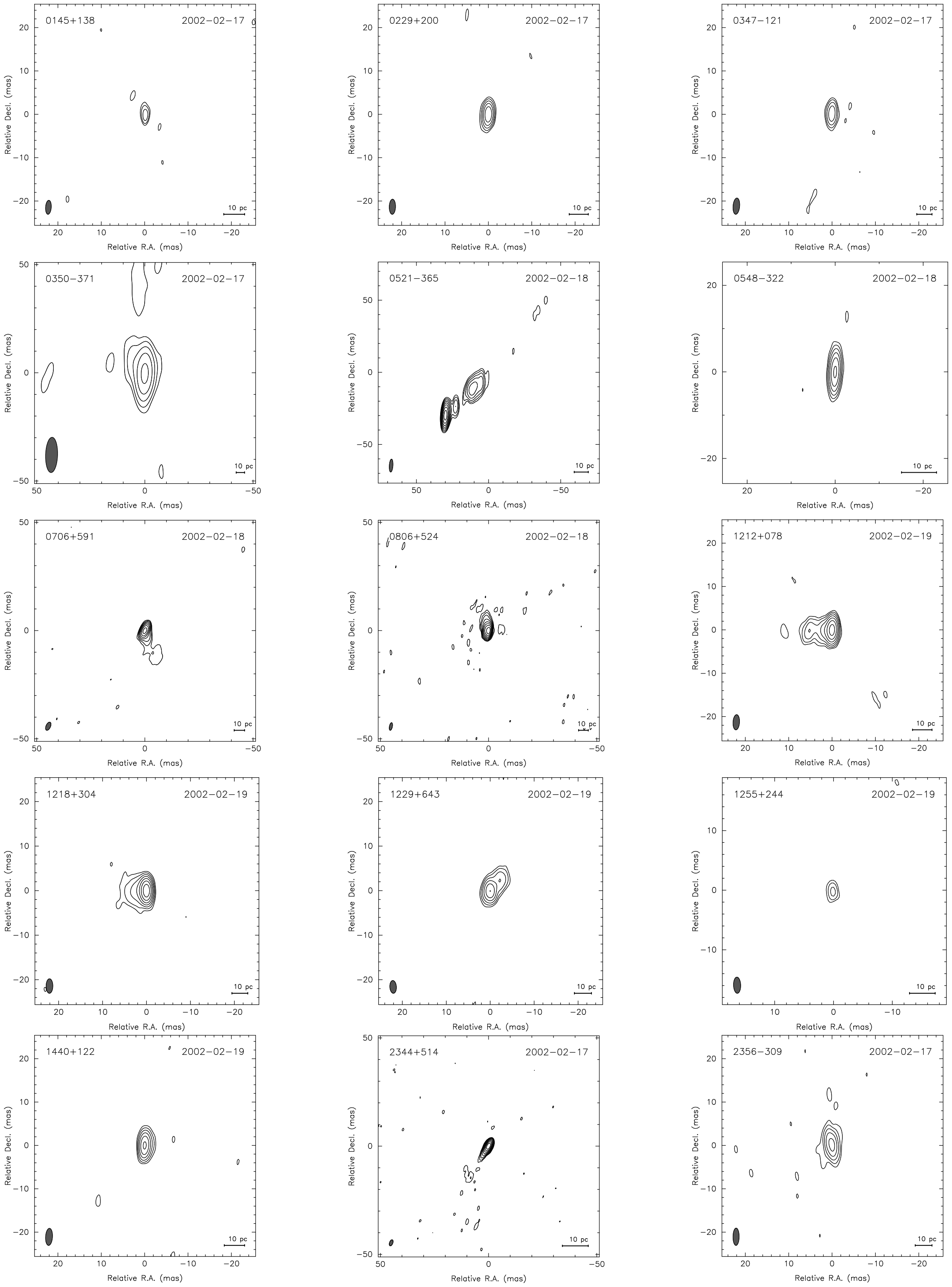

Figure 4.5 VLBA images. Contours are drawn at (1, 2, 4, 8, 16, ...) times the noise level. Noise level and image peaks are given in Tab. 4.3.

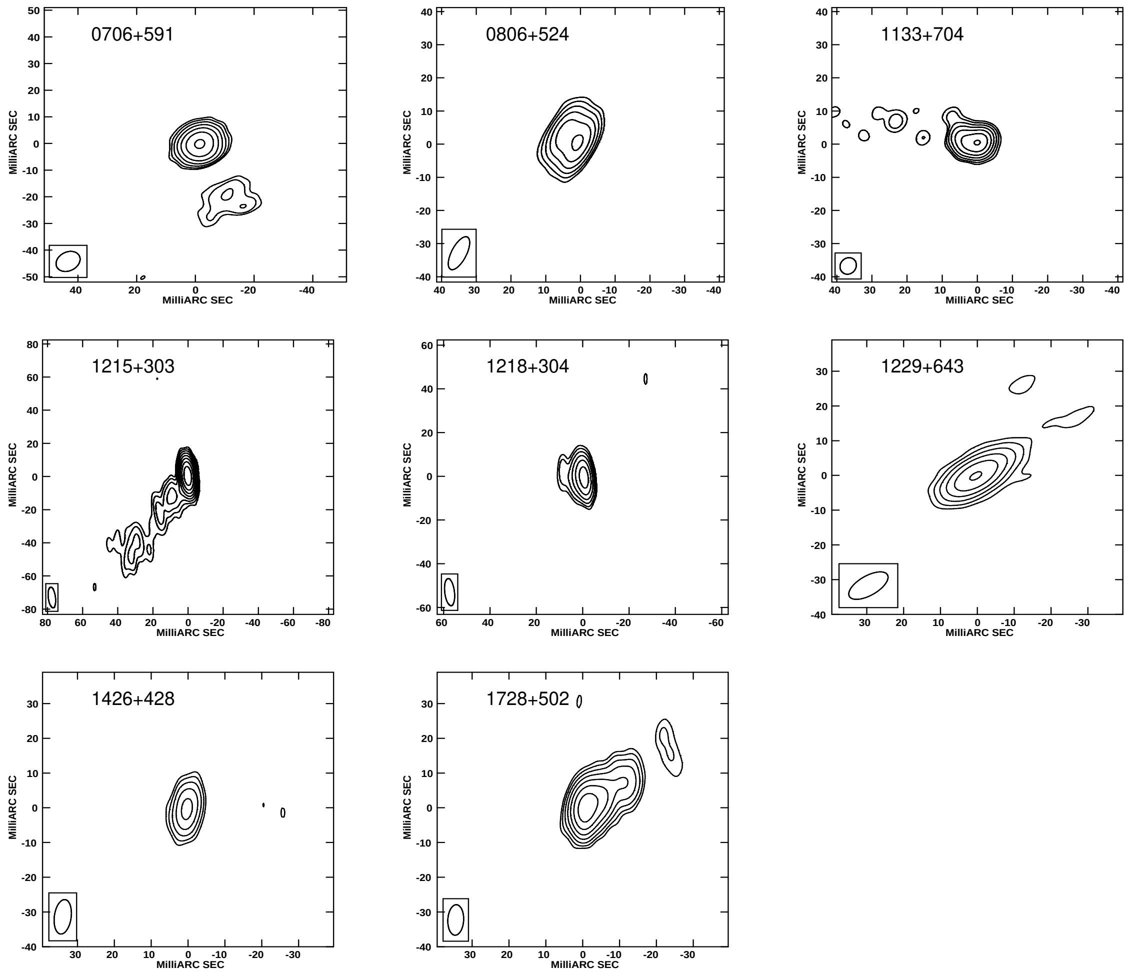

Figure 4.6 EVN images taken at 1.6 GHz on 2002 June 7. Contours are drawn at (1, 2, 4, 8, 16, ...) times the noise level. Noise levels and image peaks are given in Tab. 4.3.

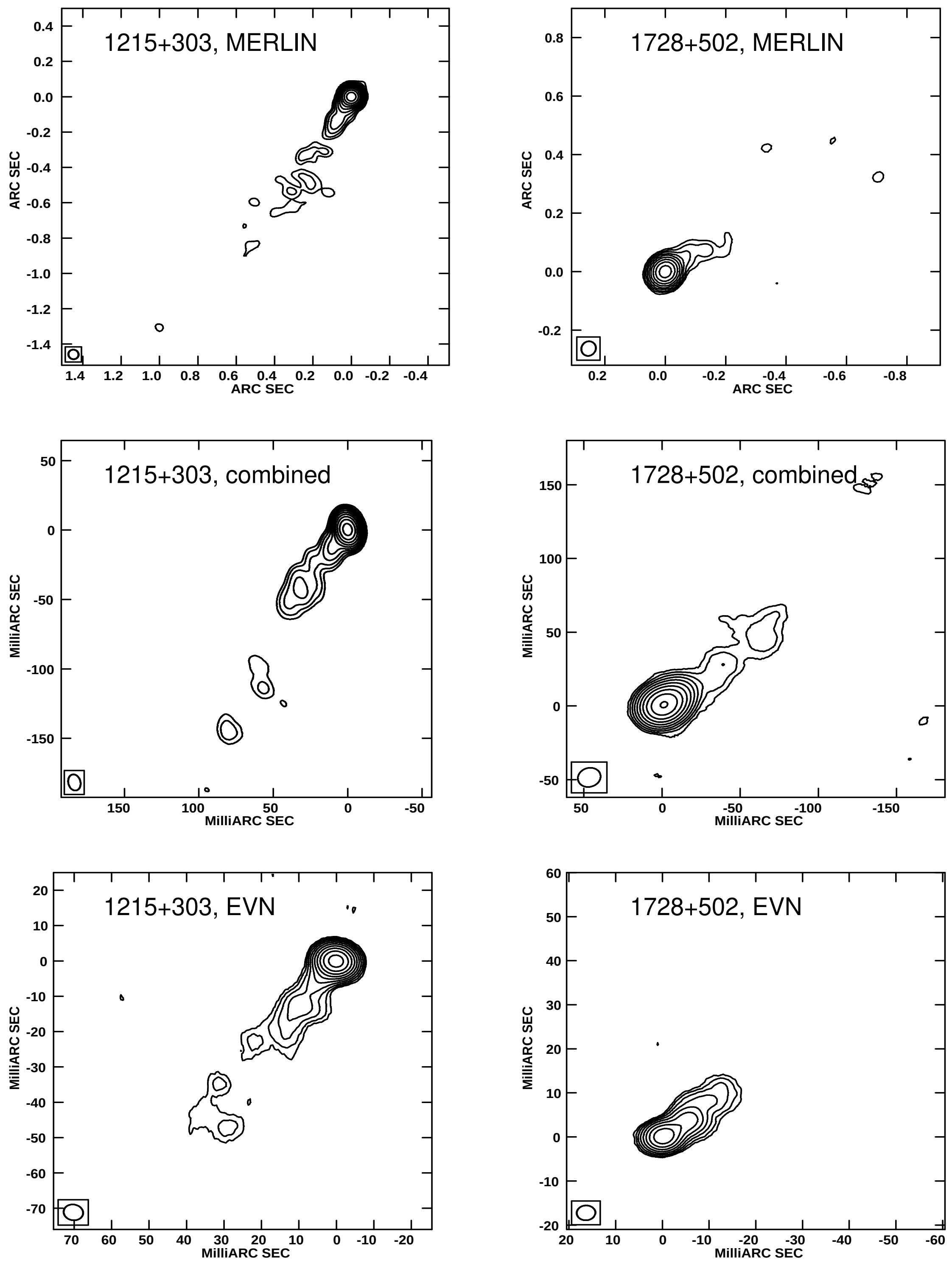

Figure 4.7 Images of 1215+303 (left) and 1728+502 (right) at 5 GHz, taken on 2002 May 26. At top are the MERLIN images, at the center the combination of MERLIN and EVN data, at bottom EVN only. Contours are drawn at (1, 2, 4, 8, 16, ...) times the noise level. Noise levels and image peaks are given in Tab. 4.4.

Table 4.6 (cont'd)

n	Name	z	S_t (mJy)	S_c (mJy)	$\frac{S_{\rm t,mas}}{S_{\rm c,''}}$	B_j $\left(\frac{\rm mJy}{\rm beam}\right)$	$\mathrm{PA_{jet}}$ (°)	R (≥)	$\beta\cos\theta$ (≥)	ref.
26	2200+420	0.070	2164	1148	0.45	300	−170	350	0.82	(9)
27	2201+044	0.027	170	131.3	1.01	3.0	−42	3	···	(4)
28	2254+074	0.190	350	280.0	0.29	38.4	−120	43	···	(2)
29	2344+514	0.044	116.7	70.0	0.55	3.0	142	25	···	(1)
30	2356−309	0.165	21.9	21.9	0.76	···	···	···	···	(1)

Note. — Col. 4: Correlated VLBI flux density at 5 GHz. Col. 5: VLBI core flux density. Col. 6: Ratio between total VLBI flux density and arcsecond core at 5 GHz (Col. 8 in 4.5. Col. 7: Jet brightness near the core. Col. 8: Jet P.A. Col. 9: Lower limit for the jet/counterjet ratio. Col. 10: Estimated lower limit for $\beta\cos\theta$. Col. 11: References – (1) this thesis (VLBA data), (2) Fey & Charlot (2000), (3) this thesis (EVN data), (4) Kollgaard et al. (1996), (5) Cassaro et al. (2002), (6) Shen et al. (1998), (7) this thesis (see Chapt. 6), (8) Rector et al. (2003), (9) Gabuzda & Cawthorne (2003)

4.2.3 Parsec/Kiloparsec scale comparisons

A comparison of the morphology on parsec and kiloparsec scales reveals in general a good agreement, and objects in the present sample do not exhibit large bending between small and large scales. There are 10 sources that bend $\leq 30°$, two between 30° and 60°, and two more are $> 60°$; for the others there is no preferred direction on either parsec or kiloparsec scale. Even with this uncertainty, this result seems to support the view proposed by Rector et al. (2003), i.e. that HBL tend to have less bent jets than LBL. It is also worth noting that all three objects showing an optical jet (0521−365, 1807+698, and 2201+044, all LBL), present straight jets as well. Therefore, with few exceptions, it seems that large bending in BL Lacs is not common; this agrees with the expectations of unified models, given the findings of Giovannini et al. (2001) that FR I radio galaxies show a good agreement between parsec and kiloparsec scale jet PA. Large bending in the jets is also unlikely in those objects presenting a core+halo morphology, such as 1133+704, 1215+303, 1426+428, 1807+698, and 2344+514. The classic explanation is that the halos are lobes seen end on, and the main axis of the object is closely aligned with the line-of-sight. This explanation argues against large bends in the jet in these sources as

Table 4.7. Core flux densities and spectral index

Source	core @1.6 GHz (mJy)	core @5 GHz (mJy)	spectral index
0706+591	35.9	36.5	0.0
0806+524	138.8	100.2	0.3
1215+303	306.3	291.6	0.0
1218+304	48.6	42.6	0.1
1229+643	48.2	25.8	0.5
1728+502	110.0	116.6	−0.1

Note. — Values are calculated considering only (u, v) data in the range $0 - 40$ Mλ. The 5 GHz data for 1215+303 and 1728+502 are from EVN observations, the others from the VLBA. All 1.6 GHz flux densities are from EVN data.

well. See for example in the next section (4.3) the note on 1215+303, whose FIRST image (Fig. 4.8) shows an unresolved core at the center of a circular halo.

In the comparison between the arcsecond core at 5 GHz and the correlated VLBI flux at the same frequency (as given in Table 4.5 and 4.6, respectively) there is a continuity of behavior – only 9 sources have integrated VLBI flux densities $\leq 60\%$ of their arcsecond core flux density. This result suggests that only a small fraction ($\sim 30\%$) of BL Lacs objects have a complex sub-arcsecond structure not visible in our data. In the majority we can follow the structure from parsec to kiloparsec scale.

Observational data suggest that beaming effects play a major role on the parsec scale and become less important on larger (kpc) scales. One clear piece of evidence is the presence of the symmetric structure on the kiloparsec scale in sources with an asymmetric parsec scale morphology. In sources discussed here we have 5 sources where VLA images suggest/show the presence of symmetric structure. They are: 0229+200, 0706+591, 0829+046, 1807+698, and 1959+650. These results imply that at a projected distance of 5-10 kpc from the core the jet velocity is no longer relativistic. On the contrary, some sources are still asymmetric in the VLA images. They are: 0145+138, 0347−121, 0927+500, and 1212+078. Assuming intrinsically symmetric jets and Doppler favoritism as the origin of observed asymmetries, the radio jets of these sources are still relativistic on scales of tens of kpc.

4.3 Notes on individual sources

0145+138 – This is one of the weakest objects ($\mathrm{Log}P_{\mathrm{tot,1.4GHz}} = 24.19\,\mathrm{W\,Hz}^{-1}$), to show a core-jet structure. The jet is unusually long ($\sim$ 200 kpc) for such a low-power object. On the opposite side of the jet at $\sim$ 25", there is a double radio source, located at the same redshift (Slinglend et al., 1998). Other nearby sources are possibly related to the foreground galaxy cluster Abell 257. Note that the total flux given in Tab. 4.5 refers to the BL Lac source only; the contribution of the nearby source has been subtracted. The VLBA image shows only a 3 mJy core in agreement with the core flux density from the VLA in A configuration. We surmise that most of the flux density in this source is from the long, one-sided jet.

0229+200 – The C-array image suggests, and the A+C image confirms, the presence of a two-sided jet, with the main jet pointing to the south, in agreement with Rector et al. (2003). About 100" to the north, we find a compact radio source not yet identified optically. The flux density of the VLBI core is $\sim$ 16 mJy; no jet is visible on the parsec scale. Thanks to a longer exposure and better (u,v)-coverage, the VLBA image by Rector et al. (2003) shows a parsec scale jet, well aligned with the kpc scale main jet.

0347−121 – This object shows in the A array image a jet in PA $-12°$; at 7" from the core the jet bends by $\sim 35°$ and expands with a large opening angle, showing in the A+C image a lobe-like structure. The VLBI image gives no indication of a parsec scale jet.

0350−371 – Because of its low declination (Dec $= -37°$), this object has a somewhat lower resolution A configuration image. There is an indication of a jet present both on arcsec and milliarcsecond scale, as an elongation of the main component to the north-east in PA 33° and 46°, respectively. This yields a small bend of $\Delta\mathrm{PA} \sim -13°$ from the parsec to the kiloparsec scale.

0521−365 – This is a nearby ($z = 0.055$), bright EGRET source (Lin et al., 1995). It is also one of the three objects in the sample with an optical jet. The optical jet is well aligned with the kiloparsec radio jet, and the radio and optical structures have a clear correspondence (Scarpa et al., 1999b). Our VLBA image shows that the same PA found in the parsec scale jet is maintained, without any significant bending, over three orders of magnitude. This suggests a relatively large angle of view, in agreement with the absence of superluminal motion showed by Tingay &

Edwards (2002) and the findings of Pian et al. (1996).

0548−322 – This southern object resides in a rich environment, with close companions and other galaxies at the same redshift (Falomo et al., 1995). This is in agreement with the wide-angle tail (WAT) structure revealed on kiloparsec scales by Laurent-Muehleisen et al. (1993) and Reid et al. (1999). The pc scale image is dominated by a 35 mJy core, with little or no other emission detected. The large difference between this value and the kpc total flux density suggests that the emission on large scales is spread over an extended low brightness area.

0706+591 – Our image in A configuration is a significant improvement in resolution with respect to the only image published so far (Laurent-Muehleisen et al., 1993). The main structure is quite extended, broad, and the core is located at the north-west edge of this quite round cocoon. It could be a tailed radio structure (WAT or NAT) viewed at a small angle of sight. Note however that there is no indication of an overdensity of galaxies in its vicinity. A small orientation angle is also suggested by the different direction of the parsec scale core-jet structure (ΔPA $\sim 80^\circ$). In fact, both the VLBA and EVN jet points at $\sim -160^\circ$ with the EVN image displaying a significant fraction of flux density in a component at $20-30$ mas.

0806+524 – This source is heavily core-dominated. It looks point-like with the VLA, with a flux density of 160 mJy/beam at 1.4 GHz. In the VLBA image, the integrated flux density at 5 GHz is 137 mJy, distributed in a core and a short (~ 5 mas), northbound (PA $\sim 13^\circ$) jet. The EVN observation at 1.6 GHz recovers a total of 182 mJy, with the jet in PA 50°.

0829+046 – This is one of the rare BL Lacs in which there is evidence of emission on both sides of the core. In the VLA A array image, two symmetric jets emerge at PA 110° (and -70°). Both jets bend, showing a radio structure typical of head-tail radio galaxies. For this reason, we believe that the large bending of the jet is related to this motion and not intrinsic to the source. This leaves us with a bend between parsec and kiloparsec scale of 44° (see VLBA image in Fey & Charlot, 2000; Lister, Marscher, & Gear, 1998).

0927+500 – This is the second most distant source in the sample and looks like a faint (~ 20 mJy), core-dominated source. No information is available on the parsec scale morphology.

1133+704 – Our observation reveals a core-halo morphology, confirming the claim

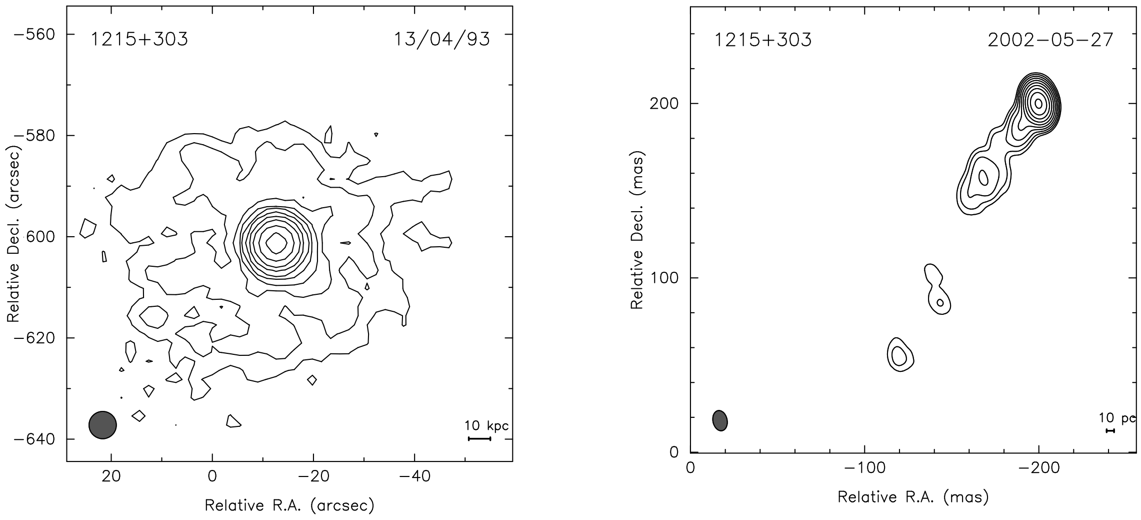

Figure 4.8 Images of 1215+303. Left: image from the FIRST survey (Becker et al. 1995); right: EVN+MERLIN at 5 GHz.

of Wardle et al. (1984). The halo is faint and heavily resolved in the image in A configuration. This explains the results of Laurent-Muehleisen et al. (1993): in their 5 GHz image, the halo is resolved out and only the compact 125 mJy core is detected. The major axis of the halo is in the east-west direction, i.e. well aligned with the EVN parsec scale jet (jet PA $\sim 71°$, see also Kollgaard et al., 1996).

1212+078 – This object presents a good alignment between the pc and kiloparsec scale structure. The jet is oriented at $\sim 90°$ and is detected for 12 mas with the VLBA and almost 50" with the VLA. Rector et al. (2003) present a VLBA image (1997 May 17) and a deep B array VLA image suggesting a transverse orientation for the extended structure. A compact feature 40 mas south of the core is present in our image as well as in the one of Rector et al. (2003). It is likely that our VLA image resolves some of the extended emission, which is also visible in Perlman et al. (1996) on the opposite side, as well as in the FIRST and NVSS images.

1215+303 (Figure 4.8) – The HBL 1215+303 is located at $z = 0.130$. For this object, a good map is available in the FIRST survey (Becker, White, & Helfand, 1995), as shown in Fig. 4.8 (left). A 377 mJy core dominates a symmetric halo structure of about 50" diameter. No preferred direction is visible on this scale, while the EVN 1.6 GHz image shows a jet oriented in PA 140°. For this reason, we consider also the EVN+MERLIN observations at 5 GHz, in order to image the inner structure out to the largest possible distance from the inner core. The right panel in Fig. 4.8 (see also Fig. 4.7) shows the long, straight, one-sided jet. The large jet/counter-jet ratio ($R \gtrsim 150$) indicates that the effects of the beaming are important in this source; indeed, one could expect a small angle to the line of sight, if the kpc halo structure were interpreted as a lobe seen end-on.

1218+304 – We confirm that this source is compact on kiloparsec scale and pose an upper limit on its size of 0.19" (0.7 kpc). The VLBA image reveals a 10 mas jet emerging at PA $\sim 90°$, confirmed by the EVN data (jet of the same length in the same PA). The total VLBI correlated flux dominates the total flux density of the source. It is 57 mJy at 5 GHz (VLBA image) and 64 mJy at 1.6 GHz (EVN data), which corresponds to a global spectral index $\alpha = 0.1$.

1229+643 – The kiloparsec scale structure shows an almost unresolved core, with a little emission from a halo-like feature. However, even if the poor signal-to-noise of this structure does not allow us to make any strong claim about its nature, we can estimate that it is oriented at a PA of $\sim -15°$. The VLBA jet points in direction north-west (PA $= -43°$) and the core-jet structure accounts for most of the flux density from this source. In the EVN image, little flux density is detected at the same position angle while most of the emission is blended in the core component at this frequency. Therefore, we tentatively propose a ΔPA $\sim 30°$.

1255+244 – This extremely weak object is only marginally resolved with the VLA, and barely detected by the VLBA ($\sim$ 3 mJy core). This is the weakest object in the sample ($P_{\rm tot,1.4GHz} = 23.5\,{\rm W\,Hz^{-1}}$)

1426+428 – The comparison of the NVSS total flux density (61 mJy) and the peak of the A array image (32 mJy/beam) indicates that some extended emission, or large variability, is present. Our VLA image confirms the presence of a faint halo surrounding the central core, but does not recover all the flux. The extension at PA $\sim 50°$ presents a ΔPA $= 30°$ with respect to the inner structure studied by Kollgaard et al. (1996), whilst the objects is unresolved in our EVN image.

1440+122 – Little information can be obtained for this object. The VLBA image reveals only a faint (15 mJy) core, possibly extended to the west. VLA images for this source have been obtained by Giovannini et al. (in prep.) and show a core-halo structure extended in the SW direction.

1728+502 – This source displays a remarkable alignment from the parsec scale EVN image out to the NVSS map, going by our MERLIN and VLA observations (see Fig. 4.7). The parsec scale jet in PA $-56°$ is still collimated on the MERLIN scale, with a little tilt east. Then, in the C array image, the emission is spread over more than 100", for a total of $\sim$ 16 mJy of extended emission. This emission is resolved in the A array image, which is dominated by the 200 mJy core.

1807+698 – This is a well known source (3C 371), with a jet detected in the optical with HST (Scarpa et al., 1999b) and in the X-rays with Chandra (Pesce et al., 2001). This jet does not bend significantly and is well aligned with the parsec scale jet imaged with the Space VLBI by Gómez & Marscher (2000) (in PA $\sim 100°$). This orientation is in good agreement with the PA of the jet visible in our C array image (ΔPA consistent with 0). We also detect a diffuse halo of about 340 mJy, and a possible counter-jet, diluted within the halo.

1959+650 – Costamante & Ghisellini (2002) suggested that this object could be a TeV source; in fact, a strong detection of very high energy γ-rays was obtained with the Whipple 10 m telescope (Holder et al., 2003). Our C array radio image clearly shows a peculiar two-sided structure. The combination of A and C data-set indicates that the symmetry could be in the jet region, suggesting that the source is oriented in the plane of the sky and/or that the jet is non-relativistic on the arcsecond scale. The parsec scale jet in the image by Rector et al. (2003) at 5 GHz has a PA of $-5°$ indicating that the jet does not change direction over three orders of magnitude. Note, however, that high frequency (15 GHz) observations suggest a 1 mas jet to the southeast, in PA $\sim 160°$(Piner & Edwards, 2004).

2254+074 – This source has one of the brightest cores ($\mathrm{Log}P_{\mathrm{c,5GHz}} = 26.1\,\mathrm{W\,Hz^{-1}}$). Only a little extended emission is present on arcsecond scale, both in the A and C configuration. A comparison to the parsec scale total flux density (350 mJy, Fey & Charlot, 2000), indicates that some emission originates on intermediate scales.

2344+514 (Figure 4.9) – This is one of the most puzzling sources in the sample. It looks like a double when observed in C configuration, with faint, extended emission connecting the two compact components. A third, misaligned, less bright component could be a background object (even if it seems aligned with a small extension in the faintest component of the double). Both components are found within 200" (180 kpc) from the position of the optical and radio core. The A array observation resolves the faint emission, detecting a core-halo morphology, while the eastern feature appears extended in the direction of the core, as also shown by Rector et al. (2003). This elongation and the diffuse radio bridge connecting it to the core

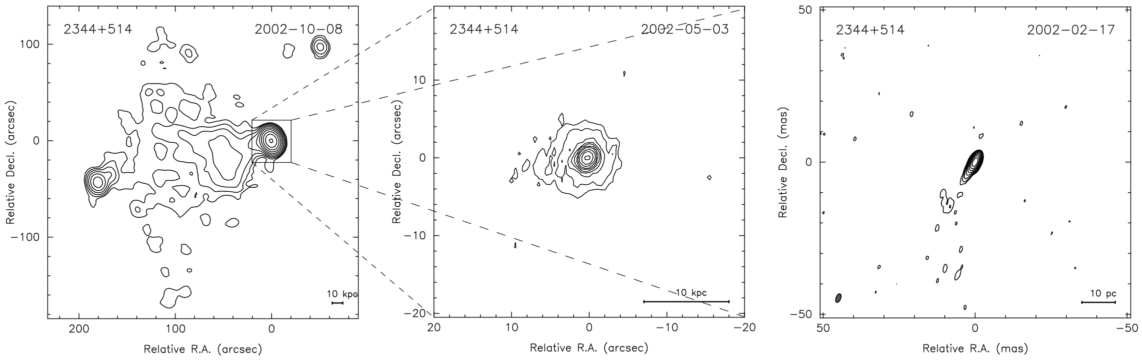

Figure 4.9 Images of 2344+514. From left to right: VLA at 1.4 GHz, C configuration; VLA at 1.4 GHz, A configuration; VLBA at 5 GHz.

indicates that the component is related to the source. On the contrary, the NW component does not show any radio structure suggesting a connection. Finally, the VLBA image shows a $\sim$ 20 mas jet oriented at 142° (see also Rector et al., 2003), confirming the complexity of this source (ΔPA $\sim$ 45° to the VLA main axis). Note that *Chandra* observations have revealed diffuse X-ray emission in the environment of this source (Donato et al., 2003).

2356−309 – Two components separated by 36" are connected by a weaker "bridge", resolved by the VLA in A configuration. A third component is found on the opposite side. The core is barely detected on the parsec scale, due to the low declination (−30°) and flux density (21 mJy) of this BL Lac. Because of the presence of a core, a radio bridge, and two possibly related compact structures, this source is similar to 2344+514.

Chapter 5

Low redshift BL Lacs: intrinsic properties

According to the current view of the unification of AGNs, BL Lac objects are expected to be FR I radio galaxies oriented at a small angle with respect to the line-of-sight. Moreover, radio data (see e.g. Giovannini et al., 2001) as well as variability, superluminal motion and high frequency emission (X- and γ- rays) strongly support the existence of highly relativistic jets. In agreement with the presence of fast jets and small angles to the line of sight, BL Lacs are usually core-dominated objects. At a first sight, the low redshift BL Lacs analysed in the previous chapters are in general agreement with this scenario. In the following sections, we will discuss in detail the properties of the sample that are most relevant in the context of the unified model.

5.1 Core and total radio power

The BL Lacs of the present low redshift sample are strongly core dominated objects. Although we found 10/30 objects where the core flux density is $< 50\%$ the total flux density (at 1.4 GHz), it is in general true that the core is the strongest component in the source. Beaming effects at the base of the jet are likely responsible of the enhanced *observed* radio power of the core; by comparing this value to the one expected from the total power at low frequency via the correlation found by Giovannini et al. (1988, 2001), we can derive the amount of boosting (Sect. 2.2). We need to account for variability, and we do this allowing for a variation of a factor 2 in the core flux density. In turn, this results in a range of possible Doppler factors for each source. Considering these intervals, we estimate for each object the allowed orientation angle under the assumption of a Lorentz factor $\Gamma = 5$. We note that smaller Lorentz factors (in particular $\Gamma < 3$) seem unlikely, according to Giovannini et al. (2001) and from strong and widely accepted lines of evidence (superluminal motions, rapid variability, high observed brightness temperatures, detection of γ-ray emission); on the other hand, larger Lorentz factors do not change significantly the permitted angles, as illustrated in the right panel of Fig. 5.1. In the left panel, we plot the core vs. total power for the objects in the sample, together with the literature correlation (Giovannini et al., 2001). As can be seen, all the objects have core luminosities far greater than expected from the correlation. In the right panel, each curve represents the set of (θ, β) that correspond to intrinsic values needed to fit the correlation for a given object. The dashed line corresponds to the assumption of $\Gamma = 5$ that we used to estimate the viewing angle; see however Sect. 5.3 for a more released approach.

There is one object whose behaviour is suspicious, i.e. 0145+138. The required angle is larger than 40°, and the resulting Doppler factor is $\delta_5 < 1$. This is absolutely uncommon for a BL Lac; as a matter of fact, the inspection of the original optical HST data reveals that this objects does not possess a compact core (Scarpa et al., 2000). Although the featureless optical spectrum is typical of a BL Lac (Perlman et al., 1996), the uncertainty in the X-ray *Einstein* position and the non detection in the RASS suggest that the identification of this objects is dubious.

5.2 Other observational constraints

Under the standard assumption that jets are intrinsically symmetric, we can derive constraints on the jet velocity and orientation. The approaching jet is amplified by relativistic beaming and the counter-jet is de-boosted. The observed ratio R between the observed jet and counter-jet brightness is related to the intrinsic jet velocity β and orientation angle θ by $R = \left(\dfrac{1+\beta\cos\theta}{1-\beta\cos\theta}\right)^p$, where $p = 2+\alpha$ (continuous jet) or $p = 3+\alpha$ (moving sphere). Here we assume a continuous jet, with spectral index $\alpha = 0.5$ ($S(\nu) \propto \nu^{-\alpha}$).

However, in BL Lacs the counter-jet is generally de-boosted below the detection threshold on the parsec scale and we can only determine lower limits $R_{\rm min}$. Furthermore, since our sample is dominated by faint objects, the main jet shows in most cases a low brightness emission resulting in small $R_{\rm min}$. Therefore, in most

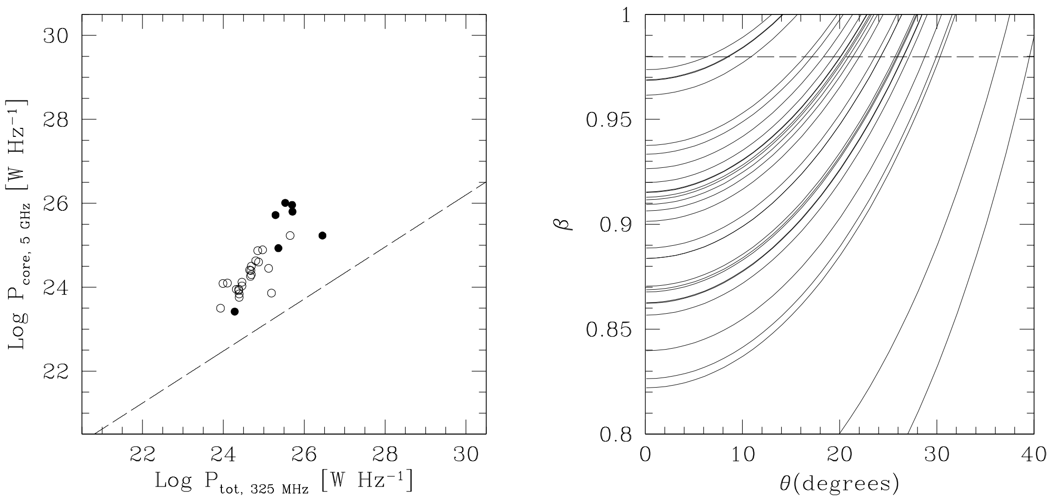

Figure 5.1 Left: $P_{\rm tot}/P_{\rm core}$ diagram for the sources in the sample. Empty circles represent HBL, filled circles are for LBL. The dashed line is the correlation found by Giovannini et al. (2001). Right: values of θ and β needed to fit the correlation for each object; dashed line: $\beta = 0.98$, i.e. $\Gamma = 5$

Table 5.1. Limits from the Synchrotron Self Compton model

Name	$\delta_{\rm min}$	$\Gamma_{\rm min}$	$\theta_{\rm max}$ (°)
0521−365	2.2	1.3	27
0829+046	4.6	2.4	13
1101+384	2.4	1.4	25
1215+303	2.6	1.5	22
1418+546	2.2	1.3	26
1514−241	9.3	4.7	6
1652+398	2.5	1.4	24
1807+698	5.3	2.7	11
2200+420	6.7	3.4	9
2201+044	1.1	1.1	65
2254+074	4.0	2.1	15

Note. — Col. 2: Minimum Doppler factor from SSC (we only report sources where $\delta_{\rm min} > 1$). Col. 3: Minimum Lorentz factor Γ. Col. 4: Largest possible orientation angle.

cases we do not find significant constraints on β and θ; only in 6 objects the J/CJ ratio is $R_{\min} > 100$. In these cases, we give the relative limits on $\beta\cos\theta$ in Table 4.6 (Col. 10).

The Synchrotron Self-Compton model (SSC, Ghisellini et al., 1993) poses a third observational constraint on the Doppler factor, by requiring that the X-ray flux produced by Inverse Compton does not exceed the observed one. Thanks to the availability of a large number of observations carried out by X-ray satellites (ASCA, EXOSAT, BeppoSAX, ROSAT, and Einstein), Donato et al. (2001) have collected fluxes at 1 keV for all the objects in the sample. The standard formula yields the Doppler factor as an inverse power of the VLBI core angular dimension θ (in milliarcsecond, see Sect. 2.2 for an explanation of the other quantities):

$$\delta = f(\alpha) F_M \left[\frac{\ln(\nu_b/\nu_m)}{F_X\, \theta^{6+4\alpha}\, \nu_X^{\alpha}\, \nu_m^{5+3\alpha}} \right]^{1/(4+2\alpha)} (1+z) \tag{5.1}$$

Since VLBI cores are unresolved in our data, we find lower limits on δ. There are 20 sources where the result is not informative ($\delta_{\min} < 1$); however, for 10 sources we have mild limits on δ, as reported in Table 5.1. These limits provide useful constraints on the minimum velocity and the maximum angle allowed. Basically, these values are in good agreement with those required from the core enhancement argument; given the independence of the two estimates, this strengthens the conclusion that small to moderate angles to the line-of-sight and high velocity jets are characteristic of the objects in the sample.

In Fig. 5.2, we illustrate the resulting allowed angles, as derived from the combination of all the constraints. The results are consistent with the expectations of the unified scheme, since most of our low-z BL Lacs require a small to moderate angle to the line of sight. In Table 5.2, we present the resulting best available estimates from the previous studies of the allowed jet orientation angle θ and the relative Doppler factor δ in the case $\Gamma = 5$. We note that there is a tendency for LBL to be oriented at smaller angles ($\langle\theta\rangle_{\rm LBL} = 14^\circ \pm 12^\circ$) than HBL ($\langle\theta\rangle_{\rm HBL} = 25^\circ \pm 9^\circ$). However, there are large uncertainties, which can result both from the small number of objects considered but also to a likely large scatter in the distribution of intrinsic angles. We also note that the adoption of a single Lorentz factor can be partly responsible for this result. Therefore, in the next section we explore a more released approach.

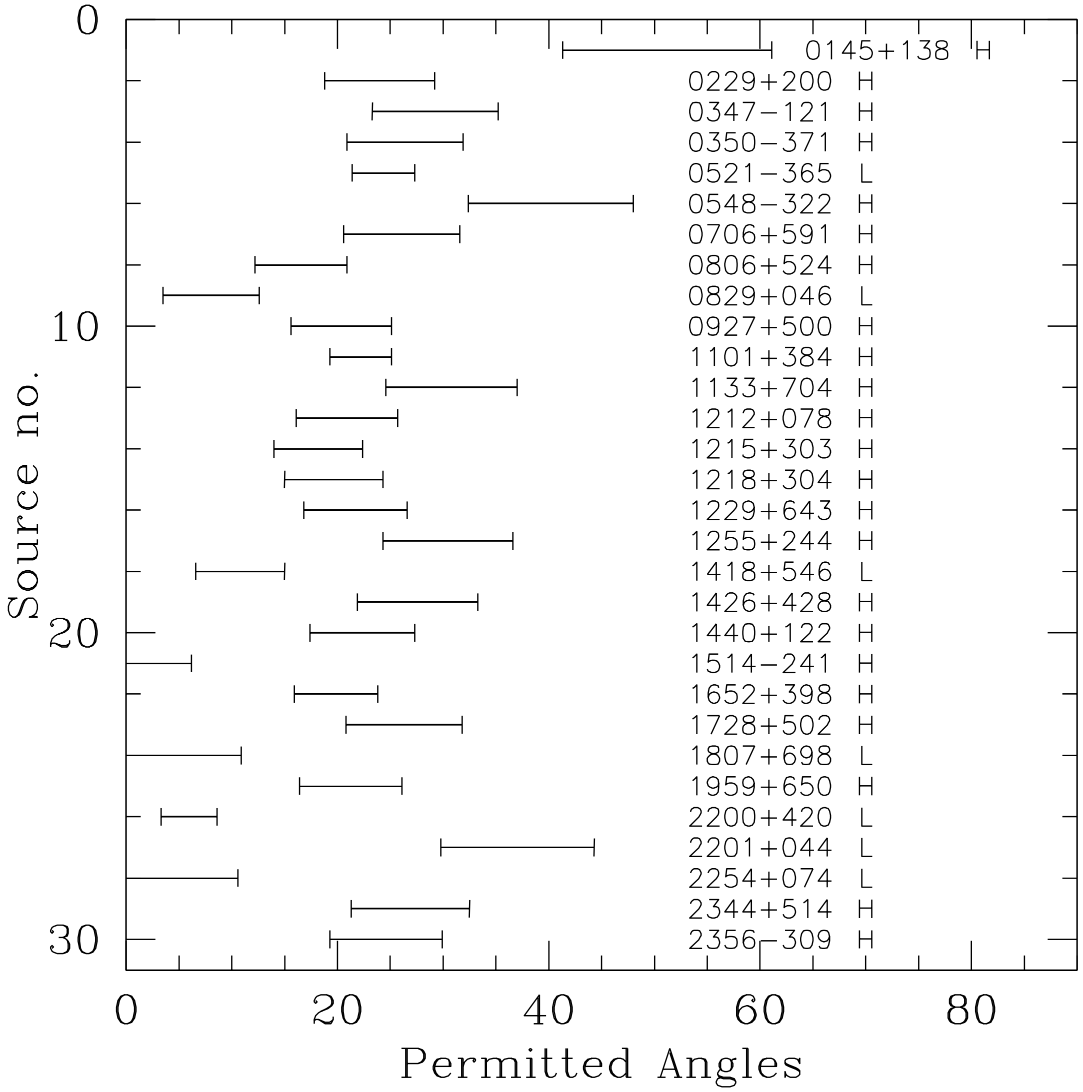

Figure 5.2 Allowed angles to the line-of-sight, assuming $\Gamma = 5$, from core dominance, jet/counterjet ratio, ans SSC model. The letter beside the name refers to the type of source (H: high frequency peaked BL Lac; L: low frequency peaked BL Lac). Note the high values required for 0145+138 (see section 5.1).

Table 5.2. Sample intrinsic parameters with $\Gamma = 5$

Num.	Name	Log$P_{\rm t}$ W Hz^{-1}	$\Delta\theta_5$ (°)	$\Delta\delta_5$	$\Delta P_{\rm c,i}$ W Hz^{-1}
1	0145+138	24.17	41 – 61	0.4 – 0.8	23.10 – 23.70
2	0229+200	24.69	19 – 29	1.4 – 2.8	23.42 – 24.02
3	0347−121	24.39	23 – 35	1.0 – 2.0	23.24 – 23.84
4	0350−371	24.46	21 – 32	1.2 – 2.4	23.28 – 23.88
5	0521−365	26.45	21 – 27	1.5 – 2.3	24.51 – 24.86
6	0548−322	25.19	32 – 48	0.6 – 1.2	23.73 – 24.33
7	0706+591	25.12	21 – 32	1.2 – 2.4	23.69 – 24.29
8	0806+524	24.85	12 – 21	2.4 – 4.7	23.52 – 24.12
9	0829+046	25.70	3 – 13	4.6 – 9.1	24.05 – 24.65
10	0927+500	23.99	16 – 25	1.8 – 3.6	22.99 – 23.59
11	1101+384	24.46	19 – 25	1.8 – 2.7	23.28 – 23.63
12	1133+704	24.39	25 – 37	0.9 – 1.8	23.23 – 23.83
13	1212+078	24.87	16 – 26	1.7 – 3.4	23.53 – 24.13
14	1215+303	25.65	14 – 22	2.1 – 4.0	24.02 – 24.57
15	1218+304	24.80	15 – 24	1.9 – 3.7	23.49 – 24.09
16	1229+643	24.65	17 – 27	1.6 – 3.2	23.40 – 24.00
17	1255+244	23.93	24 – 37	0.9 – 1.9	22.95 – 23.55
18	1418+546	25.71	7 – 15	3.7 – 7.5	24.05 – 24.65
19	1426+428	24.38	22 – 33	1.1 – 2.2	23.23 – 23.83
20	1440+122	24.68	17 – 27	1.5 – 3.1	23.42 – 24.02
21	1514−241	24.97	0 – 6	7.7 – 9.9	22.90 – 23.11
22	1652+398	24.69	16 – 24	1.9 – 3.5	23.42 – 23.93
23	1728+502	24.32	21 – 32	1.2 – 2.4	23.19 – 23.79
24	1807+698	25.36	0 – 11	5.3 – 9.9	22.94 – 23.48
25	1959+650	24.10	16 – 26	1.7 – 3.3	23.06 – 23.66

Table 5.2 (cont'd)

Num.	Name	Log$P_{\rm t}$ W Hz^{-1}	$\Delta\theta_5$ (°)	$\Delta\delta_5$	$\Delta P_{\rm c,i}$ W Hz^{-1}
26	2200+420	25.29	3 – 9	6.4 – 9.2	23.80 – 24.11
27	2201+044	24.28	30 – 44	0.7 – 1.3	23.17 – 23.77
28	2254+074	25.53	0 – 11	5.4 – 9.9	24.02 – 24.54
29	2344+514	24.38	21 – 32	1.2 – 2.3	23.23 – 23.83
30	2356−309	24.67	19 – 30	1.3 – 2.7	23.41 – 24.01

Note. — Col. 3: Logarithm of total radio power at 325 MHz. Col. 4: range of possible jet orientation angle. Col. 5: Doppler factor range. Col. 6: Logarithm of intrinsic core radio power at 5 GHz. Values are derived from core dominance, jet/counter-jet ratio, and SSC model. The range of allowed angles accounts for possible core variability, as well as for the intrinsic scatter in the $P_{\rm core}/P_{\rm tot}$ correlation.

5.3 Varying Lorentz factors

In the above sections, we have assumed that all the sources have, on kpc scale, the same Lorentz factor $\Gamma = 5$. Although in Sect. 5.1 we argued that this is a quite good approximation of the real situation, we want to explore another approach, less restrictive than assuming a constant velocity for all the jets. In particular, we will make use of the relation $\Gamma \sim 1/\sin\theta$, which corresponds to the maximum angle allowed for a given Doppler factor. In a statistical sense, this will be the most likely situation. We still make use of the Pcore/Ptot relation, in order to uniquely determine the values of β and θ. We show in Fig. 5.3 the resulting behaviour in the (θ, β) plane, and in figure 5.4 the histogram of the angles and Lorentz factor distribution. The average angle for the sample is $\langle\theta\rangle = 18° \pm 5°$, without showing any relevant difference between LBL and HBL ($\langle\theta_{\rm LBL}\rangle = 15° \pm 7°$ and $\langle\theta_{\rm HBL}\rangle = 20° \pm 4°$, respectively). There are still four LBL that need to be oriented at rather small angles ($\theta < 15°$), namely 0829+046 ($z = 0.180$), 1418+546 ($z = 0.152$), 2200+420 ($z = 0.070$), and 2254+074 ($z = 0.190$); however, their redshift is typically larger than the average, so they may be more extreme and peculiar objects.

The distribution of Lorentz factors (Fig. 5.4 right panel) is interesting. The majority of objects, including all HBL, is distributed around $\Gamma = 3$. There are however four objects separated from the others, which have $\Gamma > 5$. These objects are the four LBL

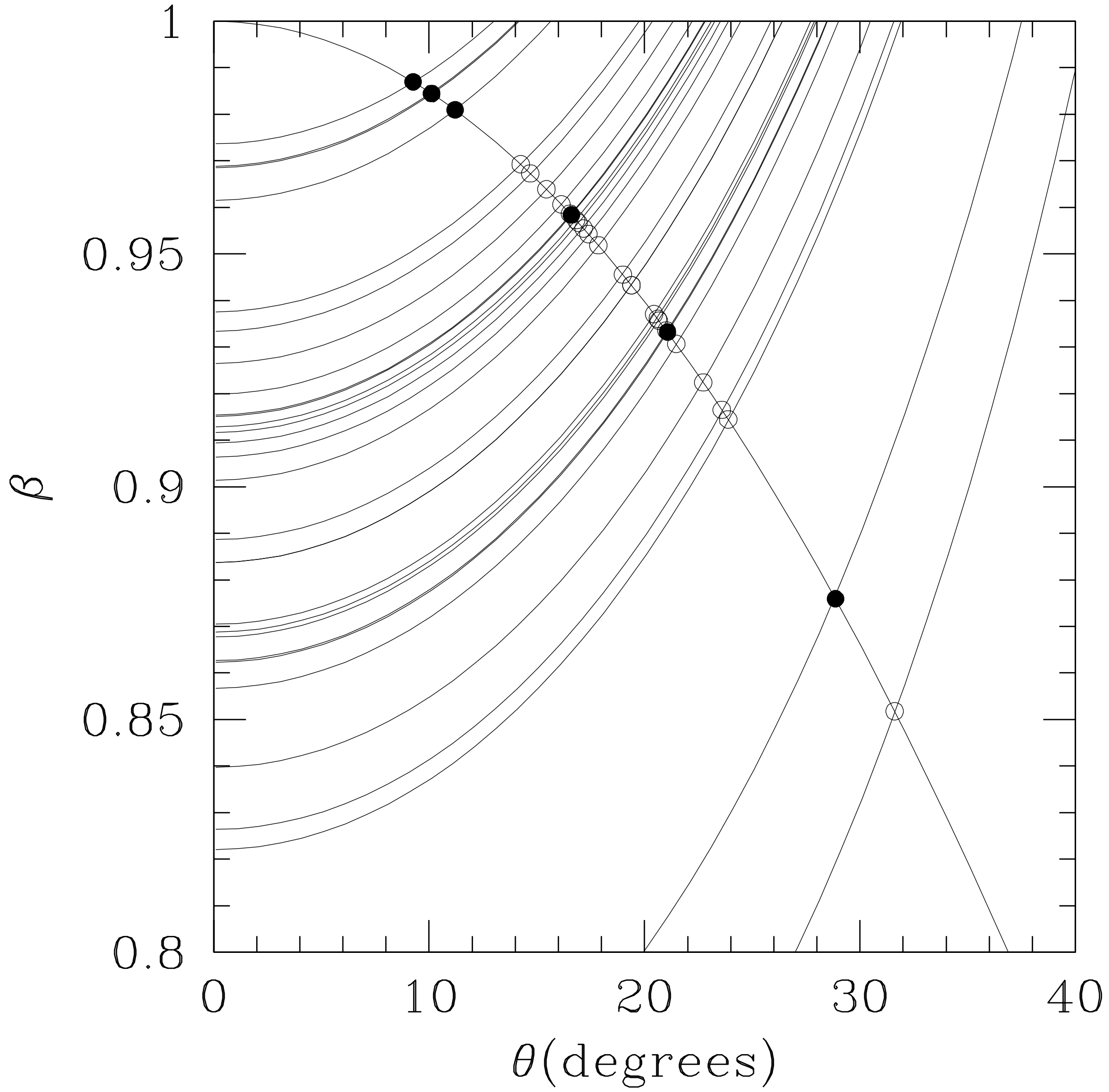

Figure 5.3 Filled symbols denote LBL and empty symbols HBL.

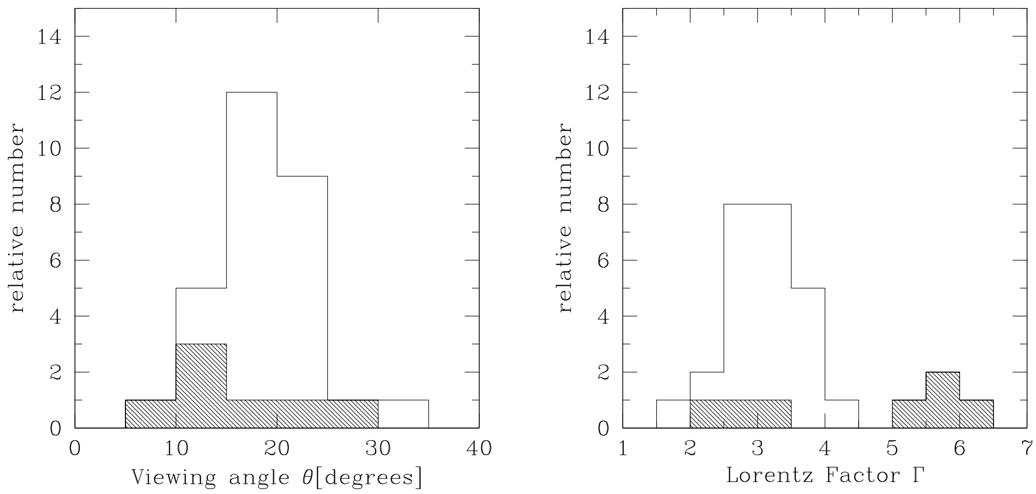

Figure 5.4 Distribution of the resulting viewing angle θ (left) and Lorentz factor Γ (right); the shaded parts correspond to LBL only.

mentioned above. Thus, it seems that, on the VLA scale, the bulk velocity of jets is larger in LBL than in HBL. This is somehow puzzling, since constraints on other scales, and from other arguments (e.g. TeV $\gamma-$ray emission), require the opposite. However, we note that, on parsec scale, the study of proper motion have revealed superluminal components in EGRET sources (Jorstad et al., 2001) and subluminal or absent motion in TeV sources (Tingay & Edwards, 2002; Piner & Edwards, 2004). Thus, it is interesting to speculate that the emission of TeV taking place on even smaller scales may be responsible for energetic losses resulting in slower jets on radio scale.

5.4 Comparisons and parent population

The objects requiring the largest beaming factors are the most distant and powerful in the sample. Since samples of distant objects and with large flux limits (e.g. the 1 Jy) have been studied in detail, it is interesting to compare some properties of the two populations. The value of the core dominance parameter $R = \frac{S_{\rm core}}{S_{\rm ext}}$ in our sample is $\langle R \rangle = 3.2$. Actually, we excluded the three sources (1418+546, 1514−241, and 2254+074) in which the flux density of the core is larger than the total; this behaviour has to be ascribed to variability, and reminds us that the whole result needs to be considered with caution. However, this is true also for other samples and we do not expect it to affect the average properties of the sources in our sample.

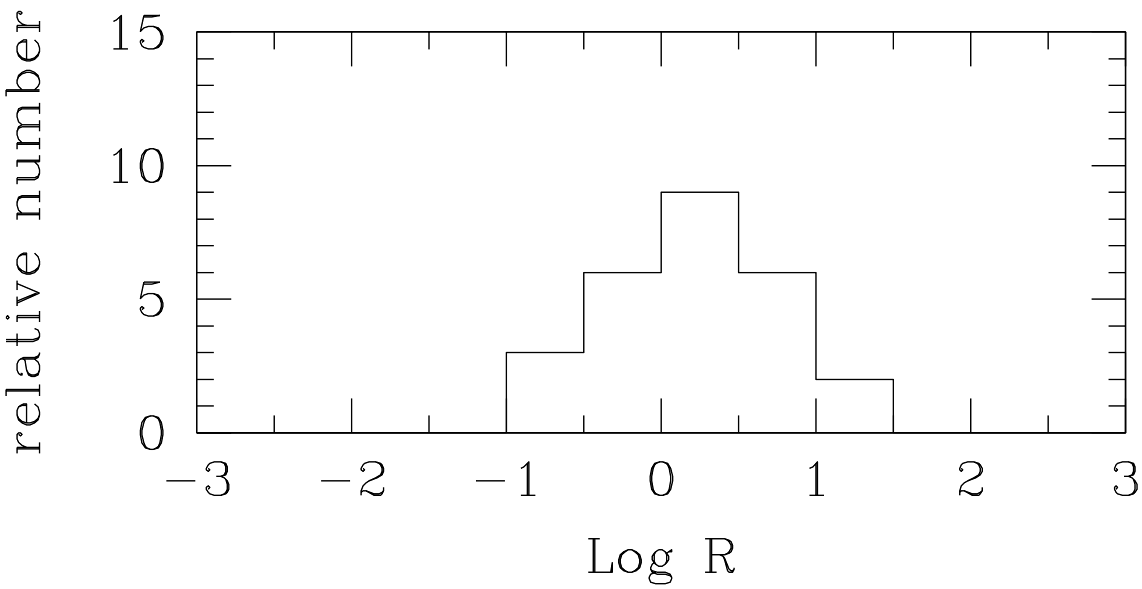

Figure 5.5 Distribution of the core dominance factor R for sources in the present sample.

The present low redshift BL Lac sample is the less core-dominated among the EMSS and the 1 Jy; in the EMSS $\langle R \rangle \geq 4.2$ (Rector et al., 2000) and much larger values are observed in the bright 1 Jy BL Lacs (Rector & Stocke, 2001).

It is also interesting to discuss the difference in orientation with respect to more powerful objects, by considering the amount of bending in the jets. In particular, large bending is suggestive of small angles, while straight jets are more common in the presence of a larger angles between the jet axis and the line-of-sight. In Fig. 5.6 we present the bending angle distribution in the 1 Jy sample from Cassaro et al. (2002) and for sources in our sample, excluding those belonging to the 1 Jy sample. The histogram provides a comparison of the two populations, which indicates that high power BL Lacs show larger distortions than weak ones. The significance of the difference between the two distributions is quite strong (Kolmogorov-Smirnov of 1.42, with a probability that the two distribution are intrinsically similar of $\lesssim 3\%$). It is tempting to speculate that this may be ascribed to a different jet orientation, with smaller viewing angles for more powerful and twisting sources. However, it is also possible to give a different interpretation for this occurrence of large bending, if we speculate that FR II have intrinsically more bent jets than FR I and that the 1 Jy sample has a parent population in which FR IIs are a significant fraction.

On the contrary, FR I radio galaxies are the best candidate to be the parent population of objects in the present sample. From our estimate of the jet velocity

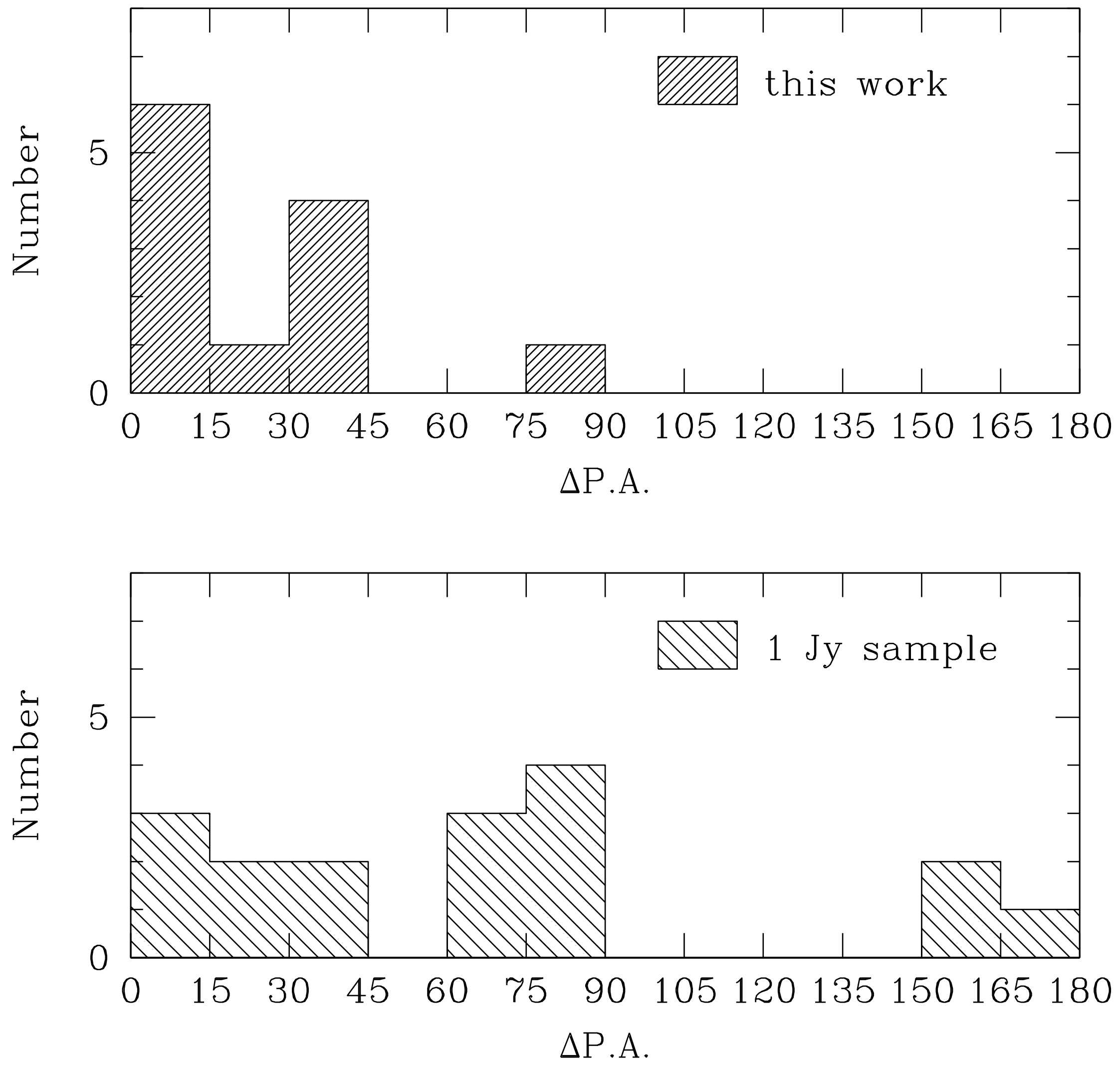

Figure 5.6 Distribution of bending for sources in the present sample (top) and in the 1 Jy sample (bottom, data from Cassaro et al., 2002). We have excluded from our sample objects belonging to the 1 Jy sample.

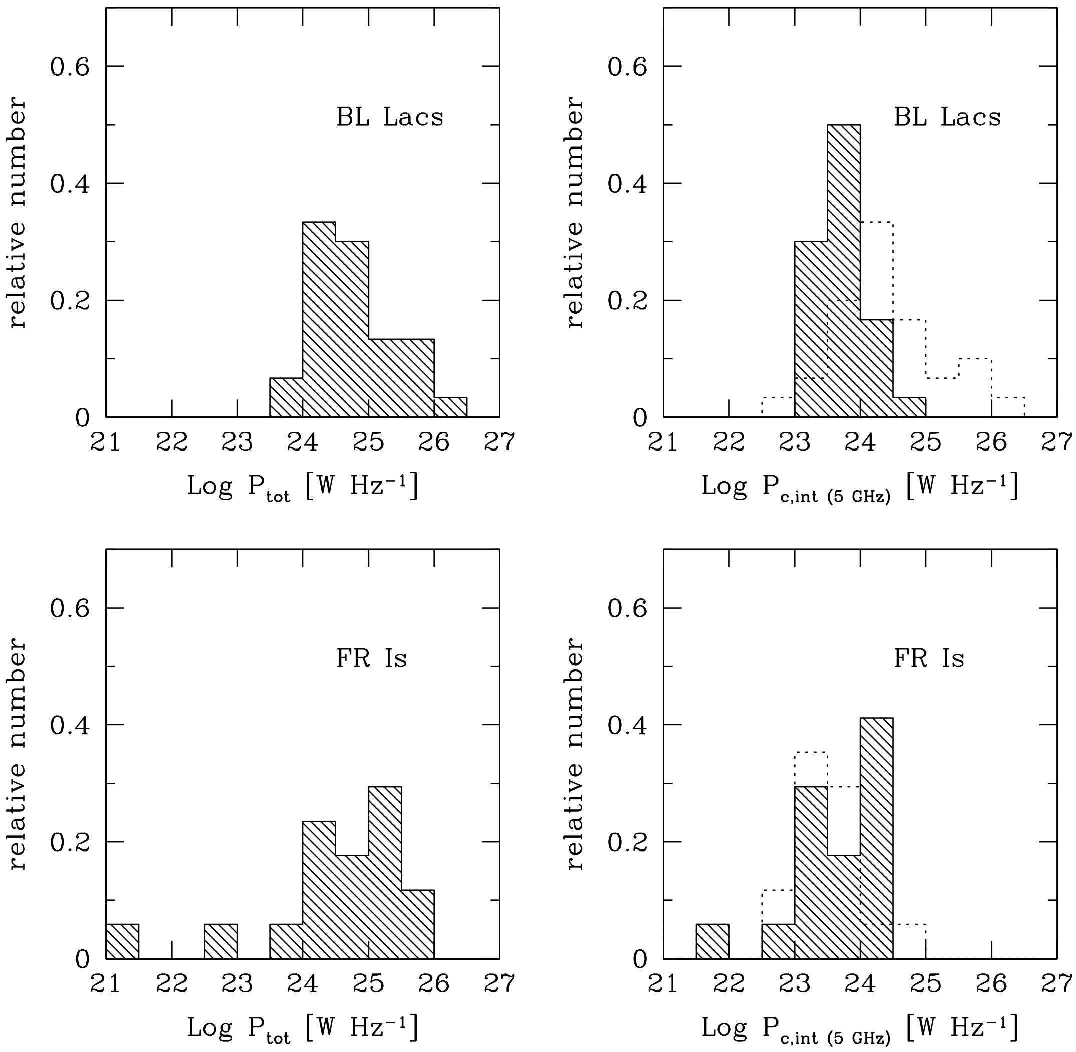

Figure 5.7 Distribution of total (325 MHz) and intrinsic core power (at 5 GHz) for objects in the present sample and for FRI and LPC radio galaxies in a sample of radio galaxies (Giovannini et al., 2001). The dashed histograms overlaid to the intrinsic core power show the distribution of the observed values.

and orientation, we can derive the intrinsic core radio power: $P_{\rm c,i} = P_{\rm c,o} \times \delta^{-(2+\alpha)}$. In Fig. 5.7 we present the distribution of the core and low frequency total radio power for the present sample and the sample of FR I and low power compact radio galaxies studied by Giovannini et al. (2001). The two samples cover the same range in low frequency total radio power (Fig. 8, left), as expected if FR Is are the parent population of BL Lacs. We note that the total radio power at 325 MHz should be an intrinsic source property since the core is self-absorbed and extended lobe emission dominates at low frequency. In the right panels, the shaded histograms represent the intrinsic core radio power distribution, while the overlaid dashed histograms refer to the observed power of the radio core. Despite a significant difference in the observed values, the distribution of the intrinsic core radio power is similar and in the same range, confirming that the intrinsic properties of the two populations are the same.
Therefore, we conclude that in our sample the parent population is composed of FR I radio galaxies alone and that the fraction of FR IIs in the parent population of BL Lacs must be very small, if any. FR IIs that may be present in the 1 Jy sample must therefore be ascribed to the very large volume considered. In any case, their incidence may not be negligible only among the most powerful LBL, which could therefore have different properties.

5.4.1 Radio/Optical

Multi-wavelength data provide a tool to investigate the mechanisms involved in the nuclear activity. For the present sample, a wealth of information is available thanks to the optical observations performed with the Hubble Space Telescope. In particular, for all the objects it has been possible to separate the contribution of a central compact core and of the host galaxy. Both quantities have significant impact on our understanding of the BL Lac phenomenon. The central compact core is a clear signature of the nuclear activity; the host galaxy luminosity is a tool to estimate the mass of the central black hole, via the well known correlation studied by Magorrian et al. (1998), Kormendy & Gebhardt (2001), Bettoni et al. (2003).
Alternatively, one could estimate the black hole mass using the relation between the central stellar velocity dispersion σ (Ferrarese & Merritt, 2000; Gebhardt et al., 2000). However, direct measurement of such quantity in BL Lacs are difficult to obtain and are becoming available only for a small number of objects, not

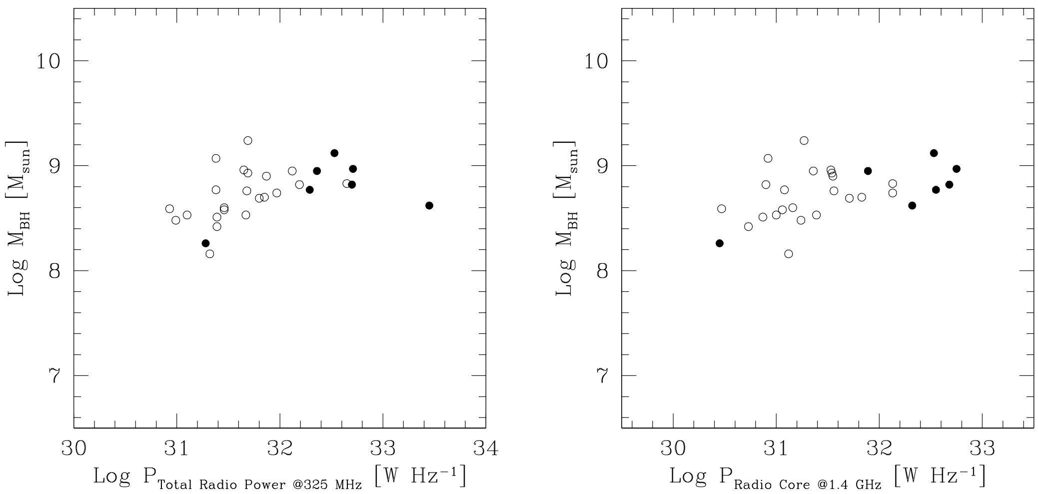

Figure 5.8 Black hole mass vs. total (left panel) and core (right panel) radio power. Filled and empty symbols represent HBL and LBL respectively.

without some controversy (Falomo et al., 2003; Barth, Ho, & Sargent, 2003; Falomo, Kotilainen, & Treves, 2002); indirect estimates of σ via the fundamental plane are also affected by difficulties in determining the other observables in the FP (the effective surface brightness μ_e and the effective radius R_E) as well as the intrinsic scatter of FP relation.

Therefore we adopt black hole mass estimates based on the host galaxies bulge luminosity, as given in Falomo, Carangelo, & Treves (2003). We show in Fig. 5.8 the plot of black hole mass vs. radio power. Neither the total nor the core radio power seem to be good indicator of the black hole mass. In both cases, there is a weak trend of larger $M_{\rm BH}$ for more powerful radio sources but the correlation coefficient is low (r = 0.45 and 0.47, respectively). Furthermore, we note that both radio power and black hole mass (estimated with host luminosity) include a dependence on redshift, which also contributes to the observed trend. We therefore conclude that black hole mass is not a critical parameter for the emitted radio power in nearby BL Lacs.

This is confirmed also if we consider black hole estimates as derived by Wu, Liu, & Zhang (2002). Using their data we do not find any signature of even a weak correlation ($r < 0.1$), which, as a matter of fact, strengthens our conclusion.

Chiaberge, Capetti, & Celotti (1999) have exploited Hubble Space Telescope and radio data to discuss the physical properties of nuclei of radio galaxies, finding

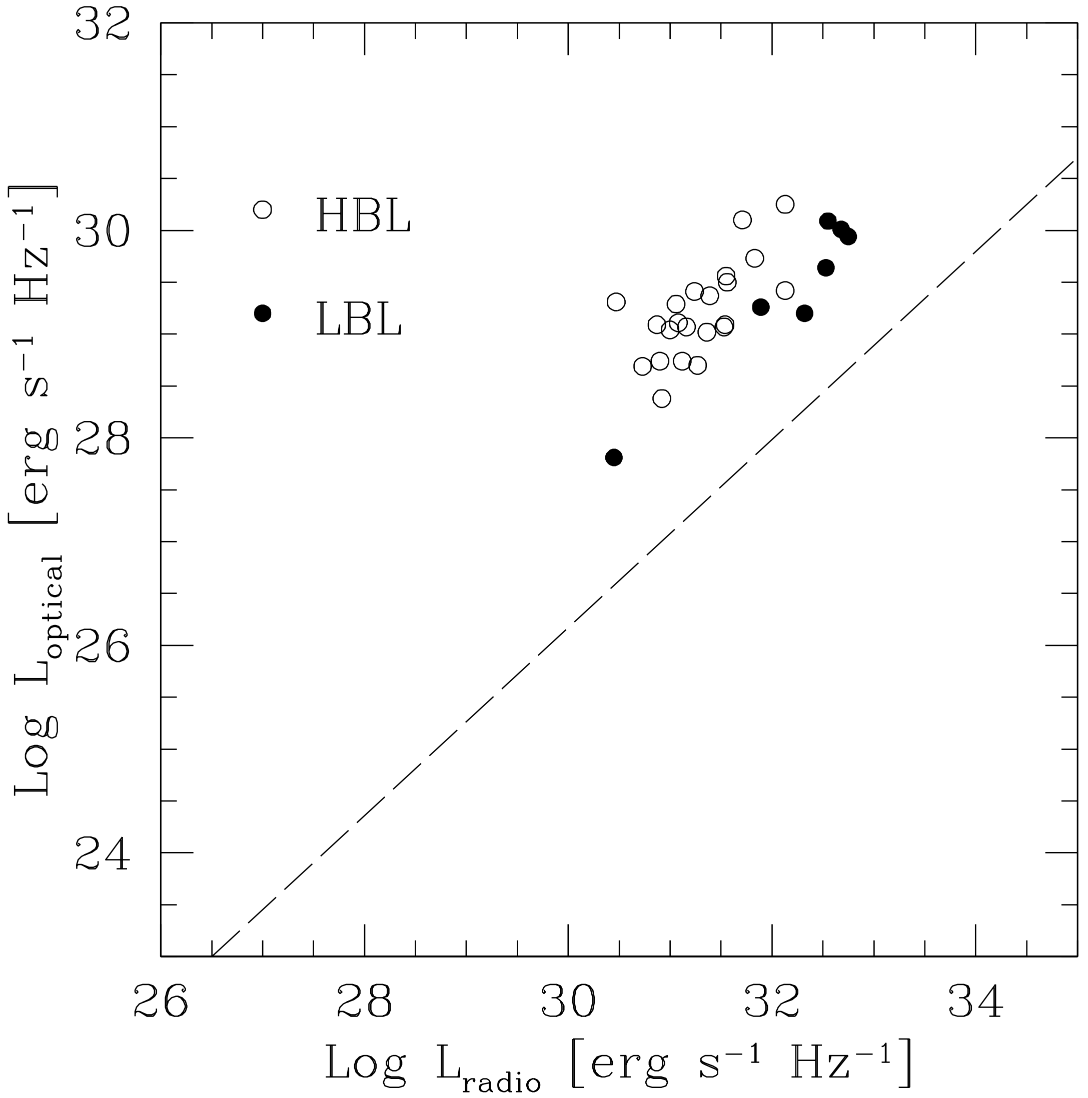

Figure 5.9 Optical vs radio core power diagram for BL Lacs in the present sample; empty symbols are HBL, filled symbols are LBL. The dashed line shows the radio-optical correlation for cores of FR I radio galaxies (Chiaberge, Capetti, & Celotti, 1999).

a linear correlation between optical and radio luminosity. This correlation is interpreted in terms of a common non thermal origin. Our high quality radio data and the optical HST results (Urry et al., 2000; Falomo et al., 2000) allow us to perform the same study on the sources of our low redshift sample of BL Lacs. We present in fig. 5.9 the comparison between optical and radio core luminosity for BL Lacs, together with the correlation found by Chiaberge, Capetti, & Celotti (1999) for FR I nuclei.

The objects in the present sample span almost three orders of magnitude in radio core luminosity (at 1.4 GHz) and the optical core luminosity increases linearly with it over this interval. As in FR I radio galaxies, the emission in the two wavebands is ascribed to the same non thermal process, with negligible contribution from, e.g., a thermal disk. However, the optical cores of BL Lacs are about two magnitudes brighter than those of FR I galaxies with the same core radio luminosity. Notice that we are plotting *observed* values, i.e. quantities that are affected by beaming. While it is interesting to note that this keeps the correlation tight, we argue that this may be responsible for the optical offset observed for BL Lacs. Chiaberge et al. (2000) obtained a similar result from the BL Lacs in the Slew survey, while the LBL of the 1 Jy sample result less displaced from the correlation than our objects. They put forward an explanation based on de-beaming trails for the broadband SED and conclude that a single emitting region can not account for this observational behaviour. Interestingly, a two velocity jet (fast spine and slower external layer) is a plausible solution that accounts also for other observational properties, such as limb brightening of jets (see Chapter 6).

5.4.2 Ledlow & Owen diagram

The Ledlow & Owen diagram (Ledlow & Owen, 1996) is a diagram in which the optical magnitude of the host galaxy is plotted on the x-axis and the radio power on the y-axis. When one fills this diagram with FR I and FR II radio galaxies, they belong in different regions. At a given optical magnitude, FR IIs are situated above a certain value of total radio power; however, this value is not fixed and it is larger for larger optical luminosities. As discussed above (Sect. 5.4.1), there is a relation (e.g. McLure & Dunlop, 2002) between optical magnitude of the host in R-band and BH mass; similarly, Willott et al. (1999) have discussed the relationship between radio power and total jet kinetic power. Thus, we can reword the previous sentence as: for a given BH mass, FR IIs have jets of total power above a certain value and this value is larger for more massive black holes. That is to say, there is a critical ratio between jet power and black hole mass that divides FR I and FR II radio galaxies.

Similarly, we can translate the total radio power into accreting power; in fact, the total radio power is related to the narrow emission line luminosity (Willott et al., 1999), which is directly produced by photoionization from the nuclear accreting

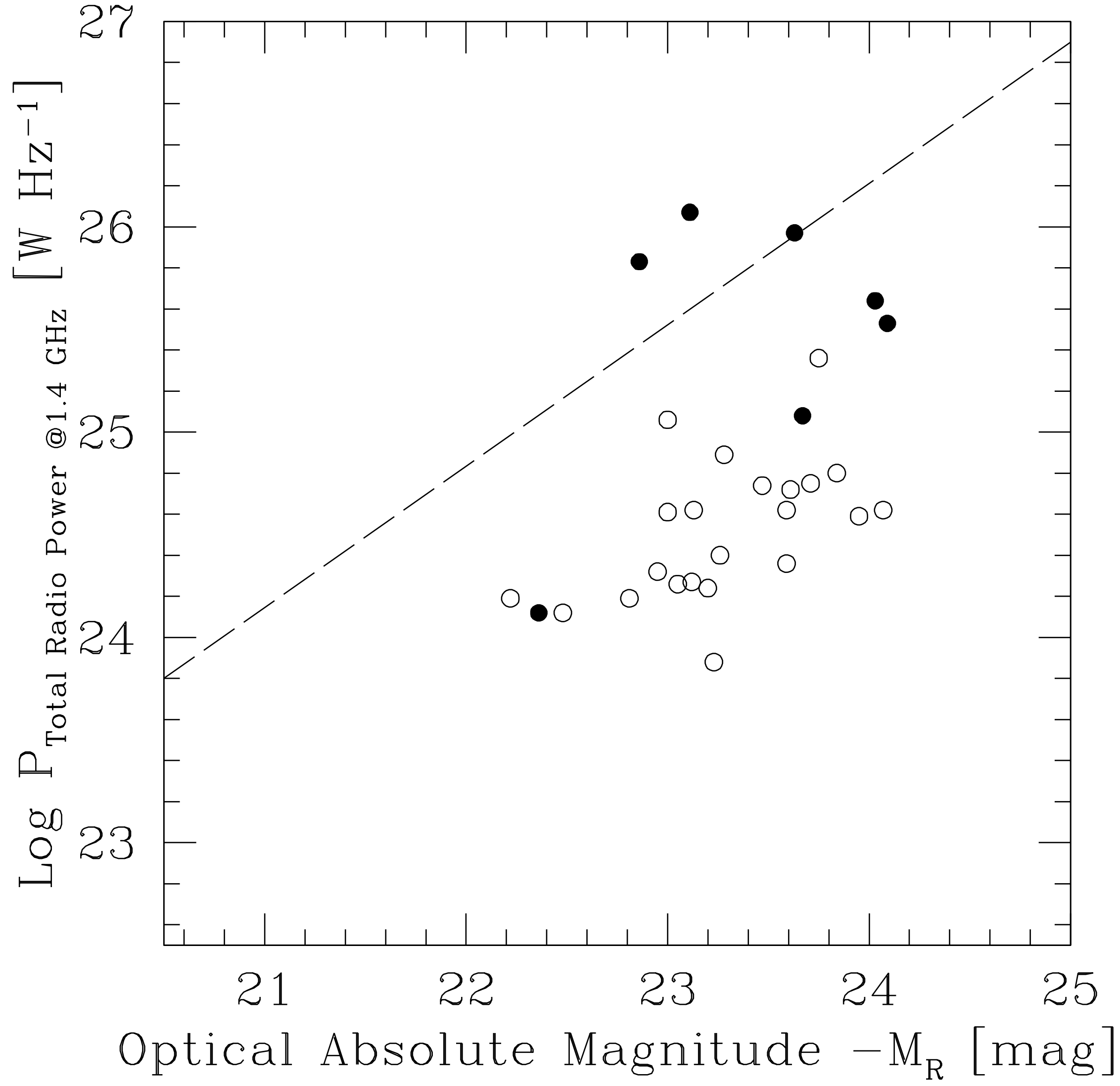

Figure 5.10 Ledlow & Owen diagram; the quantities on the x and y axis (host magnitude and total radio power) are a measure of the black hole mass and accretion rate, respectively. The dashed line corresponds to $L_{\rm jet} \sim 0.015 L_{\rm Edd}$ (Ghisellini & Celotti, 2001). The three objects above the line are 0521−365, 0829+046, 2200+420. Filled and empty circles represent LBL and HBL, respectively.

radiation. Therefore, the radio power is a measure of the accretion luminosity and the division between FR I and FR II can be attributed to a critical ratio between accretion luminosity and black hole mass. This is extremely useful for our case, since line luminosity is generally not available for sources in our sample.

Figure 5.10 shows the distribution of objects belonging to the present sample in the Ledlow & Owen diagram. The dashed line roughly corresponds to the division between FR I and FR II (see below). All the HBL are situated below this line, i.e. in the FR I region. Two LBL (0521−365 and 0829+046) lie above the dashed line, and 2200+420 intercepts it. However, if we consider the de-beamed intrinsic radio power, they all move below the line, where FR I are placed, yielding another proof that low power radio galaxies are the parent population of our BL Lacs.

Furthermore, the relationship between host magnitude and black hole mass and the one between radio power and accretion luminosity make this plane even more interesting. The accretion process may take place in low power sources through optically thin ADAF (advection dominated accretion flows), which are hot and radiatively inefficient. The accreting material releases gravitational energy, which is not radiated to the observer but is carried into the black hole. However, this process has a theoretical upper limit on the accretion rate (Narayan & Yi, 1995), above which the ADAF can not be maintained and becomes an optically thick accretion disk (which has no such upper limit). The critic upper limit to the accretion rate for an ADAF is $\dot{m}_{\rm crit} = \dot{M}_{\rm crit}/\dot{M}_{\rm Edd}$. Ghisellini & Celotti (2001) have estimated the accretion rate for radio galaxies and proposed that FR Is and FR IIs have $\dot{m}$ below and above $10^{-2} - 10^{-3}$, respectively; thus, some value in between could be the critical one and a different state for the central engine would be at the base of the difference between the two classes. BL Lacs in the present sample are all situated below this threshold; they are sub-Eddington systems with sub-critical accretion rates.

Chapter 6

Parsec Scale Properties of Markarian 501

In the previous chapters we have considered the global properties of a sample of BL Lacs, without paying much attention to each and every object. However, it has clearly emerged that some sources display properties that deserve a more careful analysis. For example, there are at least five sources strong enough to be detected at VHE (Very High Energy, $\gtrsim$ TeV); others display large bending between the parsec and kpc scale, a distorted morphology, or secondary compact components. In the present chapter, we discuss the results of a high angular resolution study of the BL Lac object Markarian 501 in the radio band.

6.1 Introduction

Along with summarising the peculiar properties of BL Lacs at all other wavelengths (lack of strong emission lines, high levels of variability, optical polarization up to 3%, detection at X-ray and γ-ray energies), we have discussed in the last chapter some of their rather extreme properties in the radio: the parsec-scale structure is dominated by a compact, flat-spectrum core, from which a one-sided jet emerges, showing knots of enhanced brightness. A few works (see, e.g., Homan et al., 2001; Jorstad et al., 2001) have also shown that, when monitored over long intervals, these components are often found to be in motion, sometimes with an apparently superluminal velocity.

Among the objects in our sample, Markarian 501 (B1652+39) possesses several properties that make it an ideal target to perform a more detailed study and test the assumptions involved in unified models. At its extremely low redshift

($z = 0.034$)[1], 1 mas = 0.72 pc; therefore, the milliarcsecond resolution achievable with VLBI techniques makes it possible to investigate in great detail the regions near the central core. Furthermore, Mkn 501 is one of the few sources where hints of limb-brightening in the jet have been found, both in total intensity (Giovannini, 1999) and in polarization (Aaron, 1999). Finally, this source is very well studied at other frequencies and it is known for its X$-$ and $\gamma-$ray activity, which also sets constraints on the parameters describing the physics of the inner jet (see Tavecchio et al., 2001; Katarzyński et al., 2001, and references therein). In particular, Markarian 501 has been the first non EGRET source to be detected at TeV energy (Quinn et al., 1996).

Therefore, we undertook an extensive multi-epoch, multi-frequency VLBI study of this source. We consider new observations as well as previously published data, in order to study the physical properties of this source. In particular, we will make use of data taken at 14 different epochs, ranging between 1.6 GHz and 22 GHz in frequency, and including new Space VLBI observations obtained on 2001 March 5 and 6 at 1.6 and 5 GHz. This large collection of data allows us to study the kinematics of the parsec-scale jet, looking for motion in components or signatures of limb brightening, possibly associated to velocity gradients. Accordingly, we will estimate the bulk velocity and orientation with respect to the line of sight, as well as some physical parameters of the parsec-scale jet. Additionally, our data-set allows us to compare images obtained at different frequencies with similar resolutions and thus to perform spectral index studies for comparison with the total intensity images. As in the rest of this thesis, we define the spectral index α such that $S(\nu) \propto \nu^{-\alpha}$.

6.2 Observations

Table 6.1 summarizes all observations considered in this paper, listing epoch, frequency, total observing time and array used. The notes provide references for details. The present data-set is similar to the one used by Edwards & Piner (2002) to discuss the proper motion in Mkn 501: we did not use the 1995 Oct 17 epoch (due to its low sensitivity), or the 1996 Jul 10 and 1998 Oct 30 epochs (as better data from other nearby epochs was available). On the other hand, we add 3 more epochs (see note 4 to Table 6.1) at 15 and 22 GHz and we consider two new Space

[1]Hereafter, we will assume $H_0 = 65\,\mathrm{km\,s^{-1}\,Mpc^{-1}}$

Table 6.1. Observation List

Date	Frequency (GHz)	Array	Observing Time (min)
1995 Apr 7[a]	15	VLBA	40
1995 Apr 12[b]	8.3	VLBA	15
1995 Dec 15[a]	15	VLBA	40
1996 Apr 23[b]	8.3	VLBA	7.5
1996 Apr 23	15	VLBA	6
1996 Jun 7[c]	8.1	VLBA	6
1997 Mar 13[a]	15	VLBA	40
1997 Apr 25[d]	15	VLBA	90
1997 Apr 25	22	VLBA	90
1997 May 26[d]	15	VLBA	50
1997 May 26	22	VLBA	50
1997 Aug 4	1.6	VLBA−SC+GO+**HALCA**	420
1997 Aug 15[d]	15	VLBA	40
1997 Aug 15	22	VLBA	40
1998 Apr 7	4.8	VLBA+EB+**HALCA**	780
1998 Apr 8	1.6	VLBA+RO+GO+**HALCA**	600
1998 Jun 24[b]	8.4	VLBA+GC+GN+KK+ MC+ON+WF	20
1999 Jul 19[a]	15	VLBA−SC	40
2001 Mar 5	1.6	VLBA+GO+RO+**HALCA**	480
2001 Mar 6	4.8	VLBA−HN+**HALCA**	540

Note. — EB, Effelsberg (Germany) 100 m, GC, Gilcreek (USA) 26 m GN, Green Bank (USA) 20 m; GO, Goldstone (USA) DSN 70 m; HN, Hancock VLBA 25 m; KK, Kokee Park (USA) 20 m; MC, Medicina (Italy) 32 m; ON, Onsala (Sweden) 20 m; RO, Robledo (Spain) DSN 70 m; SC, St. Croix VLBA 25 m; WF, Westford (USA) 18 m.

[a]VLBA 2 cm Survey of Compact Radio Sources (Kellermann et al., 1998)

[b]RRFID: Radio Reference Frame Image Database (Fey & Charlot, 1997)

[c]ICRF: International Celestial Reference Frame (Ma et al., 1998)

[d]VLBA Project BM082 (Marscher, 1999)

Table 6.2. Summary of VLBA+HALCA Observations

Date	Frequency (GHz)	Obs. Time (hr)	Tracking Stations	Other Telescopes
1997 Aug 4	1.6	7	NZ (3^h)	GO (4^h)
1998 Apr 7	4.8	13	RZ (2.7^h+1.1^h), NZ (3.3^h)	EB
1998 Apr 8	1.6	10	RZ (3.6^h), NZ (4^h)	GO, RO
2001 Mar 5	1.6	8	RZ (1^h), NZ (2^h)	RO (4^h), GO (7.5^h)
2001 Mar 6	4.8	9	RZ (0.5^h), NZ (1^h)	...

Note. — RZ, Robledo tracking station; NZ, Green Bank tracking station; EB, Effelsberg (100 m); RO, Robledo (70 m); GO, Goldstone (70 m).

VLBI (VSOP) observations obtained on 2001 March 5 and 6 (see Table 6.2).

6.2.1 Data Reduction

Space VLBI Observations

We consider new Space VLBI images at three different epochs: 1997.8, 1998.4, and 2001.3. VSOP (VLBI Space Observatory Programme) observations combine data from ground arrays, such as the VLBA, and the 8 m orbiting antenna on board the satellite HALCA. For the latter two epochs observations at 1.6 and 4.8 GHz were performed on successive days to minimize flux density variability problems in spectral index mapping. The first Space VLBI observation was conducted at 1.6 GHz only. Further details on these observations are given in Table 6.2.

The standard VSOP observing mode has one polarization (LCP) and two IFs of 16 MHz each with two-bit sampled data. The lowest IF failed in the 1.6 GHz observation in 1997. In 2001, the “a priori” calibration was affected by lack of system temperature measurement for Robledo and Goldstone. A mini-cal procedure was done before starting the experiment in Robledo, providing a value of 20 K that was assumed as constant. For HALCA, we used the nominal system temperatures of 75 K and 77 K for the two IFs at 1.6 GHz, and 88 K and 92 K for those at 4.8 GHz (Hirabayashi et al., 1998, 2000).

All the data were correlated in Socorro and then imported and reduced in AIPS. Global fringe-fitting returned good solutions for all the observations in which

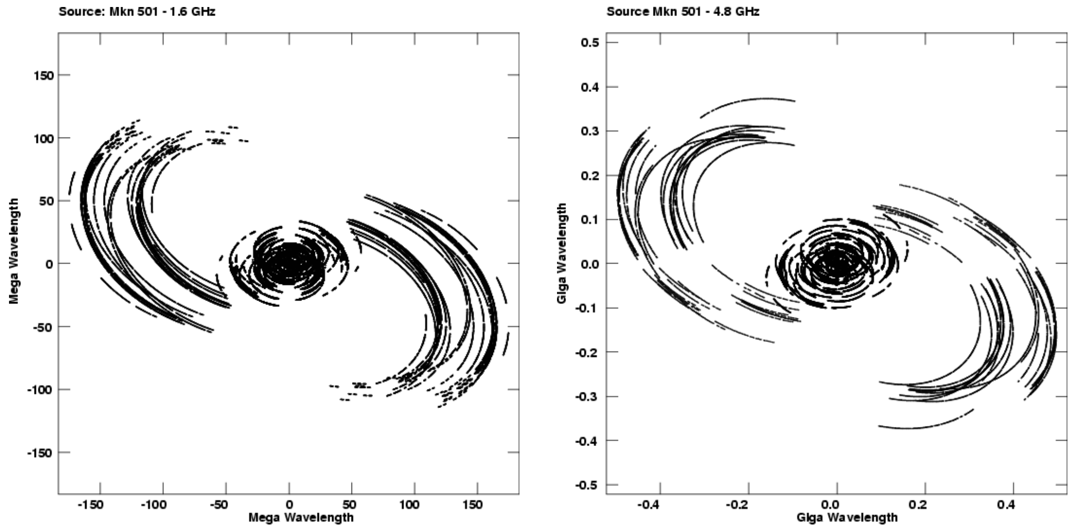

Figure 6.1 (u, v)-coverage of the Space VLBI observations. Left: 1.6 GHz ($\lambda = 18$ cm) on 1998 April 8; right: 4.8 GHz ($\lambda = 6$ cm) on 1998 April 7.

large ground telescopes were used, although no solutions were found for the last observation (2001 Mar 6), unless a value of SNR as low as 4.5 was set in the fit. In spite of such a low signal to noise ratio, we found these solutions reasonable: delays and rates found in this way do not present any discontinuity or suspicious behavior. Thus, we applied these solutions and proceeded with the whole array.

We then performed self calibration using clean-component models, first in phase and, afterward, in both phase and amplitude. In the latter, we repeated the task several times, increasing the baseline range. This revealed to be of great importance for those observations where gain information for some antennas was missing. For example, we could self-calibrate the shortest space-ground baselines using 'uniform weight' ground-only images; in fact, we have similar baselines both in the ground array and to HALCA, as provided by its highly elliptical orbit (see Fig. 6.1). Figures 6.2 – 6.5 present all the images, in order of decreasing angular resolution.

Ground Observations

Images from some of the previous observations have been published or made available to the scientific community on open web sites. However, for the sake of completeness and homogeneity, we requested and obtained the calibrated (u, v)-data for all observations presented here. After the initial reduction (see notes to Table 6.1 for references), we imported the calibrated data into the NRAO Astronomical

Table 6.3. Observational Parameters

Date	Frequency (GHz)	HPBW[a] (mas)	Noise Level (mJy/beam)	Peak Flux Density (mJy/beam)
1995 Apr 7	15	0.6 × 0.9	0.20	485
		1.2	0.25	524
1995 Apr 12	8.3	1.2	0.40	524
1995 Dec 15	15	0.6 × 0.9	0.35	508
		1.2	0.30	546
1996 Apr 23	8.3	1.2	0.25	521
	15	0.6 × 0.9	0.30	490
		1.2	0.35	520
1996 Jun 7	8.1	1.2	0.40	535
1997 Mar 13	15	0.6 × 0.9	0.15	381
		1.2	0.20	410
1997 Apr 25	15	0.6 × 0.9	0.10	360
		1.2	0.15	390
	22	0.3 × 0.5	0.15	327
1997 May 26	15	0.6 × 0.9	0.10	408
		1.2	0.10	438
	22	0.4 × 0.6	0.20	334
1997 Aug 4	1.6	1.5 × 2.9	2.3	409
1997 Aug 15	15	0.6 × 0.9	0.20	455
		1.2	0.15	487
	22	0.3 × 0.5	0.25	350
1998 Apr 7	4.8	0.6 × 0.9	0.40	465
		1.2	0.25	509
1998 Apr 8	1.6	1.5 × 2.9	0.12	421
1998 Jun 24	8.6	0.6 × 0.9	0.25	477

Image Processing System (AIPS) and inspected them carefully. Then, we produced new images; one or more self-calibration cycles proved to be useful in some cases, providing a better signal to noise ratio. We adopted the appropriate (u, v)-range, weights, cell-size and angular resolution to map the spectral index and to look for proper motion of the jet substructures; we present parameters of final images in Table 6.3.

Table 6.3 (cont'd)

Date	Frequency (GHz)	HPBW[a] (mas)	Noise Level (mJy/beam)	Peak Flux Density (mJy/beam)
		1.2	0.35	508
1999 Jul 19	15	0.6×0.9	0.20	446
		1.2	0.20	480
2001 Mar 5	1.6	1.5×2.9	0.50	316
2001 Mar 6	4.8	1.2	0.50	428

[a]Column 3: circular beam or RA $\times$ Dec in PA 0°

6.2.2 Component Fitting

Identification of components is usually the most difficult problem affecting proper motion studies. Long time intervals between epochs can lead to misidentification of components; moreover, the use of different resolutions can cause confusion, for example by blending components with different properties and velocities; finally, registering images at different observing frequencies is also necessary: the apparent core shift due to the different spectral index of the core and jet can be significant.

In the present work, the time coverage is very dense (14 epochs over 4 years, plus the final VSOP observation) and there are no large time gaps. To prevent angular resolution problems, we produced maps at the same resolution at all epochs. Even if some observations allowed a better resolution, we convolved all the images obtained at a frequency $5\,\mathrm{GHz} \leq \nu \leq 15\,\mathrm{GHz}$ with a circular restoring beam of 1.2 mas FWHM. However, higher resolution maps have also been made, in order to provide more information when needed. In particular we obtained images at a resolution of 0.6×0.9 mas (RA $\times$ Dec) in all observations with good (u, v)-coverage on long baselines (see Table 6.3). A comparison of fit components in convolved and full resolution images revealed good agreement.

The fit to the components of the jet was done within AIPS and the Difmap package (Shepherd, Pearson, & Taylor, 1994, 1995). In AIPS we used the task `JMFIT`, which allows one to fit Gaussian components to part of an image. Up to four components can be used at a time and the task, starting from given initial conditions, solves in an iterative way for position, flux density and extension of each component. Since more than four components are needed to properly fit the images, we had to run the task several times on different regions. The regions were made to overlap with each other in order to obtain consistent results. We also repeated the fit looking for "stable" solutions, i.e., changing our initial guesses or even leaving them blank. Eventually, very good models were obtained; the difference in flux density between our fits and the images is always smaller than 5%.

Using Difmap, we also carried out model-fitting to the visibilities rather than the image. Similarly to the fits made in AIPS, four to six jet components were required in addition to the core to provide a good representation of the data.

6.2.3 Spectral Index Mapping

When producing spectral index images, there are three main effects that have to be carefully taken into account. First, because of flux density variability and possible proper motion of components, the observations must be taken at very close epochs. Next, the angular resolution must be the same at both frequencies and the (u, v)-coverage as similar as possible; this guarantees the same sensitivity to extended structures in the high and low frequency images. Finally, as absolute position is not available, we need to properly align the images before combining them.

To meet the first two requirements, we produced spectral index images using data separated by less than 24 hrs. We considered 15 and 22 GHz data obtained on the same day (1997 Aug 15) and Space VLBI observations at 1.6 and 5 GHz made on successive days (1998 Apr 7 and 8 — see Edwards et al., 2000, for a preliminary analysis). We note that 1998 Space VLBI observations have better (u, v)-coverage than those in 2001 (see Fig. 6.1). To obtain matching (u, v)-coverages, we cut the shortest baselines from the low frequency data and the longest baselines in the high frequency observations. Images were then obtained using uniform weights, and the same cell-size and restoring beam.

The problem in registering the images is that the peak of the image, coincident with the core, can correspond to different positions at different frequencies if the core is self-absorbed. So, we aligned the images using the positions of components along the jet in a region with steep spectral index and no self-absorption effects. We found that at 15 and 22 GHz no shift was necessary, while a shift of $\sim$0.2 mas was necessary in both RA and Dec between the 5 and 1.6 GHz images.

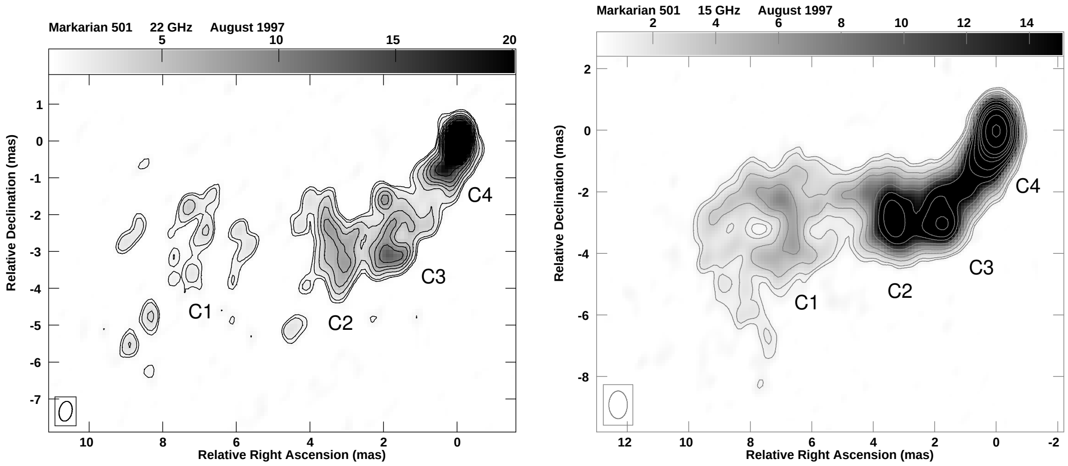

Figure 6.2 Isocontour levels of Mkn 501 at 22 GHz (left) and 15 GHz (right) from the August 1997 epoch. Left: the HPBW is 0.54×0.35 mas in PA $-11°$; noise level is 0.3 mJy/beam; contours are drawn at 1, 1.5 3, 5, 7, 10, 15, 20, 30, 50, 70, 100, 200, and 300 mJy/beam; the greyscale range is 0.3–20 mJy/beam. Right: the HPBW is 0.6×0.9 mas (RA $\times$ Dec). The noise level is 0.2 mJy/beam. Contours are drawn at 1, 1.5 3, 5, 10, 15, 20, 30, 50, 70, 100, 200, and 400 mJy/beam; the greyscale range is 0.3–15 mJy/beam. At 22 GHz, the limb brightened structure is visible even in the innermost region of the jet. At 15 GHz, it is clearly visible in the (resolved) C1 region, but no longer in the inner region because of the lower resolution.

6.3 Results

6.3.1 Source Morphology

The large scale radio structure has been imaged with the VLA (Ulvestad et al., 1983; Van Breugel & Schilizzi, 1986; Cassaro et al., 1999), showing a core dominated source with two-sided diffuse emission oriented at PA $\sim 45°$; this indicates that the jets are non relativistic at a (projected) distance of ~ 10 kpc from the core. The pc-scale structure has also been investigated, using VLBI techniques (see e.g. Conway & Wrobel, 1995), with resolution of ~ 10 mas. However, the collection of multi-epoch, multi-frequency, high resolution and high sensitivity images will improve our knowledge of the source morphology and evolution. The present VLBI observations show a strong core and a one-sided jet. The jet exhibits multiple sharp bends before undergoing a last turn, followed by rapid expansion. We can distinguish three different regions:

- a first region, extending ~ 10 mas from the core, where a high brightness jet structure is present (Fig. 6.2 and 6.3). The jet PA is not constant in this region, being $150° - 160°$ near the core (< 1 mas) and moving to $\sim 145°$ (from

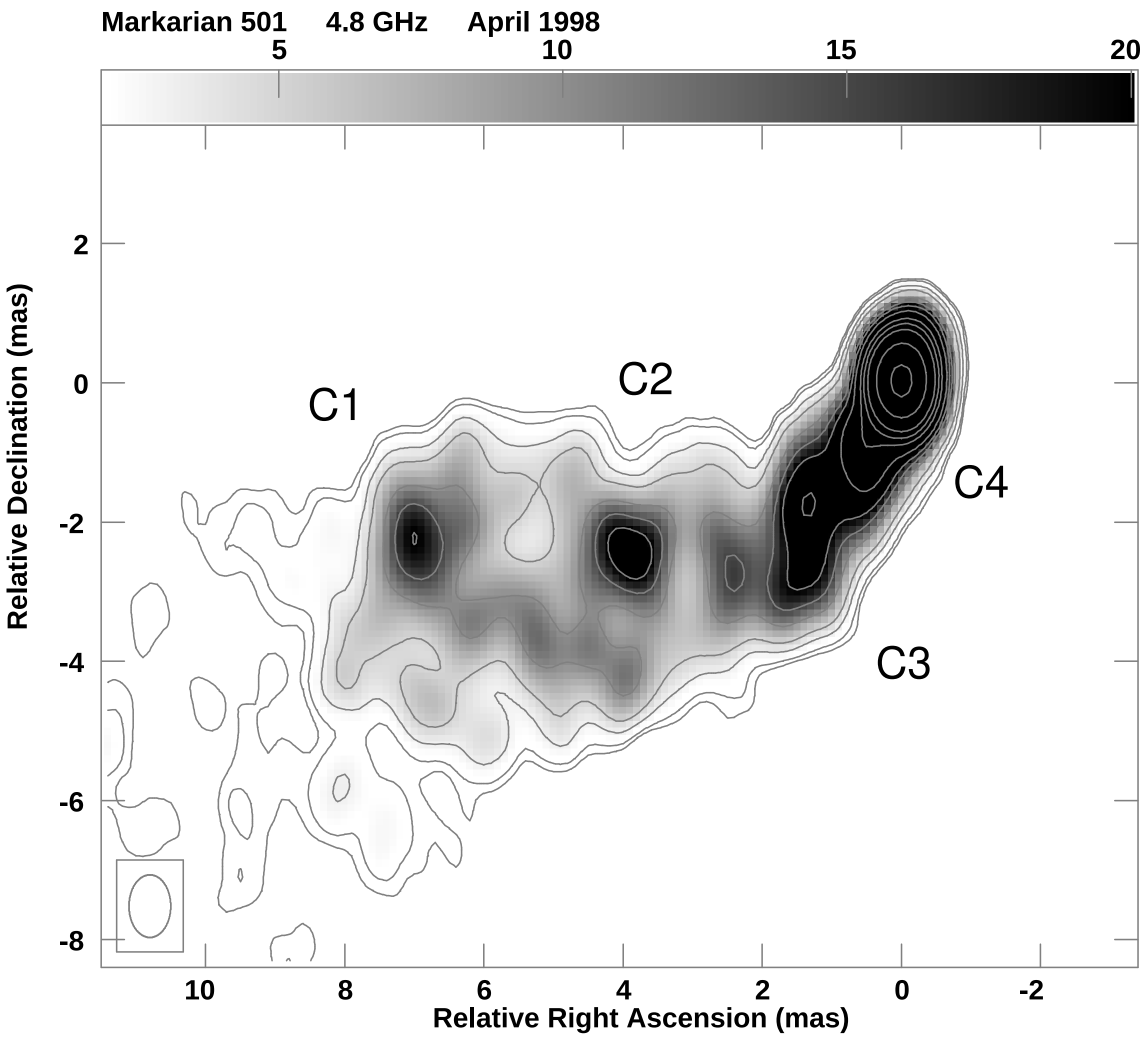

Figure 6.3 Gray scale plus isocontour levels of Mkn 501 from the 5 GHz VSOP observation in April 1998. The HPBW is 0.6×0.9 mas (RA $\times$ Dec). Contours are drawn at 1, 1.5 3, 5, 10, 15, 20, 30, 50, 70, 100, 200, and 400 mJy/beam; the greyscale range is 2–20 mJy/beam.

1 to ~ 4 mas from the core) to become $\sim 90°$ from 4 to 10 mas.

The 22 GHz high resolution image (Fig. 6.2, left) shows that the jet is resolved and limb-brightened starting at ~ 1 mas from the core. This is confirmed by the high sensitivity 5 GHz Space VLBI image (Fig. 6.3); although this image does not have enough angular resolution to resolve the inner jet near to the core, it shows an extended low brightness emission, confirming the transverse extension of the jet in the inner 2 mas. In the region from 2 to 10 mas from the core, the limb brightened jet structure is clearly visible.

The brightness profile along the main axis of the jet is not uniform; high brightness regions are followed by dimmer regions. In particular at 5–6 mas from the core a deep minimum is present just before an extended bright spot with a peak 8–9 mas from the core. However, we do not refer to these regions as "knots", since they are resolved at higher frequencies.

- between ~ 10 mas and ~ 30 mas from the core, the jet loses its collimation and becomes visible only in lower resolution images (Fig. 6.4). In this region, the jet is oriented at a PA of $\sim 110°$ and its opening angle is increasing. A well defined limb brightened structure is visible (see, e.g., Fig. 6.4, right), in agreement with the "layered" structure visible in the polarized emission (Aaron, 1999). As in the first region, lower frequency images reveal a wider jet and a more evident external shear layer; this implies that the spectra in the inner regions are flatter than in the external regions.
- at ~ 30 mas from the core the jet shows strong bending and a large opening angle (Fig. 6.5). In this third region the orientation of the diffuse jet is in agreement with the orientation of the kpc-scale emission. The jet opening angle is $\sim 43°$. The radio brightness is uniform and there is no indication of the helical structure suggested by Conway & Wrobel (1995), which possibly resulted from the poor (u, v)-coverage (five telescopes only) of their observations. A limb-brightened structure is visible in our low resolution images up to ~ 100 mas from the core, as can be seen in Fig. 6.5.

No radio emission is detected either on the opposite side of the radio core or in the position of the putative counterjet feature F reported by Conway & Wrobel (1995). However, if we compare our measured total flux densities to single dish data (e.g.

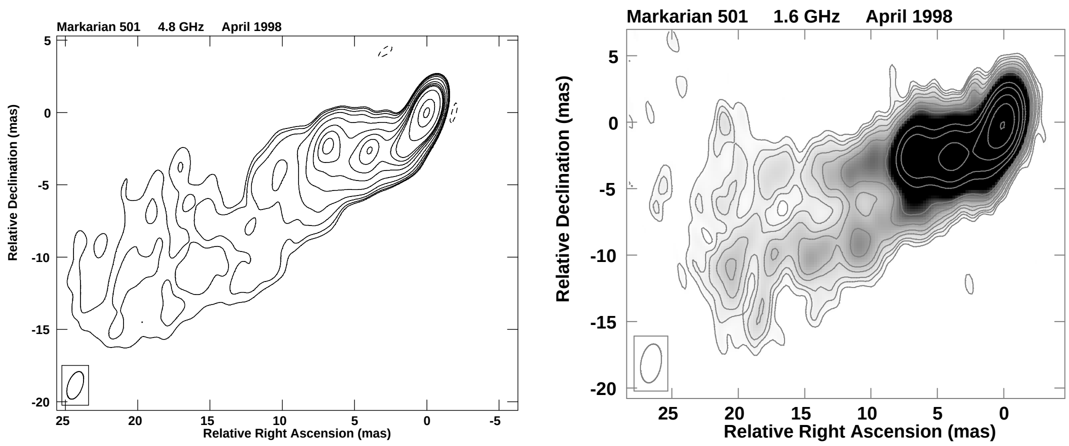

Figure 6.4 Isocontour levels of Mkn 501 from the VSOP observation in April 1998 at 5 GHz (left, HPBW 2×1 mas in PA $-20°$) and at 1.6 GHz (right, HPBW 3×1.5 mas in PA $-10°$). Contours are drawn at -3, 1.5, 2, 3, 5, 10, 20, 30, 40, 50, 100, 300, and 500 mJy/beam; the greyscale range is 0.80–15 mJy/beam (right image only).

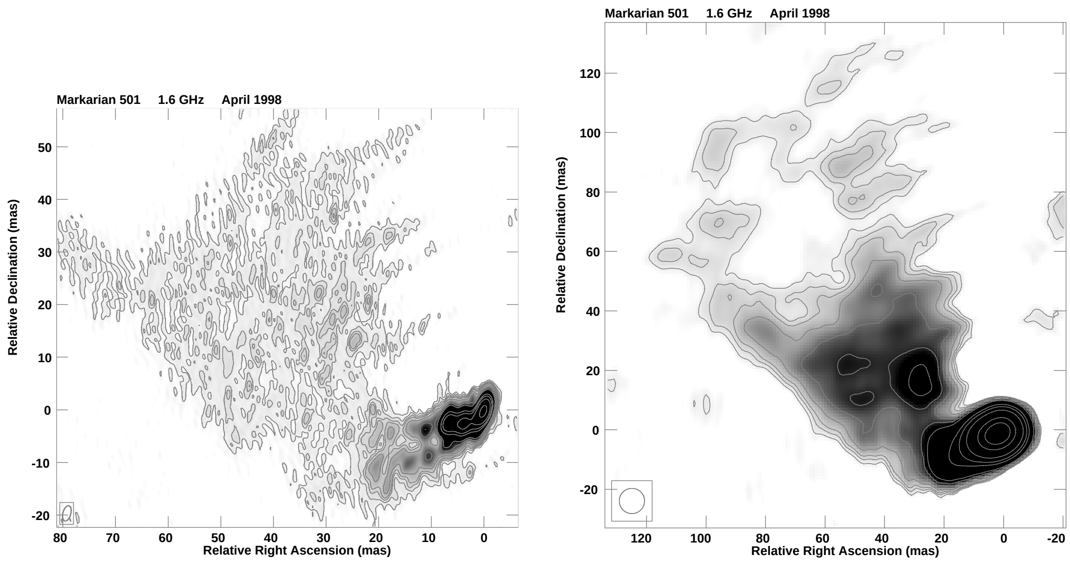

Figure 6.5 Gray scale plus isocontour levels of Mkn 501 from the 1.6 GHz VSOP observation in April 1998. Left: the HPBW is 3×1.5 mas at PA $-10°$. Contours are drawn at 0.5, 1, 1.5, 2, 3, 5, 7, 10, 30, 50, 100, and 300 mJy/beam; the greyscale range is 0–10 mJy/beam. Right: the image is convolved with circular beam of 8.5 mas FWHM. The image noise level is 0.4 mJy/beam. Contours are drawn at 1, 1.5, 2, 3, 5, 7, 10, 30, 50, 100, 300, and 500 mJy/beam; the greyscale range is 0.50–8 mJy/beam.

from the UMRAO database[2]), the correlated VLBI flux density accounts only for a part of the total flux density ($\sim 70\%$ at 5 GHz and $\sim 65\%$ at 15 GHz); this is in agreement with the presence of a larger scale structure resolved out by the VLBI data, such as the two sided emission shown by Ulvestad et al. (1983) and Cassaro et al. (1999).

6.3.2 Radio Flux Densities and Variability

Single dish monitoring of Markarian 501 shows that this source is remarkably stable in the radio band. Venturi et al. (2001) monitored a sample of 23 $\gamma-$ and X$-$ray loud blazars over a 4 year period (1996–2000) with the 32 m Medicina radio telescope. From their data, Markarian 501 is the most quiescent source, with an almost flat light curve at both 5 and 8.4 GHz. Moreover, Markarian 501 is part of the UMRAO database, which also shows a fairly steady flux density. During the period of our observation, the average flux densities are (1.54 ± 0.12) Jy at 4.8 GHz, (1.53 ± 0.13) Jy at 8 GHz and (1.29 ± 0.08) Jy at 14.5 GHz.

We consider the VLBI core flux density using our data at 15 GHz (0.6×0.9 mas FWHM, RA $\times$ Dec), where we have 8 different epochs (see Table 6.3). Assuming the map peak as the core flux density, we see some dispersion in the values, which range between 360 mJy (1997 Apr 25) and 508 mJy (1995 Dec 15). This suggests possible core variability, which is diluted in single dish observations, since the VLBI core makes up only $\sim 30\%$ of the total flux density. We note, however, that our observations are not homogeneous and were not aimed to monitor flux density variability.

6.3.3 Proper Motion

The overall morphology of the source does not present dramatic changes between epochs. No compact jet component (knot) is present in the jet at all frequencies: if we consider the highest resolution data, the local peaks present in the low resolution images become clearly resolved. Therefore, we limit our study to the innermost region, where high-resolution images are available (the jet brightness is too low to be detected at high frequency beyond 10 mas from the core). In this region, the jet is always transversally resolved: it appears centrally peaked at low resolution, but

[2]see `http://www.astro.lsa.umich.edu/obs/radiotel/umrao.html`

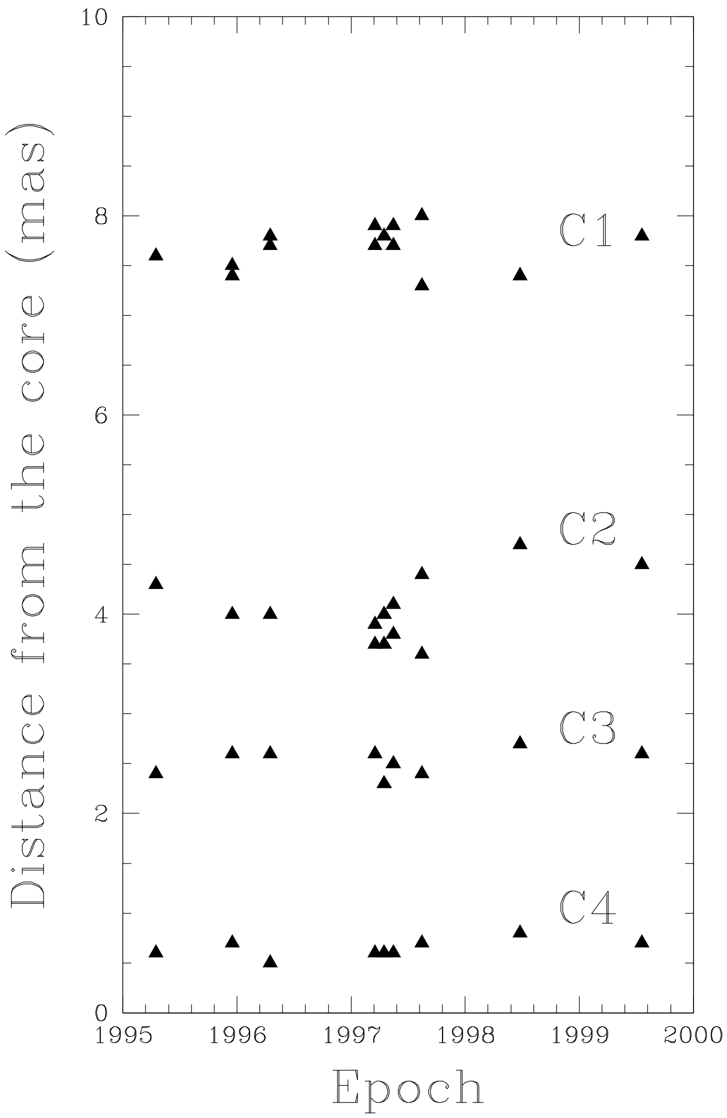

Figure 6.6 Component positions from model-fitting. Distances are given in milliarcsecond. All points are at 15 GHz, with the exception of the 1998.48 epoch which is at 8.4 GHz.

Table 6.4. Results of the Model - Fitting

Epoch	Component					
	C4	C3	C2a	C2b	C1a	C1b
1995.29	0.6	2.4	4.3		7.6	
1995.96	0.7	2.6	4.0		7.4	7.5
1996.29	0.5	2.6	4.0		7.7	7.8
1997.21	0.6	2.6	3.7	3.9	7.7	7.9
1997.29	0.6	2.3	3.7	4.0	7.8	
1997.37	0.6	2.5	3.8	4.1	7.7	7.9
1997.62	0.7	2.4	3.6	4.4	7.3	8.0
1998.48	0.8	2.7	4.7		7.4	
1999.55	0.7	2.6	4.5		7.8	8.9

Note. — Distances from the core, given in milliarcsecond. Tyipical uncertaintes are $\sim 0.1 - 0.2$ mas (see text for discussion).

resolved with a limb brightened structure at high resolution. This implies that we could be mixing together different components with different properties and moving at different velocities. For all these reasons, we analysed images at the best angular resolution (typically 0.6×0.9 mas, RA $\times$ Dec) and, in model-fitting, we tried to use a number of components that did not produce an oversimplified representation of the data. In particular, to avoid resolution or frequency effects, we used only 15 GHz data, plus the 8.4 GHz observation at epoch 1998.48. The results obtained from model-fitting of visibilities in Difmap are presented in Table 6.4 and Fig. 6.6. These results are in agreement with those obtained by fitting Gaussian components to the images (using `JMFIT` in AIPS).

The data are in general well fitted by a core and four jet components, in agreement with Edwards & Piner (2002) (not surprisingly, as most data are the same). We labelled components according to the same notation for ease of comparison: C1 to C4 moving from the outermost component inward. However, for the reasons stated above, we adopted two Gaussians for each of the components C2 and C1 at many epochs. This produced a better fit to the data, in agreement with the resolved limb-brightened jet structure present in these regions. Nominal position errors are very small. The major uncertainty is related to the complex source structure. We estimate a position error of $\leq$0.1 mas for C4, C3, C2 and $\sim$0.2 mas for C1.

From our analysis we conclude that no proper motion is visible in any of the four components. Consider the case of component C2: Edwards & Piner (2002) measured a proper motion of $(0.6 \pm 0.1)c$ for this component. However, we note that at the position of C2 two faint external peaks are visible in the 22 GHz image (Fig. 6.2) on either side of the lower frequency component. They could even have a different spectrum (Fig. 6.9). The peak position visible at lower resolution in the 15 GHz image is therefore the blend of the limb-brightened structure visible at 22 GHz. In the space VLBI image at 5 GHz, the component C2 is at a different position with respect to the 15 GHz images: this could be due to different spectra for the different components. We conclude that it is not possible to measure a proper motion for such a complex structure and that any pattern velocity measurement from low resolution data is not related to the jet bulk speed in this source.

6.3.4 Bulk Motion

Under the assumption of intrinsically symmetric two-sided jets affected by Doppler boosting effects, the observational data allow one to estimate the jet bulk velocity. In the following, we present the results derived from a study of the jet/counterjet ratio, core dominance and jet expansion.

Jet/Counterjet Ratio

From the lack of detection of a counter-jet in all the images (§ 6.3.1), we set a lower limit on the jet/counterjet ratio. We use the highest ratio between the jet brightness and the counterjet upper limit. We estimate this ratio excluding the innermost region of the jet; this avoids contamination from the unresolved central emission. The best image for this analysis is the Space VLBI observation obtained in Apr 1998 at 1.6 GHz. From this image we can derive a jet/counterjet ratio $R > 1250$ (1 rms) at ~ 4 mas from the core. Given the well known relation $R = \left(\frac{1+\beta\cos\theta}{1-\beta\cos\theta}\right)^{2+\alpha}$, and assuming $\alpha = 0.5$ (see §6.3.5), this value yields $\beta\cos\theta > 0.89$. In turn, this implies $\beta > 0.89$ and $\theta < 27°$.

Our deep, low resolution images allow us to also put a constraint at large distance from the core. In particular, in the 1.6 GHz image from the 2001.3 data, at ~ 60 mas from the core we still have R $>$ 70; although less extreme, this value is also very interesting, as it implies that the jet remains at least mildly relativistic ($\beta\cos\theta > 0.69$) even at large distances from the core.

It is not possible to extend this analysis further with our data. However, we remind the reader of the symmetric morphology of the source on the kpc scale (§ 6.3.1). This implies that the bulk of the jet slows to subrelativistic speed going from the parsec to the kpc scales.

Core Dominance

Given the general relation between total and core radio power (Feretti et al., 1984; Giovannini et al., 1988, 2001; de Ruiter et al., 1990), we can use low frequency unboosted data to compute an "expected" value for the core power. A comparison between the expected and measured 5 GHz core radio power allows to constrain the jet orientation and velocity (Giovannini et al., 2001). We note that at 5 GHz self-absorption effects are small (see § 6.4.2); however, to take also into account possible core variability, we allow the observed core flux density to vary by a factor of 2. This is a conservative assumption, based on the total flux density monitoring and the range of derived VLBI core flux densities (see § 6.3.2), and, more generally, on statistical flux density variability of AGN in the radio.
To estimate the orientation and jet velocity for Mkn 501, we have compared its total unboosted flux density (1.81 Jy) at 408 MHz (Ficarra et al., 1985), with the nuclear flux density at 5 GHz. Since Giovannini et al. (2001) used the arcsecond core radio power to derive their correlation, we adopted the total VLBI correlated flux density at 5 GHz ($\sim$800 mJy) as the Mkn 501 core flux density. Any possible underestimate in this assumption is compensated for by the allowed range (a factor of 2) in flux density variability. We found that Mkn 501 has to be oriented at $\theta \leq 27°$ with $\beta \geq 0.88$. We note that a high jet velocity ($\beta > 0.95$) is allowed only in the range $10° < \theta < 27°$. High velocities are forbidden at smaller angles; the resulting Doppler factor would require a core much brighter than observed.

Adiabatic Model

The functional dependence of the jet intensity on the jet velocity and radius for an adiabatically expanding jet has been discussed in the case of relativistic motion by Baum et al. (1997). Since the model represents a simplification of the real situation, the results should be considered with caution and compared with other observational results. This model has enabled useful constraints to be placed, in agreement with

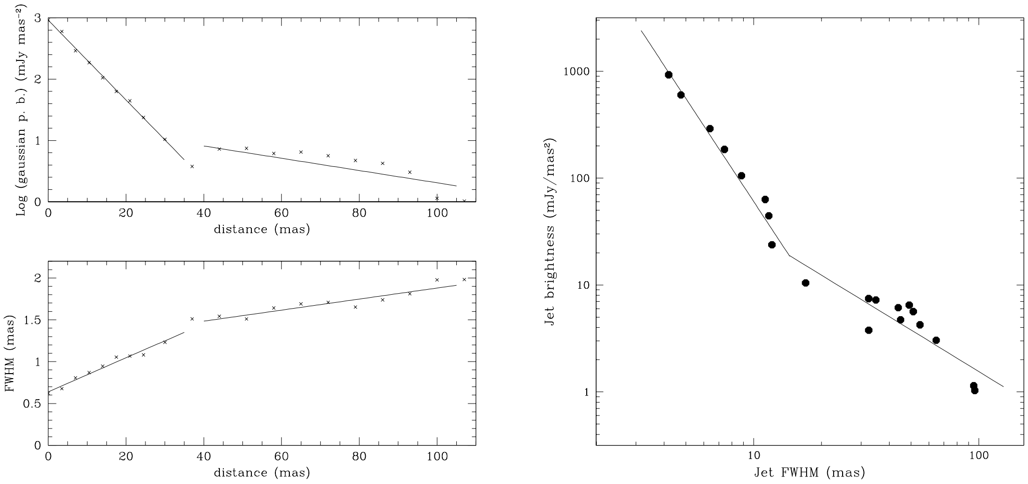

Figure 6.7 Left: plots of peak brightness (top) and FWHM (bottom) of Gaussian model fits vs. distance from the core, with least-squares fits represented by the straight lines; note the clear change in behavior at about 35 mas from the core. Right: peak brightness vs. FWHM of Gaussian model fits; straight lines represent least-squares fits; the change in slope at FWHM$\sim$ 15 mas corresponds to the transition between the two zones visible in the left panel. The power law slopes are -3.2 and -1.3.

other data, for 3C 264 (Baum et al., 1997) and other sources, such as NGC 315 (Cotton et al., 1999) and 3C 449 (Feretti et al., 1999).

To apply this model we used our deep VSOP observations at 1.6 GHz obtained in March 2001 and in April 1998. In these observations, the jet emission is visible on scales up to $\sim$ 150 mas (see, e.g., Fig. 6.5). First, we derived brightness profiles across the jet; we used the AIPS task `SLICE` on an image reconstructed with a circular beam of 7 mas diameter, where the longest baselines have been omitted to increase the signal to noise ratio. In the innermost region ($<$ 25 mas from the core), we have 8 slices, taken every half beam-width at PA 27.2°. After the main bend, we considered 12 more slices, each one beam apart, at PA $-57.1°$. We stopped our analysis $\sim$ 100 mas from the core; further out, the low jet brightness and the presence of extended sub-structures do not allow the data to be fitted well.

Using the AIPS task `SLFIT`, we fitted single Gaussians to each profile. This could be done unambiguously in most cases, although in a few slices some deviation from a pure single Gaussian profile was present. However, the difference between the area subtended by the profile and the fit is always smaller than 5% and does not affect the analysis. We plot the resulting FWHMs and peak brightnesses in Fig. 6.7; the quantities have been deconvolved from the CLEAN beam, according to the formula given by Killeen et al. (1986). There are clearly two regimes; least-squares fits yield a power-law of index -3.2 in the inner jet (< 30 mas from the core) and -1.3 in the outer regions. In the following, we use these best-fit solutions rather then the actual data; this prevents us from spurious results brought about by random fluctuations.

We recall the equations given in Baum et al. (1997) for the jet surface brightness I_ν:
$I_\nu \propto (\Gamma_j v_j)^{-(\delta+2)/3)} r_j^{-(5\delta+4)/3)} D^{2+\alpha}$ (predominantly parallel magnetic field)
$I_\nu \propto (\Gamma_j v_j)^{-(5\delta+7)/6)} r_j^{-(7\delta+5)/6)} D^{2+\alpha}$ (predominantly transverse magnetic field).

We assume an injection spectral index $\delta = 2$, as suggested from the average α in the image, excluding the self-absorbed core (§ 6.3.5). It is not easy to decide which magnetic field regime is preferable: according to the 8.4 GHz images of Aaron (1999), the Mkn 501 jet is highly polarized at the edges with the magnetic field parallel to the jet flow, while in the jet spine the magnetic field is orthogonal to the jet flow with a lower degree of order. Pollack et al. (2003) report a 5 GHz electric vector PA distribution consistent with this result but the lower resolution renders the results less conclusive. Therefore, since the percentage of ordered field and the intrinsic orientation are not well known, we consider the two cases of pure parallel and perpendicular magnetic field orientation; in a disordered magnetic field, the real result will be in between the two extreme situations. Figure 6.3.4 shows the derived trends of β for an initial Lorentz factor $\Gamma = 3.2$ and $\Gamma = 15$ ($\beta_i = 0.95, 0.998$) with parallel and perpendicular magnetic fields. In each plot, we draw five lines, corresponding to angles to the line of sight of $5°$, $10°$, ..., $25°$ (i.e., in the range of values allowed by the jet sidedness and core dominance).

We note that the jet velocity decreases with the core distance, more slowly in the perpendicular case, and on a shorter scale in the parallel case. The lack of detection of the CJ in all our images strongly constrains any possible model since it implies a relativistic jet also at large distance from the core (> 50 pc). Models with low initial Lorentz factor ($\Gamma < 5$) are definitely ruled out, regardless of the assumed magnetic field orientation, since they disagree with both the observed limb-brightened structure (§ 6.4.1) and the jet/counterjet ratio (at least in the case of the parallel magnetic field); moreover, they require a jet deceleration (§ 6.4.1) between the $\gamma-$ray region and radio jet region that is too strong. Among models with a higher initial speed ($\Gamma = 15$), the case of the parallel magnetic field requires an orientation angle of $25°$, at least at > 70 mas from the core, to be in agreement

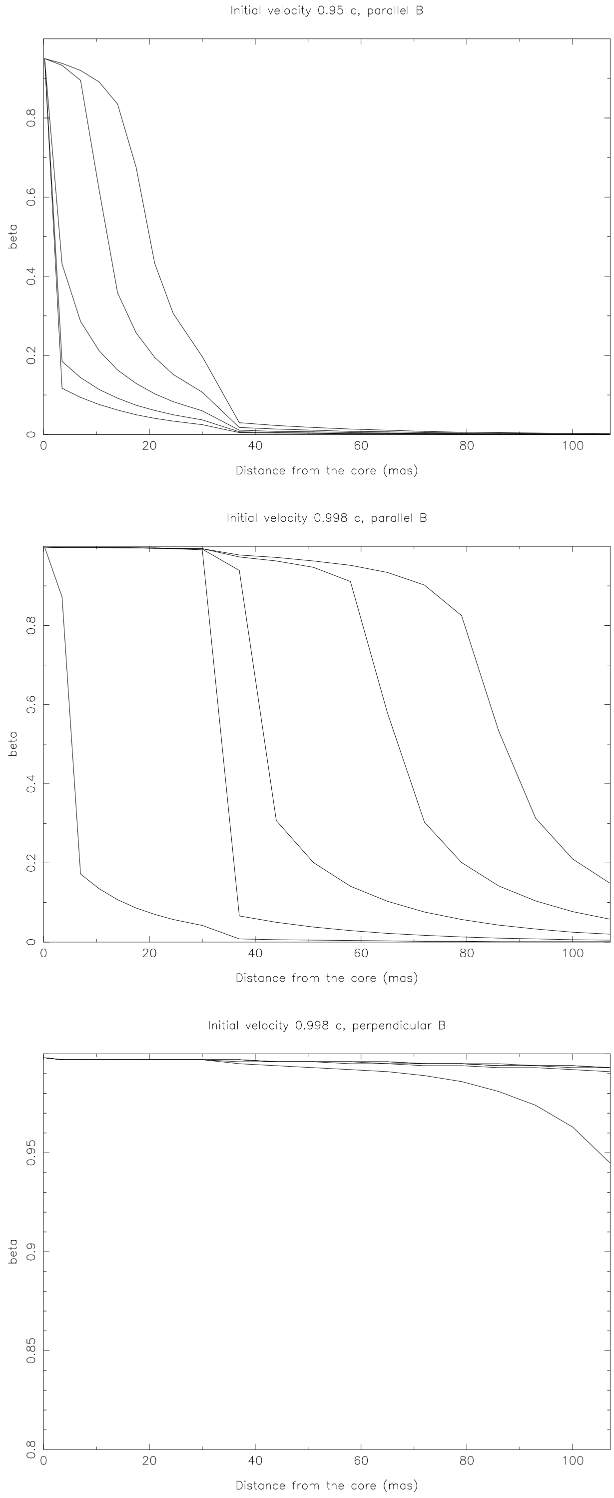

Figure 6.8 Results of the adiabatic model fit. The low initial velocity with parallel magnetic field is at top; middle and bottom plots show high initial velocities ($\beta_i = 0.998$) for a parallel and perpendicular magnetic field, respectively. Orientation angles of $5°, 10°, 15°, 20°, 25°$ are drawn in each plot, with angle increasing from bottom left to top right. For illustration purposes, the vertical axis in the bottom plot spans only the range 0.8–1.

Table 6.5. Spectral Index Results

Image	beam	PA	core	C4	C4toC3	C3	C3toC2	C2	C2toC1	C1
$\alpha_{4.8}^{1.6}$	1.7×0.9	$-25°$	-0.45	-0.2^*	0.6^*	0.1	0.9	0.6	0.7	0.3
α_{22}^{15}	0.6×0.9	$0°$	0.45	0.80	2	0.65	$\cdots$	0.70	2.4	resolved
$\alpha_{4.8}^{1.6}$	3.3×1.3	$5°$	-0.3	confused due to low resolution						

Note. — Results of the spectral index imaged in Figures 6.10, 6.11. Typical uncertainties are ± 0.05. Data marked with an asterisk (*) are estimated after core subtraction and have larger uncertainties.

with the observed jet/counterjet brightness ratio. We cannot exclude models with a narrow angle to the line of sight at small distances from the core, where solutions are similar. In the case of the perpendicular magnetic field, the constraints are less severe since we have a fast jet even at large distances from the core.

6.3.5 Spectral Index

In Fig. 6.9, 6.10 and 6.11, we display the spectral index distribution at various resolutions between 1.6 and 4.8 GHz and between 15 and 22 GHz. Observational results are summarized in Table 6.5 for high resolution images and described in the following subsections.

Low Frequency Range: $\alpha_{4.8}^{1.6}$

At low resolution (3.3×1.3 mas, PA $= 5°$), we can study the spectral index distribution at distances from the core larger than 8–10 mas (Fig. 6.9). The limb-brightened jet structure between 8 and 20 mas from the core is clearly visible. The spectrum is always flat in the inner spine (medium value $\alpha = 0.08$) and steep in the bright shear regions, with values in the range $0.9 \sim 2.1$. In the inner region (< 8 mas from the core), the jet is well resolved with a steep spectrum in the more external regions ($0.7 \sim 1.0$) but with a puzzling region south of the high brightness region where the spectral index is $\alpha \sim -0.1$. This region is clearly visible also in the lower resolution image in Edwards et al. (2000) where it seems connected to the inner spine flat spectrum region, while no such connection is present in the total intensity images.

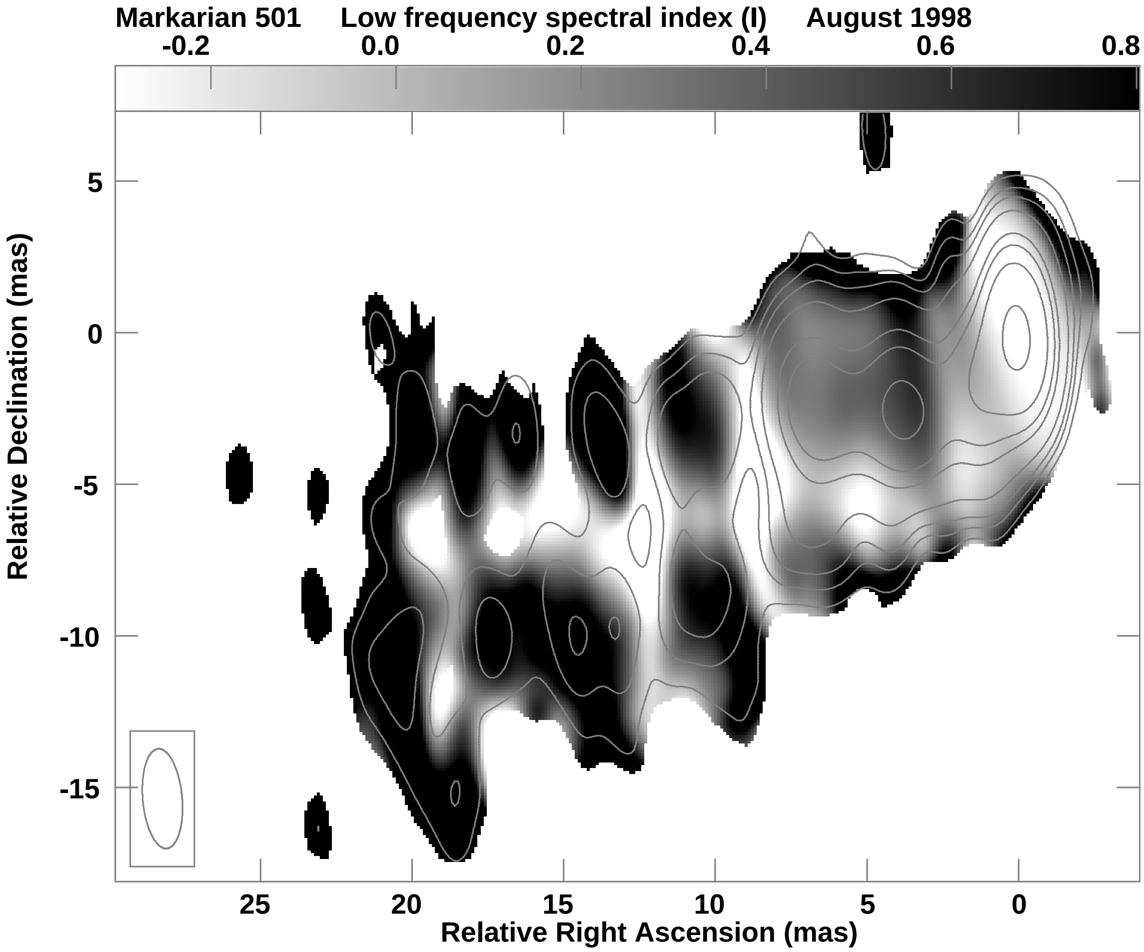

Figure 6.9 Low frequency, low resolution spectral index image: $\alpha_{1.6}^{4.8}$ with 3×1.5 mas HPBW (PA 10°). Contours show total intensity levels at 1.5, 3, 5, 10, 30, 50, 100, and 300 mJy/beam (at 1.6 GHz); the greyscale is the spectral index from -0.3 (inverted) to 0.8 (steep).

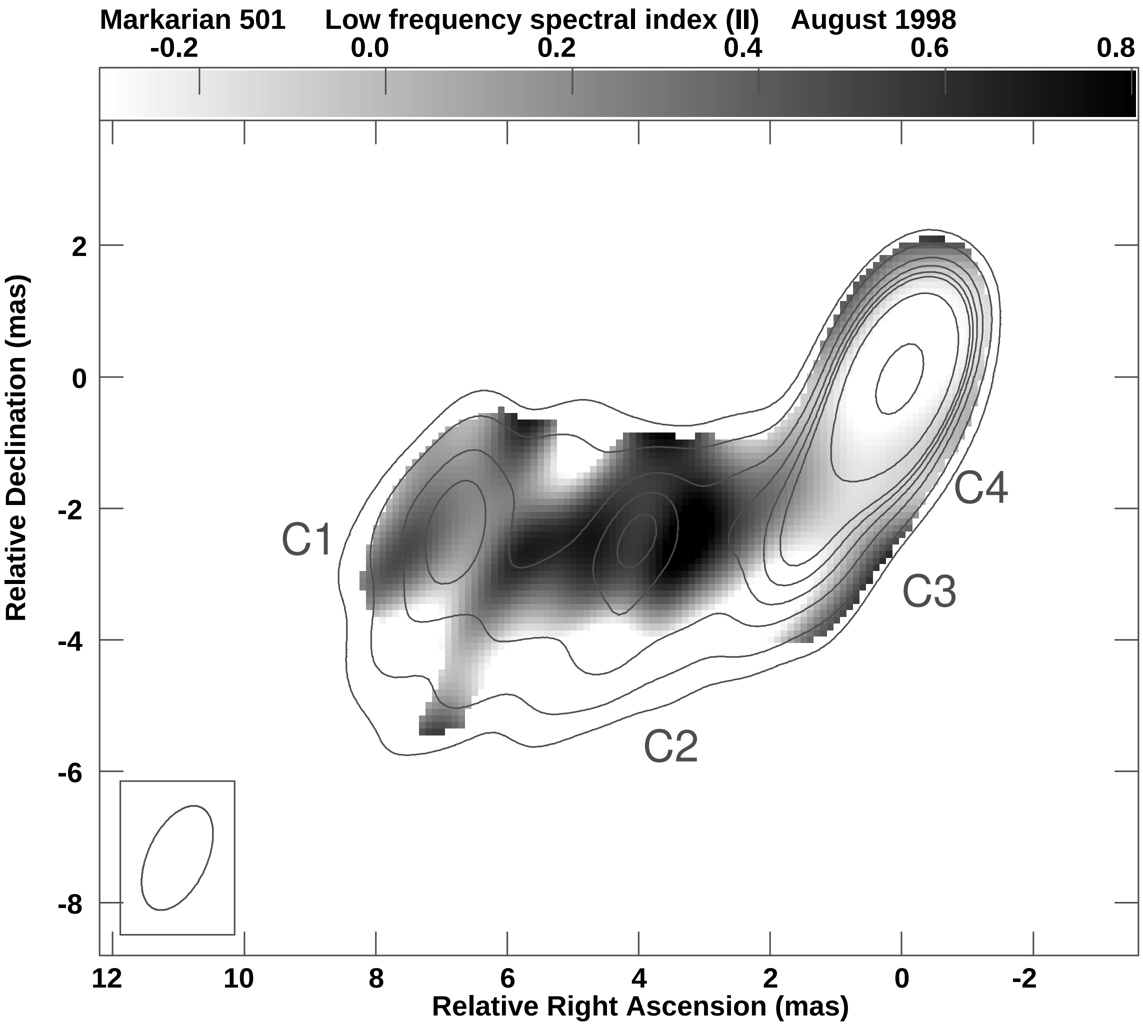

Figure 6.10 Low frequency, high resolution spectral index image: $\alpha_{1.6}^{4.8}$ with 2×1 mas HPBW (PA $-20°$). Contours show total intensity levels at 5, 10, 20, 30, 40, 50, 100, 400 mJy/beam (at 4.8 GHz); the greyscale is the spectral index from -0.3 (inverted) to 0.8 (steep).

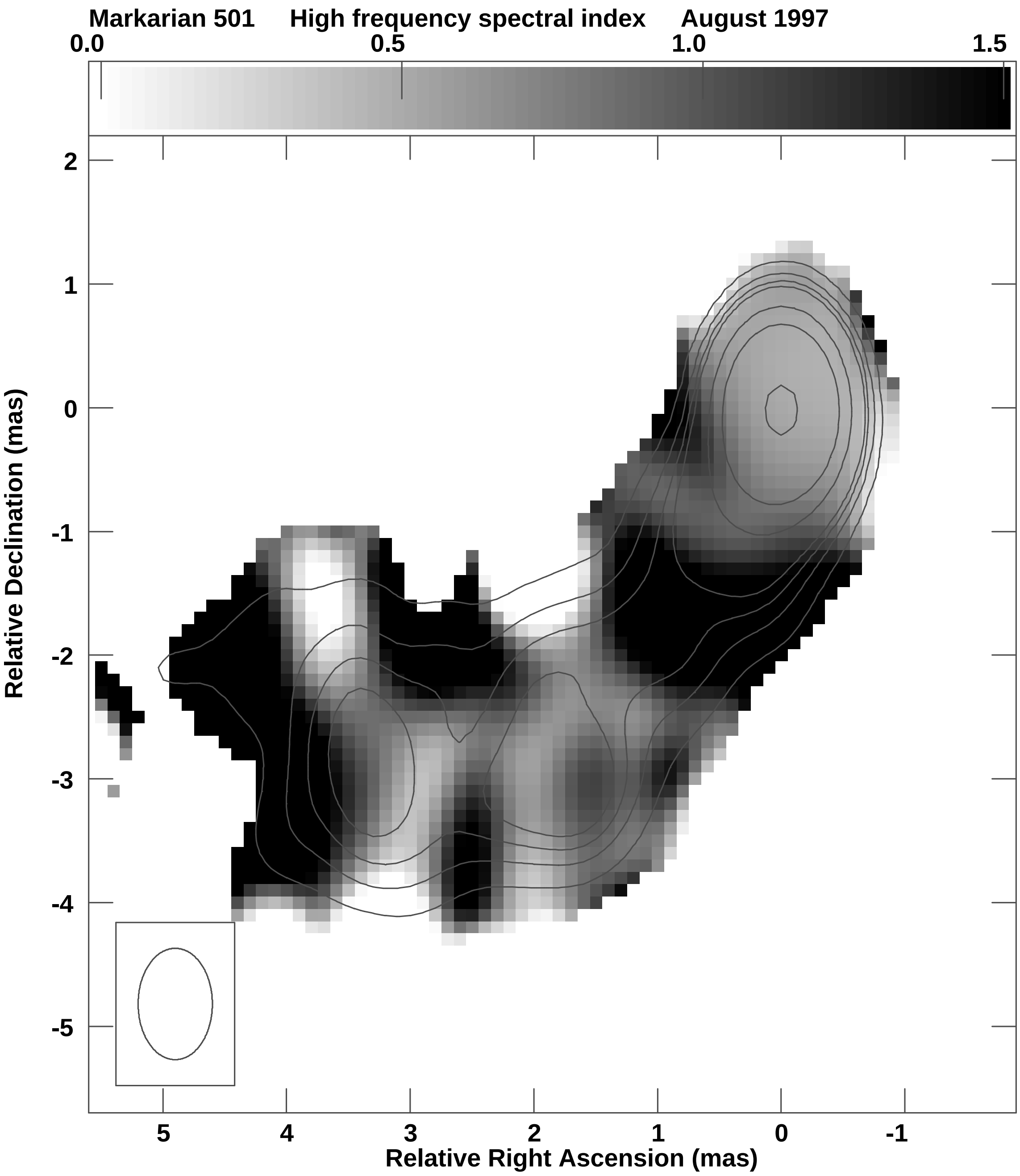

Figure 6.11 High frequency, high resolution spectral index image: α_{15}^{22} with 0.6×0.9 mas HPBW (RA $\times$ Dec). Contours show total intensity levels at 5, 10, 15, 20, 50, 100, and 400 mJy/beam (at 15 GHz); the greyscale is the spectral index from 0 (flat) to 1.5 (steep), where $S(\nu) \propto \nu^{-\alpha}$.

Using the space VLBI baselines, we can study the source details at higher angular resolution (1.7×0.9 mas, PA $= -25°$) even at this frequency (Fig. 6.10). The nuclear spectrum is inverted ($\alpha_{4.8}^{1.6} = -0.45$). Except for C4 (confused with the core and subject to a large uncertainty), the jet sub-components show flat to moderately steep spectra: $0.1 < \alpha_{4.8}^{1.6} < 0.6$. Regions in between the components have steeper spectra.

High Frequency Range: α_{22}^{15}

At these high frequencies, we are beyond the self-absorption turnover and the nuclear region shows a flat, non-inverted spectrum ($\alpha = 0.45$), generally steepening along the jet. The resolution of 0.6×0.9 mas (RA $\times$ Dec, Fig. 6.11) shows that the inner regions C4, C3, C2 have α_{22}^{15} in the range $0.60 \sim 0.80$, while regions in between are much steeper ($\alpha \sim 2$ and higher). The large component C1 is too faint and resolved to be properly imaged at these high frequencies. A marginal suggestion is present of a spectral steepening moving from the inner (spine) to the external jet region but at this high angular resolution the jet width is not well defined.

Average Nuclear Spectrum

It is interesting to consider the nuclear flux density over the whole range of frequency. We are aware that the compact core of Mkn 501 presents some variability (see §6.3.2); however, the large number of observations and frequencies available allow us to carry out such a study based on average values.

We plot in Fig. 6.12 the average core peak flux density, from the images at resolution of 0.6×0.9 mas (see Table 6.3); at 1.6 GHz, we had to consider super-resolved images, in order to avoid a large contamination from the jet. The spectrum is convex, peaking at ~ 8.4 GHz and steepening toward the high frequency end. Below the turnover frequency, the spectrum is flatter than $\alpha = 2.5$, as would be expected for a single self-absorbed component. This suggests that different components with different turnover frequencies may be blended together.

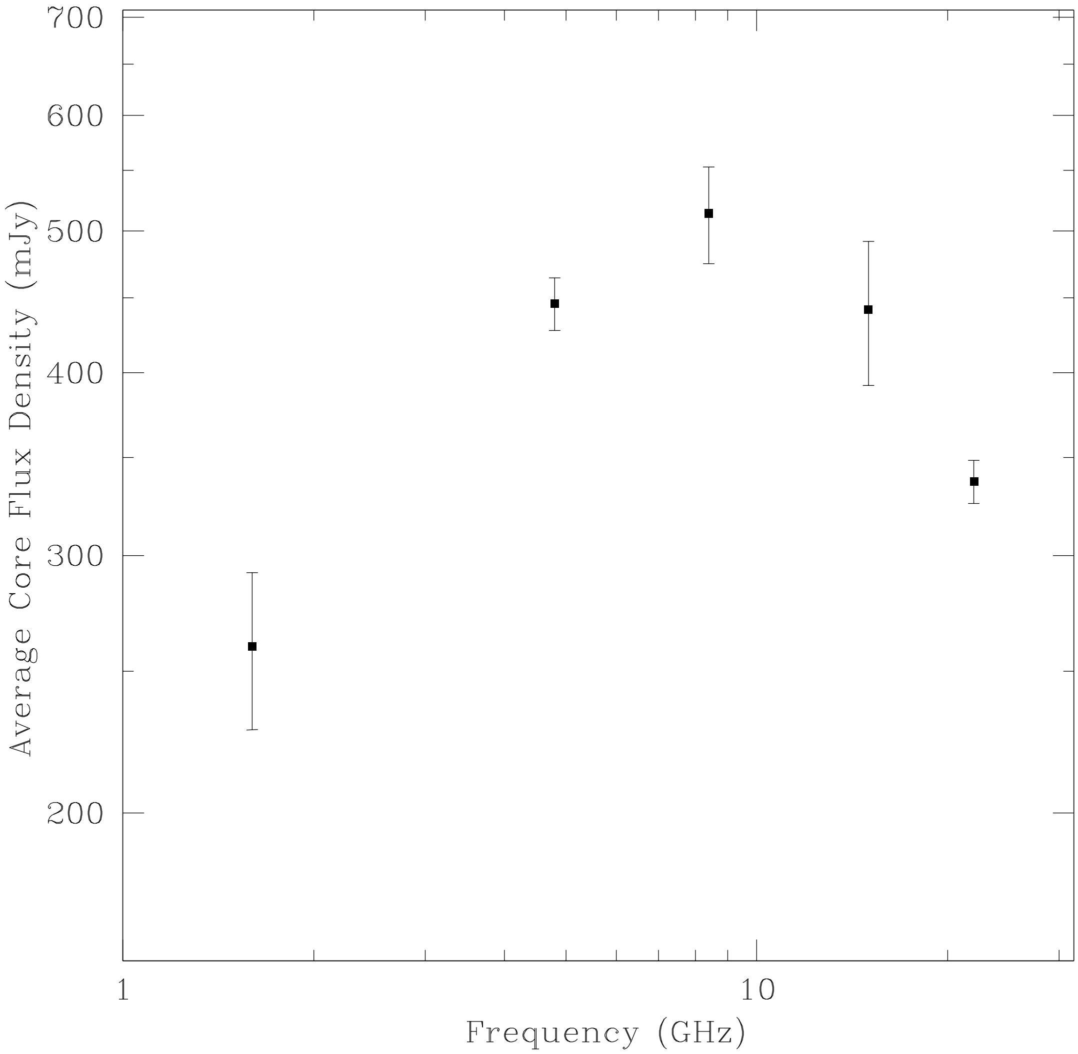

Figure 6.12 Average core spectrum from data at resolution 0.6×0.9 (HPBW, RA $\times$ Dec). Note the turnover at 8.4 GHz and the rapid decrease at higher frequency. The low frequency part presents a slow growth, suggesting the presence of more than one single self-absorbed component.

6.4 Discussion

6.4.1 Jet Velocity

Velocity Structure

Limb brightened jet morphology on parsec scales is present in some FR I sources but also in a few high power FR II sources (Giovannini, 2003). A possible explanation is the presence of velocity structure in the jet. When viewed at a relatively large angle to the line of sight, this structure yields different Doppler factors for the internal spine and the external shear layer. In particular, an inner high velocity spine could be de-boosted while a slower external layer could be less strongly de-boosted, or even boosted. Transverse jet velocity structure has been found by Laing et al. (1999, 2002a,b) in 3C 31, where the jet velocity in outer regions is ~ 0.7 the inner spine velocity. Chiaberge et al. (2000) invoke such a structure to account for observational discrepancies between FR I and BL-Lac objects.

A possible origin of the velocity structure is the interaction of the jet with the surrounding medium and its consequent entrainment; the mass loading slows down the jet in the external regions, while the inner spine travels unaffected. However, the presence of limb brightened jets in both high and low power sources (Giovannini, 2003) and the evidence in M87 that the jet structure is present very near to the core emission (see the image presented by Junor et al., 1999), suggest the possibility that the velocity structure may originate at the base of the jet. Meier (2003) presents a model where the inner high velocity spine is produced in the black hole region, while the external shear moving at lower velocity is produced in a more extended region downstream.

In Mkn 501, it is interesting to note that the jet structure is visible at a distance < 1 mas from the core, suggesting that it originates very close to the base of the jet. However, we recall that, at $z = 0.034$, 1 mas corresponds to ~ 0.7 pc, i.e., $> 10^4$ Schwarzschild radii (see Rieger & Mannheim, 2003, and references therein for a discussion on the central black hole mass in Mkn 501) and, therefore, we do not have the angular resolution to see this jet inner region. Nevertheless, we note that the presence of velocity structure so near to the nuclear source implies too strong a deceleration if it is completely due to the jet interaction with the ISM. We suggest (in agreement with M87 data of Junor et al., 1999) that a transverse

Table 6.6. Jet Velocity Structure - Parallel Magnetic Field

R_{core} (pc)	θ (°)	Γ_{spine}	δ_{spine}	Γ_{layer}	δ_{layer}	Notes
0.0001 – <0.03	4	15	15	?	?	γ-ray region
0.03 – 0.15	10	15	4	10	5	Radio core
0.15 – 7	15	15	2	3	5	First jet region
7 – 20	15–20	15	2–1	3	4–3	Before of large bending
20–30	25	10–3	1–2	2	2.5	After the large bending
50	25	1.25	1.8	1.1	1.5	Final VLBI jet region

Note. — R_{core} = projected distance from the core

Table 6.7. Jet Velocity Structure - Perpendicular Magnetic Field

R_{core} (pc)	θ (°)	Γ_{spine}	δ_{spine}	Γ_{layer}	δ_{layer}	Notes
0.0001 – <0.03	4	15	15	?	?	γ-ray region
0.03 – 0.15	10	15	4	10	5	Radio core
0.15 – 7	15	15	2	3	5	First jet region
7 – 20	15	15	2	3	4	Before of large bending
20–30	15	10	2.5	3	4	After the large bending
50	15	10	2.5	3	4	Final VLBI jet region

Note. — R_{core} = projected distance from the core

velocity gradient is intrinsic to the jet structure (as discussed by Meier, 2003) and that a further velocity decrease due to mass loading in the jet from the ISM is likely to be present and possibly dominates the jet velocity structure at larger distances from the core.

Bulk Motion and Jet Orientation

We have strong indications that in Mkn 501 the radio jet emission is oriented at a large angle with respect to the line of sight relative to that expected for a blazar:

- From the jet morphology: the jet is limb-brightened in high resolution images at ~ 1 mas from the core. The different brightness can be related to a different Doppler factor only with an orientation angle $\theta \gtrsim 15°$. Then, we can reproduce the observed ratio between the brightness of the external shear and the inner spine with $\Gamma_{spine} = 15$, assuming $\Gamma_{layer} \sim 3$ (see Tables 6.6,6.7). With these values, the spine Doppler factor (δ_{spine}) is lower than the external layer Doppler factor (δ_{layer}). On the contrary, a jet orientation at a smaller angle and/or a lower spine velocity imply $\delta_{spine} > \delta_{layer}$ and therefore a centrally peaked structure.

- From the core dominance: the core boosting is high but not extreme; high bulk velocities require, therefore, an orientation angle θ in the range 10°–27° with respect to the line of sight.

- From the fit to the trend of the jet brightness and FWHM: assuming an adiabatic model and consistency with the jet/counterjet brightness ratio, we need a radio jet starting with a high velocity ($\beta \sim 0.998$), and in the case of a parallel magnetic field, θ has to be $\sim 25°$ at > 70 mas.

These results seem to be in disagreement with constraints derived from the high frequency (γ-ray) emission and variability detected in blazars. Studying the rapid burst of TeV photons in Mkn 421, Salvati et al. (1998) determine that a jet with a bulk velocity $\Gamma \gtrsim 10$ with opening angle and orientation angle $\sim 1/\Gamma$ is required. Similarly, in Mkn 501 the expected Doppler factor should be $\gtrsim 10$, as obtained from fits of synchrotron self-Compton (SSC) models (Katarzyński et al., 2001; Tavecchio et al., 2001). To reconcile the radio and high frequency results we have to assume that the inner region of the jet (0.001–0.03 pc) is moving with a Lorentz factor $\gtrsim 10$ and oriented at $\theta \lesssim 5°$. From this region we have high energy radiation and negligible radio emission. Over the range from 0.03 to 50 pc (projected distance) the jet orientation has to change from $\sim 5°$ to 25° (or at least $\sim 15°$ in the case of perpendicular magnetic field).

We propose that this large change in the jet direction may be gradual and we derive the minimum change requested by observational data at different distances from the core. As shown in Table 6.6, a progressive change in the jet direction with respect to the line of sight is possible and in agreement with the observed pc-scale jet properties.

At present, there is no obvious explanation for this change in the jet direction in the inner region. It is possible that it could be related to helical type motion (Villata et al., 1999) (although helical motion is not visible in our high resolution images), or to an instability in the jet due to reasons that are thus far unknown. It is also important to stress that small changes in direction are not uncommon in FR I radio galaxies and are magnified when projection effects occur. In any case, we recall that beyond 30 mas from the core the jet position angle becomes stable and closely aligned with the kpc-scale structure.
We note that in the case of the perpendicular magnetic field the jet velocity is still very high at large distances from the core, in agreement with the lack of detection of a visible counterjet in all published maps of this source and despite the symmetric structure visible in the VLA low resolution image (Ulvestad et al., 1983). However, we recall that $\theta \gtrsim 15°$ is required to justify the observed limb-brightened structure from Doppler boosting alone, even in the case of perpendicular magnetic field.

6.4.2 Physical Parameters

From the present data we can derive that:

- The nuclear region shows a self-absorbed spectrum with a peak frequency $\nu_m \sim 8.4$ GHz and a peak flux density $S_m \sim 0.55$ Jy. Following Marscher (1987), we can use these data to estimate the magnetic field in the nuclear region (from 0.03 to 0.15 pc):

  $\mathrm{B} = 3.2 \times 10^{-5}\, \theta^4\, \nu_m^5\, S_m^{-2}\, \delta\, (1+z)^{-1}$;

  assuming θ (the core angular size) = 0.2 mas (0.15 pc) and $\delta = 5$ (Table 6.6), we estimate a magnetic field $\mathrm{B} \sim 0.03$ gauss. On the other hand, fits of SSC models to a high energy state observed in April 1997 yield values of the magnetic field in the range 0.2–0.02 gauss in the inner region (< 0.03 pc) (Katarzyński et al., 2001). This suggests a constant or a not very large decrease of the magnetic field from the gamma ray emitting region to the beginning of the radio jet.

- The radio spectra of jet sub-components show an evident steepening at high frequencies, suggesting the effect of radiative losses in a high magnetic field.

- In the region where the jet is well resolved, the spectrum is flat in the inner spine confirming the presence of a higher transport efficiency, lower radiative losses, or reacceleration mechanisms. The transverse steepening from the spine to the shear layer regions confirms the larger losses in these regions, probably related to the interaction with the external medium.

- It is not straightforward to determine the equipartition magnetic field (Pacholczyk, 1970) given the complex structure of the jet. We can obtain a rough estimate by assuming that electrons and heavy particles carry the same amount of energy ($K = 1$), the filling factor $\phi = 1$, and the frequency range is between 10 MHz and 100 GHz. This yields ~ 0.015 gauss in the C4 and C3 regions and 0.01 gauss in the C2 and C1 regions.

- Assuming a viewing angle θ as in Tables 6.6 and 6.7, the observed angular distances correspond to the following de-projected linear distances:

  – The inner limb-brightened region is present at < 4 pc from the core

  – The first jet region extends to ~ 10 mas, corresponding to ~ 30 pc

  – The VLBI jet is visible up to 170–270 pc (assuming $\theta = 25° - 15°$, respectively)

  – The kpc-scale structure is symmetric (i.e. not relativistic) at $\leq 20 - 30$ kpc from the core

  – The large scale symmetric structure extending to $\sim 70''$ corresponds to a linear size of 120–200 kpc, in agreement with the expected linear size of a FR I radio galaxy with the same low frequency total radio power.

6.5 Conclusions

As a result of the many frequencies and resolutions available, we have established that a limb-brightened structure is indeed present in Markarian 501, beginning in the very inner jet. This has important consequences: (1) it implies the presence of velocity structure already at very small scale, which jet models will have to take into account; (2) it suggests, together with other arguments, that the VLBI jet can not be oriented at too small a viewing angle. In particular, the detection of a very long one-sided jet and the results of an adiabatic expansion fit yield values of the angle of view in the range $15° < \theta < 25°$, depending also on the magnetic field orientation.

The bulk velocity is strongly relativistic at the beginning ($\Gamma \sim 15$), decreasing to $\beta \sim 0.6$ ($\Gamma \sim 1.25$) at the end of the VLBI jet, 100 mas from the core (parallel B) or to $\beta \sim 0.99$ ($\Gamma \sim 7$) in the case of a perpendicular B. The data considered here are consistent with a pattern speed of zero. Previous reports, based mostly on lower frequency observations, have reported low pattern speeds, however the complex limb-brightened structure revealed at 22 GHz makes measurement of component speeds problematic at high frequencies.

Finally, the study of the spectral indices has revealed a self-absorbed compact core and a complex spectral index distribution in the jet with flat and very steep regions. A clear connection is present between limb-brightening in total intensity and the spectral index images: the inner spine has a flat spectrum while the jet more external regions show steep spectra. Our derived magnetic field strengths are similar to those obtained from data at other wavelengths, yielding values of order $B \sim 0.03$ gauss in the core region. The estimated equipartition field in the jet region is in the range 0.015–0.01 gauss.

Chapter 7

Lobe Advance Velocities in the Compact Symmetric Object 4C 31.04

Extragalactic radio sources come in a variety of flavours. Spanning a range of almost ten orders of magnitude in radio luminosity, they exhibit compact or extended morphology, flat or steep spectra, and can be hosted by "normal" galaxies or associated to optically bright quasi stellar objects, presenting narrow, broad, or absent emission lines. In the previous chapters of the present thesis, we have explored an interesting framework, which attributes most differences to orientation, as a consequence of both obscuration and relativistic beaming. Although we have shown that this scheme is meeting with success, there is however growing evidence that age is also a key variable that needs to be added to the space of parameters, and that an evolutionary sequence may hold as well (Fanti et al., 1995; Polatidis & Conway, 2002); for example, recent observations have revealed a few objects presenting a self-similar morphology, which can be interpreted as a signature of restarted activity Lara et al. (2002).

On the smallest scale, Very Long Baseline Interferometry (VLBI) are able to probe the parsec scale structure of compact objects, separating sources strongly affected by beaming (asymmetric, core dominated, flat spectrum) from those lying in the plane of the sky (often symmetric, with faint cores). Among the former we find, e.g., BL Lacs: intrinsically large objects whose compactness is only apparent; the latter are named Compact Symmetric Objects (CSOs) after their morphology: they have sub-galactic dimensions but the same symmetric, two-sided aspect as classical large scale FR I and FR II radio galaxies. In them, we observe all the typical components of a

full size radio galaxy (core, jet/s, lobes and hot spots) on a thousand times smaller scale. Whether the small size were due to an extremely dense medium surrounding the radio source (frustration scenario) or simply to a young age (youth scenario) has longly been debated (Fanti et al., 1995; Readhead et al., 1996a,b). Evidence of hot spot advance on time baselines of a few years have solved this dilemma, showing and providing age estimates of order $10^2 - 10^4$ yrs (Owsianik & Conway, 1998; Polatidis & Conway, 2002). Support to this scenario comes also from multi-frequency studies of spectral ages (Murgia et al., 1999), as well as from the lack of any evidence for the presence of the dense interstellar medium (ISM) needed by the alternative frustration scenario. The overall radio spectra of CSOs are typically convex, peaking at frequencies that present an anticorrelation with the source size. This behaviour is modeled in terms of synchrotron self-absorption of the radiation emitted by the radio source. By going from smaller to larger sources, we then find High Frequency Peakers, Gigahertz Peaked Spectrum and Compact Steep Spectrum sources (Dallacasa, 2003).
Among other properties of CSOs in the radio, we remind that (1) the rate of H I absorption is higher than in common radio galaxies (e.g. van Gorkom et al., 1989; Pihlström, 2001), and (2) variability and polarization are almost non-existent (Fassnacht & Taylor, 2001). At other wavelengths a comprehensive study of the properties of CSO host galaxies is still missing, although HST observations have suggested that in at least some cases the host galaxies are not completely relaxed (Perlman et al., 2001).

7.1 Introduction

For all the reasons stated in the previous section, considerable efforts have been devoted to the study of CSOs in recent years. Among other sources, the radio galaxy 4C 31.04 (B2 0116+31) was observed with VLBI by Wrobel & Simon (1986) at 92 cm using 7 antennas. Their image showed two components separated by about 70 mas. Cotton et al. (1995) tentatively classified this source as a low redshift ($z = 0.0592$) CSO. Giovannini et al. (2001) confirmed the CSO structure and identified the core with a weak flat spectrum central component.
On the basis of spectral line VLBI observations, Conway (1996, 1999) has presented evidence for a circumnuclear H I disk, viewed close to edge-on, whose axis is that

of the radio jet. The presence of a circumnuclear disk is also supported by HST observations (Perlman et al., 2001), which reveal a disk-like dusty feature of somewhat larger scale but similar orientation to the one suggested by Conway. The optical nucleus is also found to have cone-like features well aligned with the radio axis.

After a five year gap following the first observation at 5 GHz presented in Giovannini et al. (2001), we re-observed this source with the VLBA in order to look for a possible expansion. We will report on the milliarcsecond scale morphology and perform model-fitting and other analysis of the data (brightness profile, difference map). We will use the measured velocity of the expansion to estimate the kinematic age of the source. We also study the spectral index considering VLBA observations at 1.3 GHz and MERLIN at 22 GHz and derive the spectral age. Finally, we will discuss and compare the two estimates.

7.2 Observations

7.2.1 5 GHz Observations

The first epoch observations at 5 GHz were obtained on July 22, 1995 (1995.554), with the Very Long Baseline Array plus a single VLA antenna (Y1) for ∼5 hours. Details about these observations are discussed in Appendix A of Giovannini et al. (2001).

In the second epoch we obtained ∼10 hrs of observing time with the full VLBA + Y1 in full polarization mode on July 3, 2000 (2000.504). The observing frequency was centered at 4.971 GHz with 4 IFs and both polarizations recorded. Correlation was performed in Socorro. All calibration and fringe fitting were done within NRAO Astronomical Image Processing System (AIPS): J0136+4751 was used as an amplitude and leakage term calibrator, while J1751+0939, 3C395 and J0423−1020 were used as calibrators for the polarization angle.

For the purposes of this work it was important to have both datasets reduced in the same way. Thus we reanalyzed first epoch data, in order to have the same calibration procedure for both observations. We then exported the two datasets to Difmap, which we used to perform the editing, self calibration and model-fitting. To properly register the two images, we used the 1995.554 image as a starting model for the self calibration of the 2000.504 data. We chose a restoring beam of 3 mas

FWHM for both epochs.

7.2.2 1.3 GHz and 22 GHz Observations

It is of great interest to compare the dynamic age – derived from the study of hot spot velocities, to the radiative age – which can be estimated from synchrotron losses. In order to make this comparison, observations at multiple wavelengths are needed.

Data at 1340 MHz were obtained with the VLBA + Y1 on July 7, 1995 in a project aimed to study the nature of H I absorption in CSOs. Spectral line results and a continuum map with angular resolution of 3 mas (FWHM) were reported in Conway (1996). Details on data calibration and reduction will be presented in a forthcoming paper (Conway et al., in prep.). Here we point out only that the same strategy used for the 5 GHz data was adopted.

We also investigated the high energy end of the spectrum by considering a MERLIN observation at 22 GHz. Observations were made on 29th January 1998 in continuum mode with a bandwidth of 14 MHz, using all 5 of the MERLIN telescopes available at this frequency. The observations lasted 12 hrs. Observations were made using phase-referencing, but only low dynamic range images were obtained using phase-referencing so final images were made using self-calibration. Good fits to the phase and amplitude data were obtained. Final restoring beam was 10 mas (FWHM).

We used the 1.3 GHz data and the second epoch 5 GHz observation to map the spectral index. For a proper comparison we tried to achieve a similar (u, v) coverage at the two observing frequencies by cutting the shortest baselines in the 20 cm data and the longest ones in the 6 cm data. Final images were then produced with the same angular resolution and cell–size. The source position in the two images was registered using the isolated, unresolved core.

The resulting (u, v) coverages at 5 and 22 GHz are quite different, so it was not practical to produce a spectral index image between these frequencies. However, comparable short baselines are present, so that we do not expect missing flux in either image. This allowed us to derive an integrated spectrum for different regions of the source.

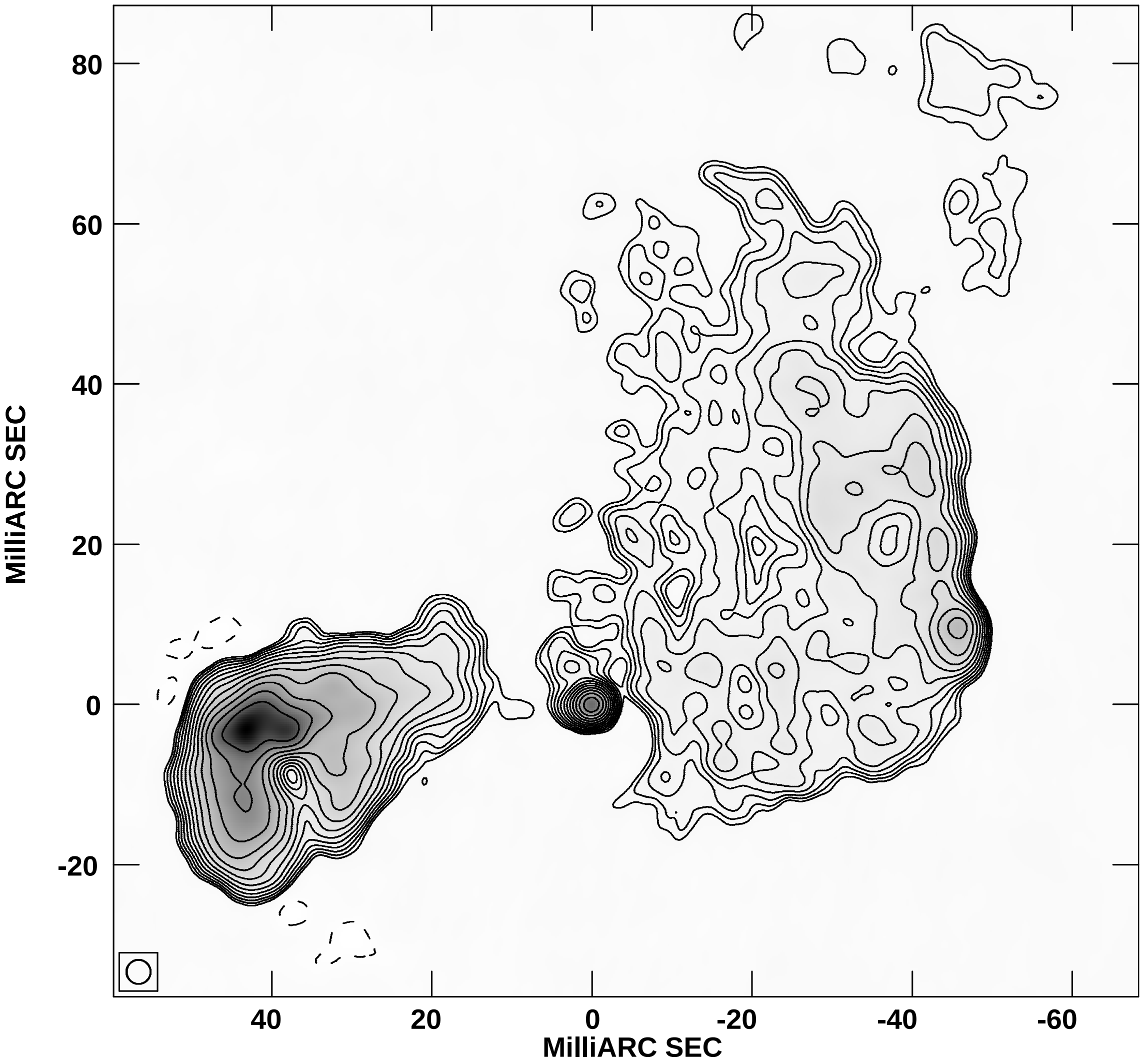

Figure 7.1 The July 2000 VLBA image of 4C 31.04 at 5 GHz. Contours are drawn at -0.4, 0.4, 0.57, 0.8, ..., 36.2 mJy/beam by $\sqrt{2}$ intervals with negative contours shown dashed. The peak flux density is 40.2 mJy/beam. The grey scale range is from -0.75 to 40.2 mJy/beam. Note the compact core, symmetrically placed hot spots, and the unusual 'hole' in the eastern lobe.

7.3 Results

7.3.1 Morphology

In Figure 7.1 we show the final image of 4C 31.04 at 5 GHz for the July 2000 epoch, convolved with a circular restoring beam of 3 mas (FWHM)[1]. The overall structure of the source is the same as was observed in 1995 (both at 5 and 1.3 GHz), consisting of a compact core component with hot spots and lobes on either side. The lower

[1]Assuming $H_0 = 65$ km s^{-1} Mpc^{-1} and $q_0 = 0.5$, at the distance of 4C 31.04 ($z = 0.0592$) 1 mas corresponds to 1.2 pc and 1 mas/yr = 3.9 c.

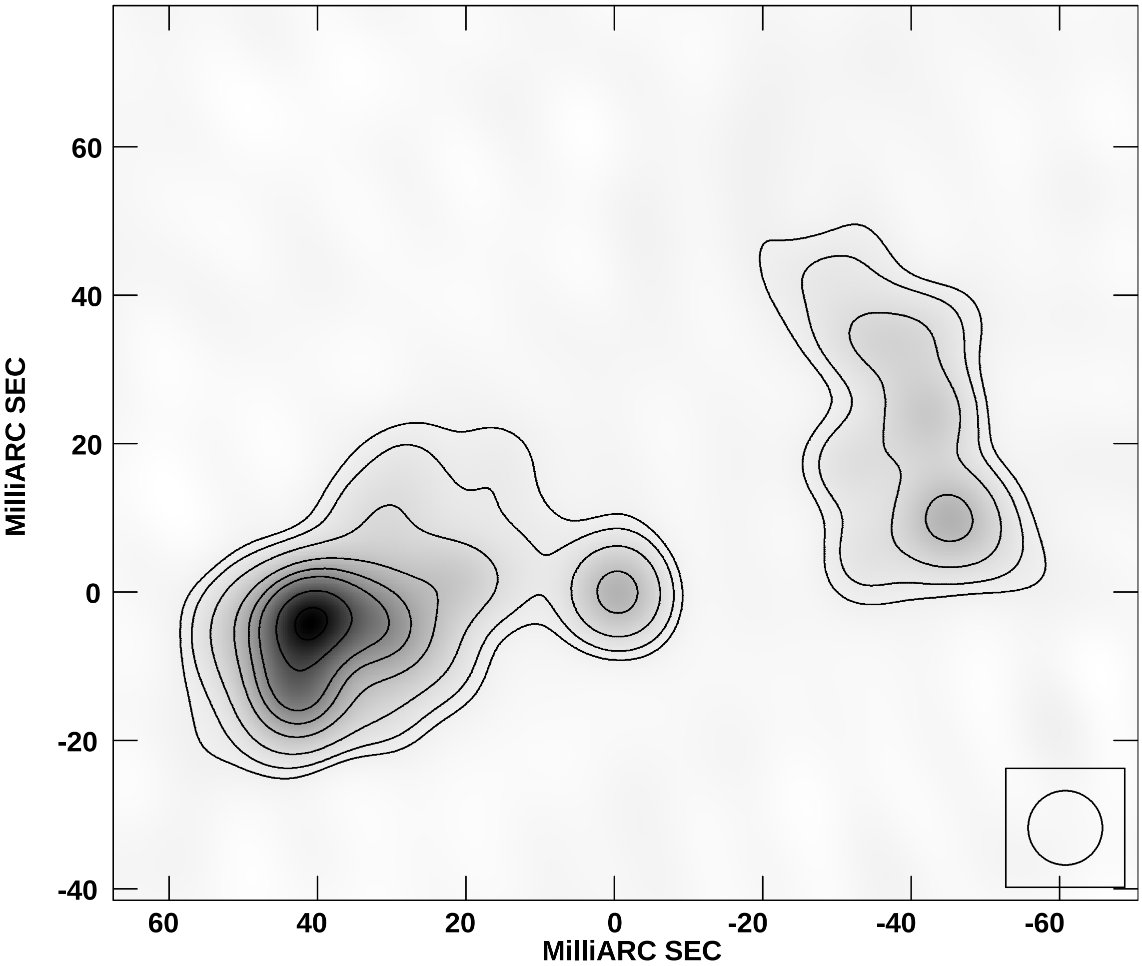

Figure 7.2 MERLIN image at 22 GHz restored with 10 mas FWHM. Contours are drawn at −4, 4, 8, 16 32, 48, 64, 96, 128 mJy/beam. The peak flux density is 138.5 mJy/beam. The grey scale range is from −4.3 to 138.5 mJy/beam.

resolution (10 mas FWHM) 22 GHz MERLIN image shown in Fig. 7.2 shows the same features, except that the lobes look much fainter and are barely detected.

At all frequencies the total source extent is ∼100 mas, which corresponds to ∼120 pc. Total flux density in the 5 GHz maps is ∼ 1.25 Jy, i.e. about 90% of values measured with single dish telescopes (Becker, White, & Edwards, 1991; Gregory & Condon, 1991). This yields a total power of 1.14×10^{25} W/Hz at 5 GHz, which makes 4C 31.04 one of the weakest known CSOs (Polatidis, 2002).

Within Difmap, we model-fit the visibility data of the two 5 GHz observations with a set of 10 elliptical Gaussian components. We used large, extended components in order to pick up the lobes' flux density as well as compact components to describe the core and hot spots. We fixed the parameters of the largest components (size >

10 mas) and let the most compact ones vary; results of the fits are listed in Table 7.1. Uncertainties for each component are computed from the ratio between its FWHM and SNR and are all within 0.1 mas. The most compact components, except for the core, are all located in the hot spots regions. The western hot spot is labeled W1, while the best fit to the eastern end is obtained using three different components – E1, E2 (also the image peak of 40.2 mJy/beam) and E3. Given their high brightness, position close to the edge of the lobe and compactness, we will consider W1 and E2 as the two primary hot spots of this source. It is less likely that either E1 or E3 – both quite fainter than E2 – may be a primary hot spot; it is however possible that they are secondary hot spots similar to those found in many extended FR II sources. The innermost E3 could also be related to the presence of a knot component in an underlying jet.

Indeed, even if a classical jet of plasma is not detected, hints of a jet-like feature are clearly present in the enhanced brightness visible all along the line connecting the core, and in the east hot spot which has an elongated structure on the west side in the full resolution image published in Giovannini et al. (2001). Here it is suggested that the source is oriented close to the plane of sky ($\theta > 75°$), with the west lobe the one nearest to us, in agreement with Conway (1996).

With the increased image fidelity obtained in this second epoch we can also confirm the presence of a 'hole' in the east lobe. This large region of lesser brightness lies close to the east hot spot, in a direction perpendicular to the jet. While visible in the first observation, it looks even dimmer and more defined in this second epoch. In contrast, the west lobe does not present very clear features. Being very extended and of low brightness, it cannot be mapped with high fidelity by VLBI technique; however, we are confident that this does not affect the compact hot spot region, which is well detected on most baselines. Fig. 7.2 and the 1.3 GHz data (Conway, 1996) also confirm that it is indeed a compact, flat-spectrum component.

At their outermost extents, both lobes have a very sharp edge, running along a very wide front ($\sim$ 20 mas in the eastern lobe but even $\sim$ 40 mas in the western one). The sharpness of this border is again in agreement with this region being the place where the plasma is advancing into the external medium as the source grows.

Table 7.1. Gaussian model and relative proper motions for components in 4C 31.04.

Comp.	Epoch	S (Jy)	r (mas)	θ (°)	a (mas)	b/a	Φ (°)	Δr (mas)	v (h_{65}^{-1} c)	p.a. (°)
C...	1995.554	0.020	0.0	0.0	0.81	1.00	8.0			
	2000.504	0.024	0.0	0.0	0.81	1.00	8.0	reference		
E1...	1995.554	0.013	46.74	93.7	1.60	1.00	32.5			
	2000.504	0.013	46.82	93.9	1.60	1.00	32.5	0.18 ± 0.01	0.14 ± 0.01	157.6
E2...	1995.554	0.137	42.52	93.6	7.20	0.60	−28.3			
	2000.504	0.135	42.82	93.5	7.20	0.60	−28.3	0.31 ± 0.04	0.25 ± 0.04	79.6
E3...	1995.554	0.038	37.30	94.6	2.95	1.00	−6.0			
	2000.504	0.040	38.01	94.9	2.95	1.00	−6.0	0.74 ± 0.02	0.58 ± 0.02	110.2
W1...	1995.554	0.030	46.08	−78.3	5.54	0.53	7.0			
	2000.504	0.027	46.62	−78.3	5.54	0.53	7.0	0.54 ± 0.07	0.43 ± 0.07	-78.2
E4...	1995.554	0.213	45.67	106.0	11.53	0.69	11.7			
	2000.504	0.216	45.67	106.0	11.53	0.69	11.7	fixed		
E5...	1995.554	0.074	32.59	105.4	10.20	0.58	−0.9			
	2000.504	0.071	32.59	105.4	10.20	0.58	−0.9	fixed		
E6...	1995.554	0.209	33.89	89.4	20.32	0.40	−83.2			
	2000.504	0.229	33.89	89.4	20.32	0.40	−83.2	fixed		
W2...	1995.554	0.333	45.07	−50.1	41.63	0.42	22.8			
	2000.504	0.323	45.07	−50.1	41.63	0.42	22.8	fixed		
W3...	1995.554	0.143	21.91	−77.0	35.69	0.63	86.2			
	2000.504	0.162	21.91	−77.0	35.69	0.63	86.2	fixed		

Note. — Parameters of each Gaussian component of the model brightness distribution: S, flux density; r, θ, polar coordinates of the center of the component relative to an arbitrary origin, with polar angle measured from north through east; a, b, major and minor axes of the FWHM contour; Φ, position angle of the major axis measured from north through east; Δr, relative proper motion of the component; v, relative projected velocity in units of $h_{65}^{-1}\,c$ (h_{65} = H$_0$/65 km s^{-1} Mpc^{-1}), along the given position angle (p.a.).

7.3.2 Component Motions and Kinematic Age

The first hot spot velocities in CSOs by Owsianik & Conway (1998) required time baselines of $\sim$ 15 years, with VLBI observations at 5 GHz. By going to higher frequencies (15 and 43 GHz), Taylor et al. (2000) reduced this to $\sim$ 5 years for a few strong CSOs. Currently 10 sources have been measured (Polatidis, 2002). Typical velocities are $0.2h_{100}^{-1}\,c$ (i.e. $0.31h_{65}^{-1}\,c$), which due to the large distance of the sources, translates into angular motions of typically only a small fraction of mas/yr ($\sim$32 μas/yr at $z = 0.1$), thus requiring long time intervals and high angular resolutions. We consider observations at 5 GHz separated by 5 years. More observations in the future are planned to extend the time baseline and to better constrain the results.

To measure the advance velocity in 4C 31.04, we compare the model-fit of the dataset in our two epochs. Fig. 7.3 illustrates the motion of all the compact components with arrows of length proportional to the magnitude of their motion. It is apparent that all the components have moved away from the core. In particular, the two hot spots W1 and E2 show motions almost in the same direction as their position angles. Furthermore, the increase in hot spots separation becomes even more clearly visible when E2 and W1 are directly compared. In Fig. 7.4 we show a magnified inset around the west hot spot region with contours drawn for both epochs. In this image the 2000.504 profile has been shifted by 0.3 mas westward, so that the position of component E2 is the same in both maps (the displacement needed in declination is smaller than the measurement errors). The motion of the peak of W1 is clear, confirming the results of model-fitting.

In Fig. 7.5 we show a brightness profile made in AIPS with the task `SLICE`. The two profiles are derived from the two epochs along the same slice. This slice cuts the two hot spots at a position angle of $-82.6°$ (measured north to east), passing close to the core (but not across the core itself because of a small bend in the jet). In the global profile one can easily see the two lobes on the opposite sides (the east one being the brightest) and the core region in the middle (see Sect. 7.3.5 about core variability). The hot spot regions are magnified in the two insets, showing that both in the eastern and the western hot spot the 2000.504 profile is shifted outward. This displacement, though small, is clear both in the rising and in the falling part of the profile. We remind the reader that the region between the core and the west hot spot is poorly imaged, so that the features present in the slices in this region

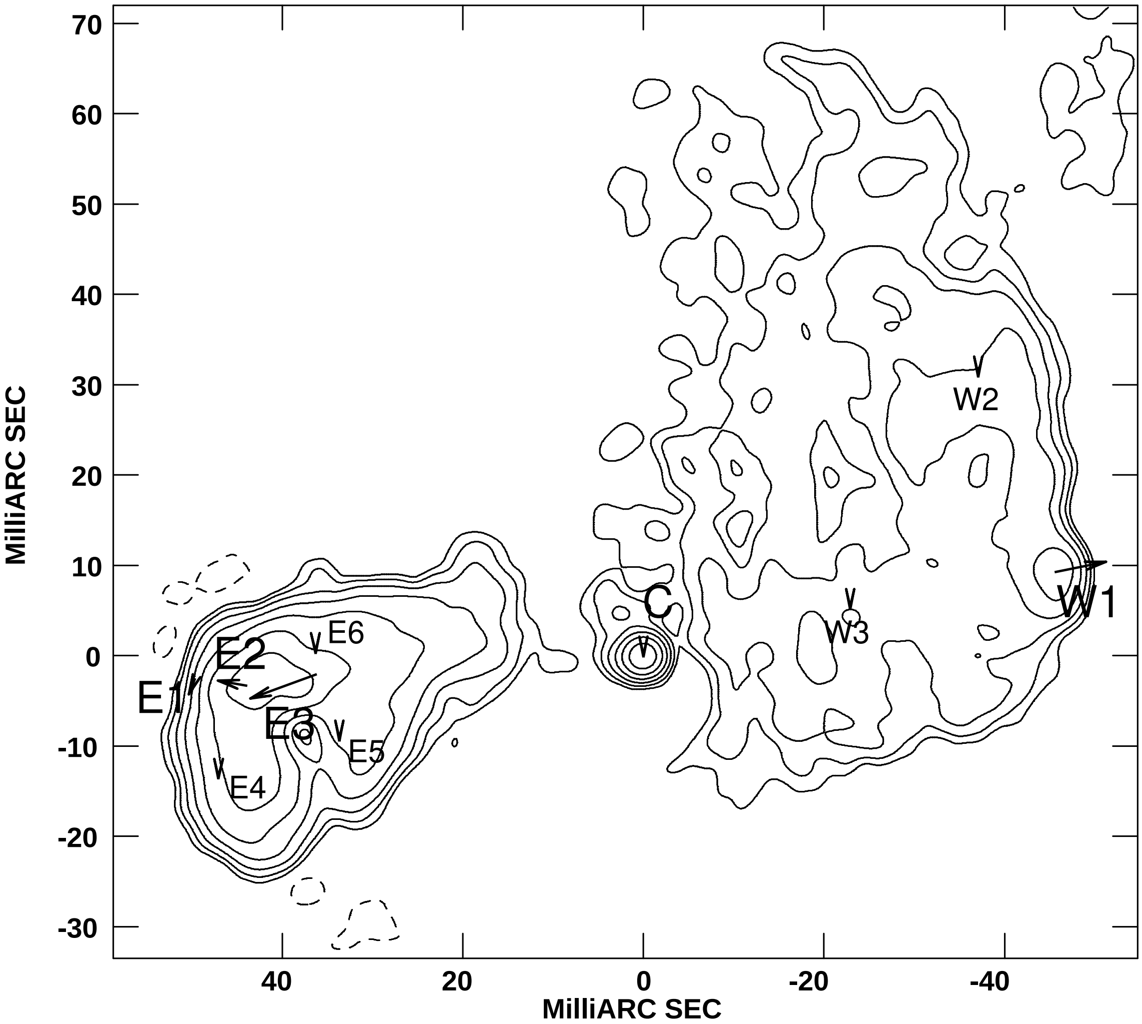

Figure 7.3 The 2000 VLBA image of 4C 31.04 at 5 GHz with arrows indicating the positions and motions of components derived from model-fitting. The model-fit results are shown in Table 7.1. Components larger than 10 mas have been held fixed between the two epochs for reasons discussed in the text. Component motions have been magnified by a factor of 5 for illustration purposes. Those arrows pointing due south indicate that the component was held fixed.

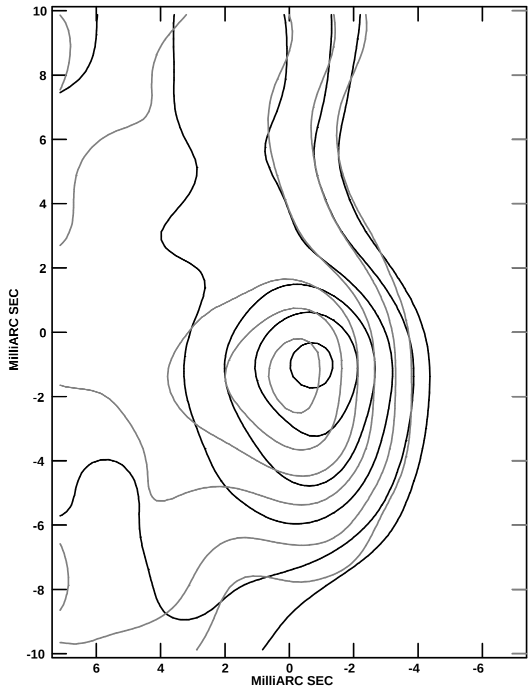

Figure 7.4 Overlay of the hot spot region in the west lobe (W1). Contours are drawn in grey (epoch 1995.554) and black (epoch 2000.504) at (1, 2, 4, 6, 8, 10) mJy/beam. The two images have been aligned on the position of the east hot spot E2.

are not completely reliable. It is also possible that some of the changes are due to turbulence present in this back-flow region.

The increase in the hot spot separation implies an expansion of the whole source. Since the lobes are too extended and faint to measure their expansion by model-fitting, we tried to directly compare the two images. The difference map shown in Fig. 7.6 was done with the AIPS task `COMB`. The features that appear in this image, in particular in the eastern lobe, are clearly related to the expansion of the source. The two close white and black spots are due to the outward shift of the peak of component E3. Moreover, the presence of a white stripe all around the outer edge of the lobe, though faint, is suggestive of an expansion of the whole eastern lobe in this direction. Note that a similar white stripe, even if less evident, is present all around the edge of the west lobe.

As these last results (shown by Fig. 7.4, 7.5, 7.6) are drawn from the images and not from the model, we feel that they lend support to the detection of motion and to the estimate of its velocity derived from the model-fits. With just two epochs available, and a moderately short time baseline, it is difficult to better quantify the accuracy of our measurements of component motions. We hope to address this difficulty with

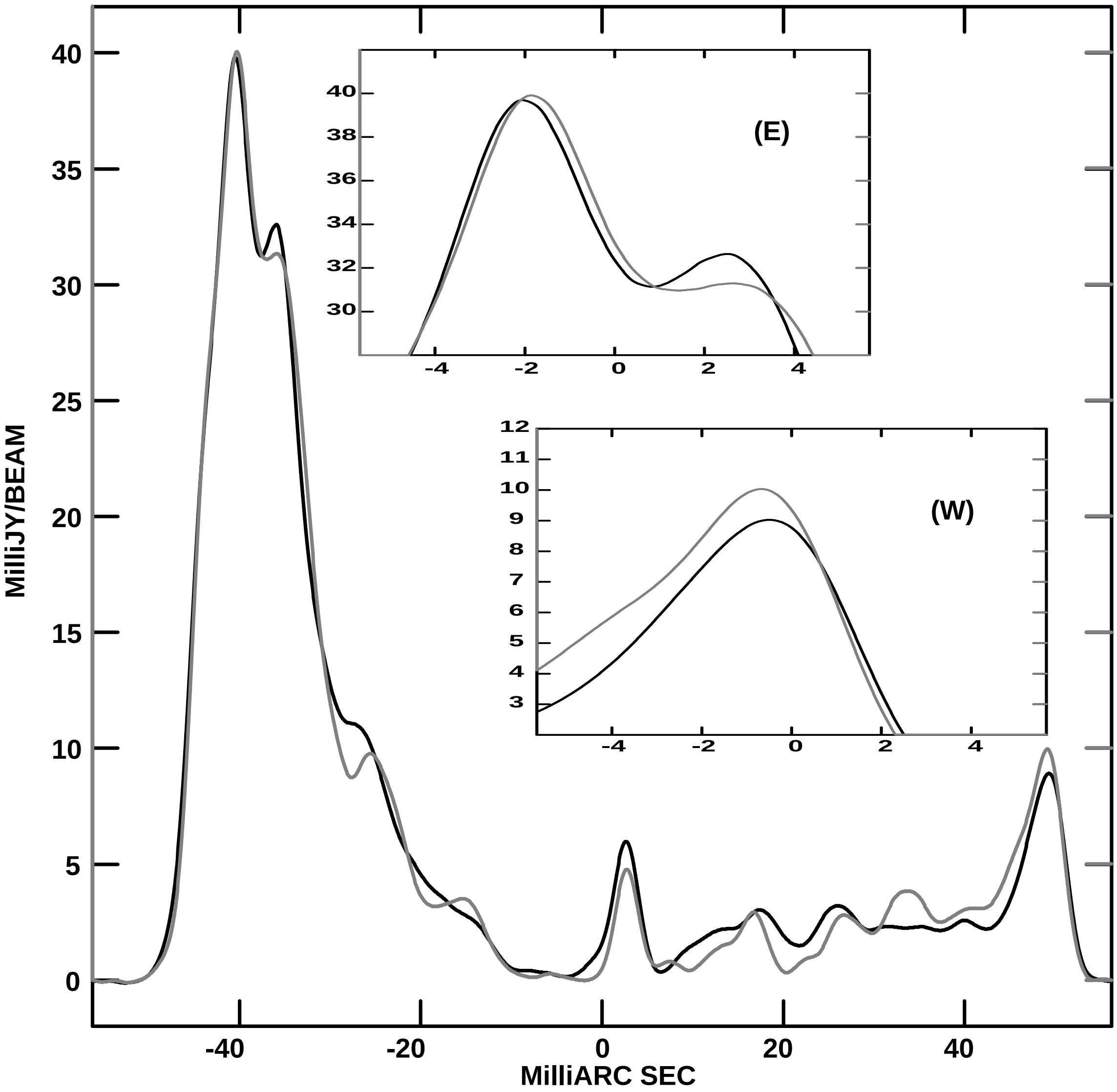

Figure 7.5 A slice through the hot spots of 4C 31.04. The central small peak results from the northern edge of the core (the hot spots are not perfectly symmetric about the core). The black line shows the profile of the 2000.504 image, while the grey line represents the profile of the 1995.554 image. Shown inset are magnified versions of the profile at the east (E) and west (W) hot spots.

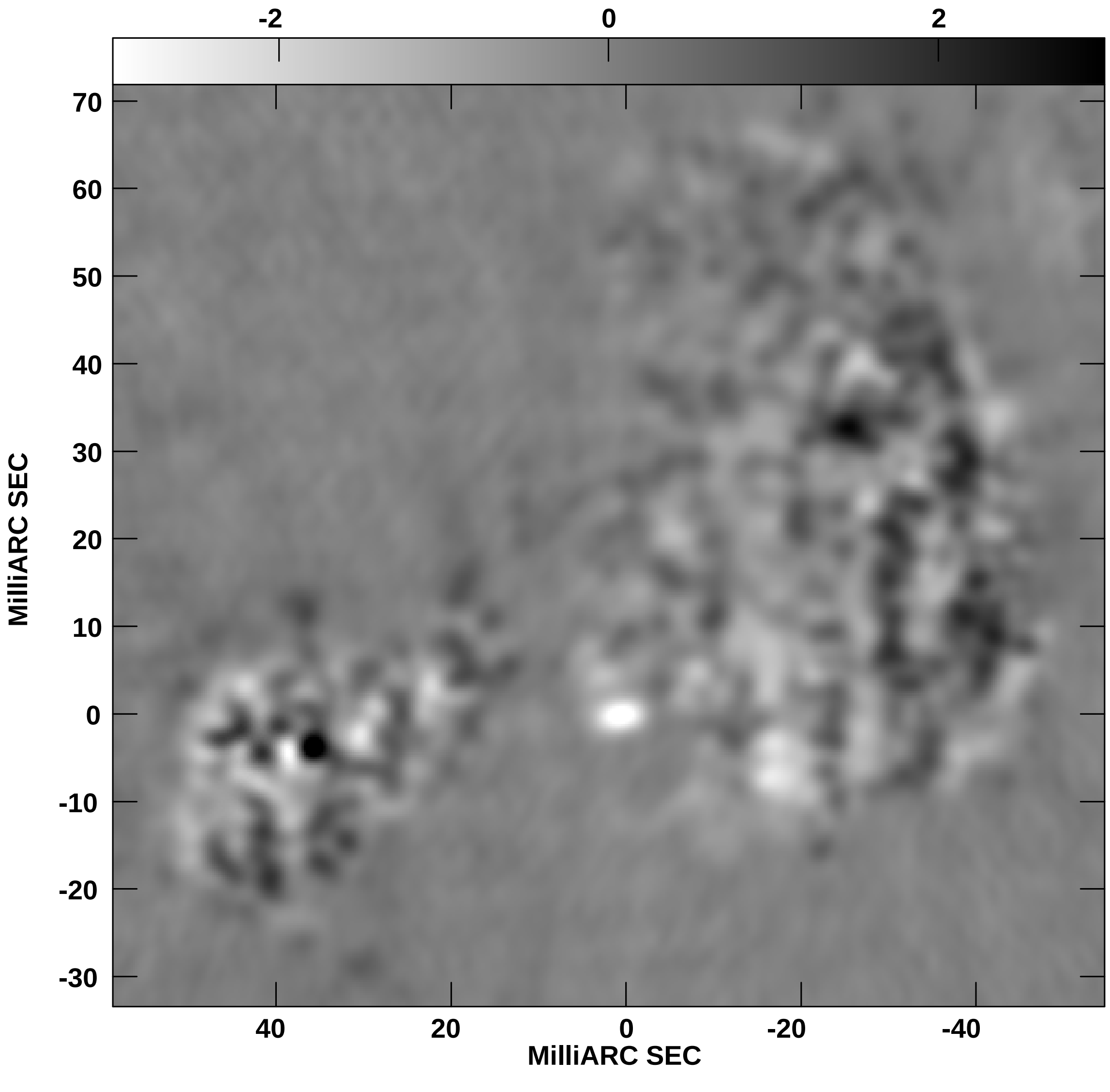

Figure 7.6 The difference image computed as $S_{2000.504} - S_{1995.554}$. Note the change in the core flux density of ~4 mJy. One can also see the black+white pattern of motion in the eastern hot spot, and a faint ring of white along the edge of the eastern lobe. The "mottled" pattern in the lobes is a result of the low fidelity of the image in the presence of extended emission.

future observations.

Model-fitting of the present data (see Table 7.1) provides the most reliable information on the velocity. The east and west hot spots present quite different displacements, ΔW1 = (0.54 $\pm$ 0.07) mas and ΔE2 = (0.31 $\pm$ 0.04) mas. It is possible that such differences may be due to a velocity asymmetry related to an inhomogeneous ISM, but it is not possible to discuss it more deeply with only a two epoch measurement. Since the two arms are about the same length and the source is near to the plane of sky, we will assume that the average velocity over the long term is the same in both directions.

We therefore try to estimate the advance speed by averaging up the results for the two hot spots W1 and E2. This yields an average motion of (0.42 $\pm$ 0.08) mas in 5 years. This indicates that each hot spot is advancing at (0.085 $\pm$ 0.016) mas/yr, i.e. (0.33 $\pm$ 0.06) $h_{65}^{-1}\,c$. The most distant component (W1) is located 46.62 mas from the core, so it would have taken 548 $\pm$ 100 years to cover this distance at such speed. Therefore, based on kinematics, we can estimate the source age at $\sim$ 550 years.

7.3.3 Spectral Index Distribution and Spectral Age

From the measured energy distribution of a population of electrons it is possible – under a few basic assumptions – to determine how long these electrons have been radiating. This has proved to be a useful tool in estimating ages of compact radio sources (e.g. Murgia et al., 1999; Readhead et al., 1996a). In order to perform such a study, one needs to know the spectral index distribution and the magnetic field in the source.

The image in Fig. 7.7 shows the spectral index for 4C 31.04 between 1.3 and 4.8 GHz at a resolution of 3.0 mas (FWHM). The core spectrum is inverted[2] ($\alpha = -0.6 \pm 0.05$). This is probably due to self-absorption, even after accounting for possible flux density variability (see Sect. 7.3.5). In the east lobe, the hot spot region shows a flat spectrum ($\alpha \sim 0.1 \pm 0.01$) with a constant and uniform steepening toward the core direction, up to $\alpha \sim 1.0$ ($\pm$ 0.02) at 20 mas from the core, just before the 'gap' between the core and lobe. The spectral index distribution is more complicated in the west lobe perhaps on account of a stronger interaction of

[2]Spectral index is defined according to $S(\nu) \propto \nu^{-\alpha}$.

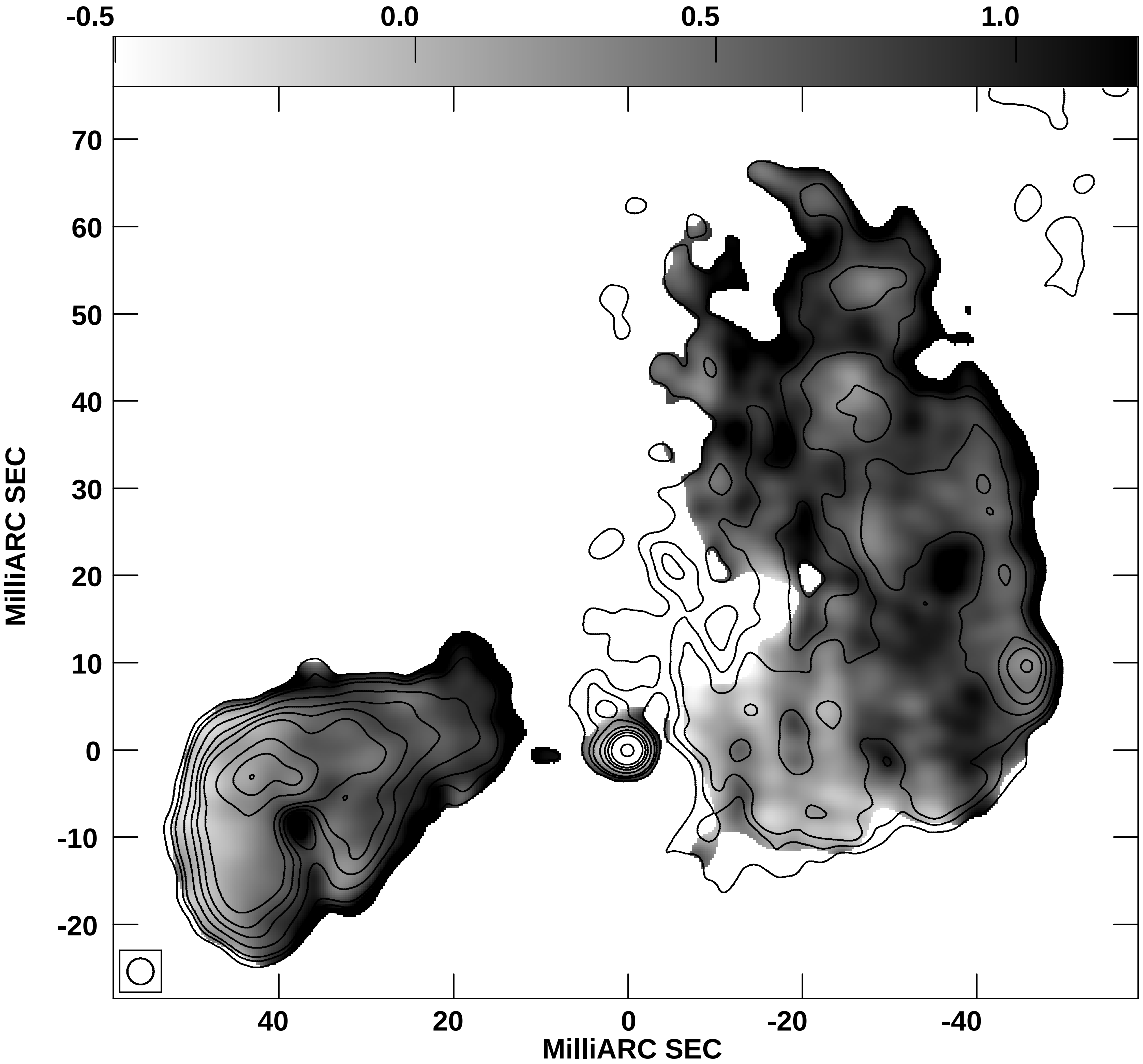

Figure 7.7 The spectral index map of 4C 31.04 at 3 mas resolution (FWHM). The grey scale range is −0.5 to 1.2. Overlaid contours from 4.8 GHz are drawn at 0.5, 1, 1.5, 3, 5, 7, 10, 20, 30, 40 mJy/beam.

the radio plasma with the ISM, as suggested also by the lobe morphology (see Sect. 7.4.2). The region of the faint hot spot is still flat ($\alpha \sim 0.25 \pm 0.01$) but the spectral index steepening is more irregular moving toward the core and to the north. The steepest values in the more external northern regions are as high as 1.0-1.2. In the core-hot spot direction the region from 10 to 30 mas shows again a flat spectrum (0.1-0.4) suggesting a local interaction between radio plasma and the dense ISM. Imaging problems in this low brightness region could also play a role.

In this high resolution image, one can see the region of the hole close to the east hot spot. The spectral index is very steep here, not only in the deep hole itself – where it is as steep as 1.7 $\pm$ 0.04 – but also in external lobe region, where we find $\alpha = 1.0$ $\pm$ 0.04.

In a population of electrons with an initial power-law energy distribution, synchrotron losses produce a curvature in the original straight power-law radio spectrum. The curvature manifests itself at a critical frequency related to the electron age. The shape of the spectrum and the critical frequency crucially depend on the evolution of the electron pitch angle distribution with time (Pacholczyk, 1970). We used the Jaffe-Perola model which assumes a redistribution of electron pitch angles on time scales short compared with their radiative lifetimes (Jaffe & Perola, 1973). To derive the critical frequency from the spectral index information, we used the Synage program (Murgia & Fanti, 1996). Since a spectral age measurement can give only the time since electrons were accelerated, we avoided the core and hot spot regions where local turbulence and electron re-acceleration is likely to be present, and investigated the steep-spectrum, relaxed regions where the 'oldest' electrons are present. The break frequency was found to be ~7.4 GHz in the east lobe at ~20 mas from the core, and between 6.1 and 7.2 GHz in the northern region of the west lobe.

The MERLIN image in Fig. 7.2 lends strong support to this estimate, showing that very little of the lobe emission is detected at 22 GHz. This cannot be due to a lack of short spacings since the MERLIN has baselines down to 6 km. It follows that the lobes are undetectable because of spectral steepening. Fig. 7.8 shows the spectrum for the two hot spots, the lobes and the core. The steepening between 5 and 22 GHz in the lobes supports the presence of a spectral break around 5-7 GHz.

The local magnetic field, which is also needed to derive the lifetime of radiating

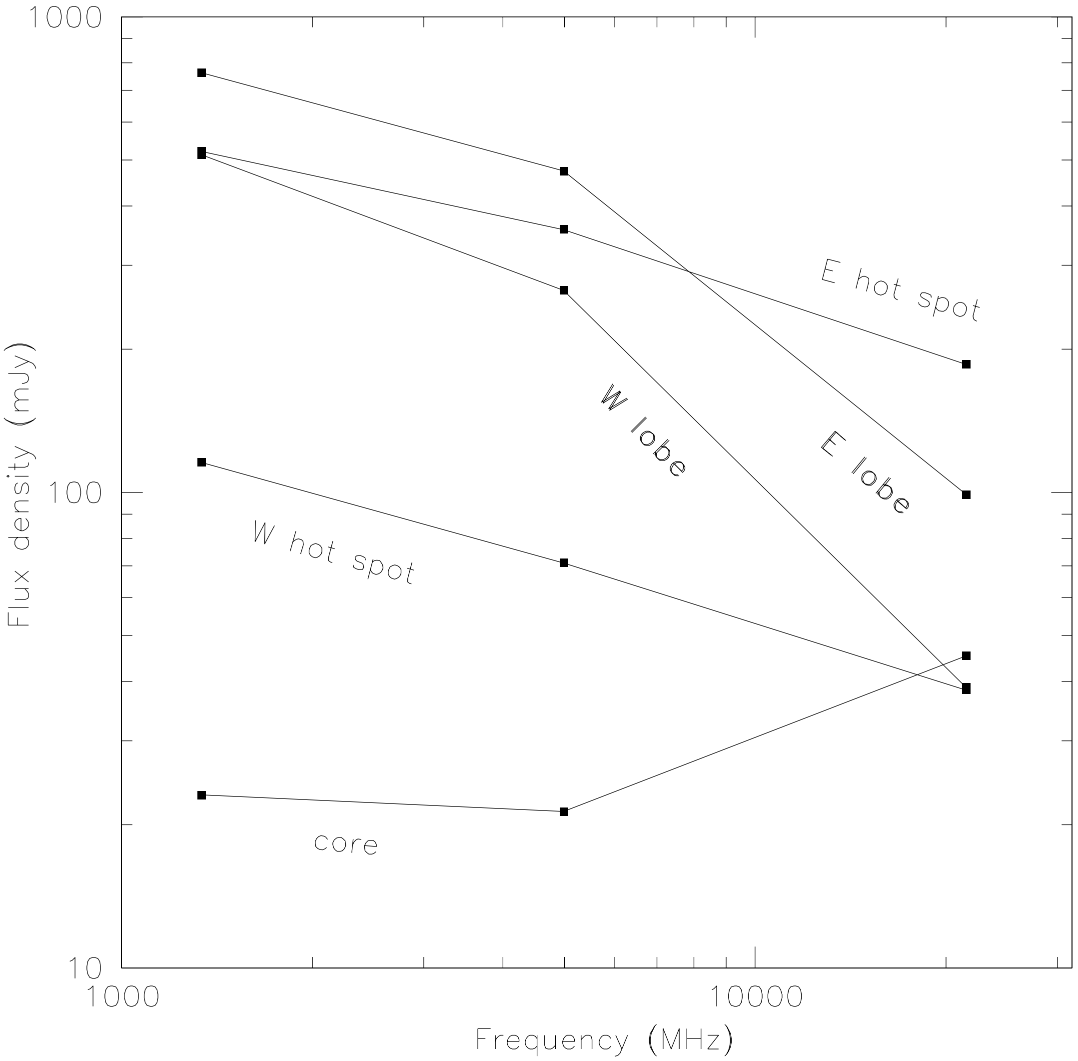

Figure 7.8 The spectrum of lobes, hot spots and core. The steepening of both lobes is clearly visible above 5 GHz.

electrons, was calculated assuming equipartition. We note that a recent X-ray study of a relatively compact FR II radio source (Brunetti et al., 2001) indicates that the magnetic field in the radio lobes is very near equipartition; equipartition conditions in GPS are also preferred by Snellen & Schilizzi (2002). Standard formulae (Pacholczyk, 1970) were used under the assumption that relativistic particles and magnetic fields occupy the same volume ($\phi = 1$), and that the amount of energy in heavy particles is the same as that in electrons ($k = 1$). We assumed cutoffs in the relativistic particle energies at 10 MHz and 100 GHz. The major uncertainty in the estimation of the equipartition field strength comes from the assumption of the source depth which we assumed to be equal to the smaller transverse dimension of the lobe regions where we estimated the magnetic field.

With these assumptions the derived equipartition magnetic field is 4.1 milligauss in the east hot spot region, decreasing to 3.3 milligauss in the direction of the core. In the less bright west hot spot we find 3.5 milligauss and even smaller values (2.2-2.7 milligauss) in the extended W lobe regions. The uncertainties are mainly due to the non-uniform spectrum present in this region. With these results the estimated radiative age of older emitting electrons is 3.0×10^3 yrs in the east lobe (near the core) and 4.5-4.9 $\times 10^3$ yrs in the northern region of the west lobe. An estimate of the uncertainty of these values is not obvious since errors are mainly model dependent.

7.3.4 Polarization

After removing the instrumental polarization we did not detect any polarized signal from the source. The 3σ upper limit on the polarized flux density is < 0.140 mJy/beam at 5 GHz. This limit corresponds to $< 0.3\%$ polarization at the brighter, eastern hot spot, to $< 0.6\%$ polarization at the core, and $< 3\%$ at typical locations in the lobes.

7.3.5 Variability

The sum of model-fit components in the two epochs is 1.21 and 1.24 Jy respectively, which gives an insignificant difference of just 2%. Given that many of the components are extended, such a small variation in the total flux density over 5 years seems reasonable. The core component is compact (size $\sim$ 0.81 mas) and could be more variable. In fact from the model-fit results (Table 7.1) the core varies from 20 $\pm$ 1 mJy in 1995 to 24 $\pm$ 1 mJy in 2000. Although this variation is only significant at the 3σ level, if it is real then it indicates a change by 20%. This variation is consistent with the limits on core variability implied by the integrated intensity observations of (Fassnacht & Taylor, 2001) from a small sample of CSOs studied over the course of eight months. Fassnacht & Taylor (2001) found the rms variation in the integrated flux density to be 0.7%. Assuming all that variation was due to the core component, and given an average core fraction of 0.03 (Taylor et al., 1996), leads to an estimate for the core variability in CSOs of less than 23%. Better limits on the variability of core components in CSOs will require VLBI monitoring campaigns, rather than low resolution studies only sensitive to the integrated flux density. The radio galaxy 4C 31.04 is an excellent candidate for such a study since the core is comparatively strong and isolated from nearby jet components.

7.4 Discussion

7.4.1 Ages of Compact Symmetric Objects

We derive the kinematic age of 4C 31.04 to be 550 years. This estimate is within the 300 to 1200 year range of ages found in the literature (Polatidis, 2002; Owsianik & Conway, 1998; Taylor et al., 2000). It is interesting to ponder the narrowness of this range. Even younger sources would need to be smaller, and/or have faster hot spot advance speeds. Currently there is a lower limit on the size of a source of a few mas ($\sim$ 10 pc) that we can readily classify as a CSO by identifying a core component between two hot spots. Assuming that the hot spot advance speed through the AGN environment is similar ($0.2\,c$) for an ultra-compact CSO (the denser environment on such small scales should make this a conservative assumption) then we can derive a lower limit to the age of observed CSOs of 100 years. There is also an observational upper limit on the size of CSOs. This is the size beyond which the CSO becomes difficult to observe with VLBI arrays since an interferometer is only sensitive to certain spatial frequencies. VLBI arrays have difficulty imaging components larger than about 40 beams, or sources lacking a strong compact component. By the time CSOs reach 1 kpc in size the lobes will be largely resolved out and the hot spots will be resolved to the extent that a direct detection is impossible without phase referencing. Velocity measurements of heavily resolved components are also much more difficult. These parameters give a conservative upper limit on the source age of 10000 years. Future advances in Space VLBI may discover radio sources younger than 100 years, and the E-MERLIN and EVLA projects may provide sufficient resolution and sensitivity to extend the upper boundary of sources for which we can determine a kinematic age. We also note that the advance speed of both east and west hot spots in 4C 31.04 at 0.33 $h_{65}^{-1}\,c$ are at the high end of those measured in CSOs to date, corresponding to a hot spot separation velocity of 0.39 $h_{100}^{-1}\,c$. This should be confirmed with future epochs.

It is of interest to compare the dynamic age of 550 years – derived from the study of hot spot velocities, to the radiative age – which we estimate from synchrotron losses in 4C 31.04 to be $\sim$ 4000 years. The radiative age is nearly an order of magnitude larger than the dynamic age estimate, indicating that some of our assumptions are in error.

First, we note that the kinematic age estimate rests on the assumption that the velocity has been constant over the lifetime of the source. Although Readhead et al. (1996b) argue that only mild evolution in velocity is likely, this assumption may not hold in 4C 31.04. As discussed in Sect. 7.4.2, there is evidence from the radio morphology of a strong interaction between the jet and the ISM. This could be making the jet wander around within the lobe, forming new hot spots which drill quickly out for some brief time before being shut off. Further suggestion that the kinematic age may be an underestimate comes from the west lobe dimension: the weakest detectable emission northward is about 60 mas which would require a lobe expanding at 0.41 c.

On the other hand, it is possible that the radiative age is overestimated by the equipartition field strength or the value of the critical frequency. While the 22 GHz data suggest that the value of the critical frequency is quite accurate, we note that the equipartition field could easily be higher if either $k > 1$ or $\phi < 1$. In this case the radiative age would be much more similar to the kinematic estimate; for instance $H_{\rm eq} \sim 6$ milligauss (given by $k = 20$ and $\phi = 0.7$) would yield $\sim$ 1000 years. Furthermore, this result was obtained assuming no energy losses due to Inverse Compton interactions. Even if scattering with the microwave background can be neglected with no harm, it is possible that in such a small source some interaction is present between relativistic electrons in the lobes and photons from the active core. The radiative age would then be smaller than calculated.

It is not easy to infer from the present data which estimate is the most reliable. We hope to address the question of the dynamic age with additional observations in the next years. Other studies of magnetic fields in CSOs would help to understand how correct are the assumptions going into the radiative age estimate. Also, high resolution low frequency data could help to estimate H from self-absorption analysis, while high frequency data will allow a better estimate of the critical frequency.

7.4.2 Morphology and interaction with ISM

The radio morphology of the two lobes is quite different. It is likely that their asymmetry is related to a slightly different ambient medium. In particular, the interaction between the relativistic jet and the ISM can lead to the formation of lobes of various morphologies.

According to computer simulations presented by Bicknell et al. (2003), the extended, low brightness morphology of the western lobe could be produced by a jet interacting with many ISM clouds. This interaction is not so strong as to destroy the jet but would cause: (1) the presence of a hot spot fainter than usual and (2) the spread of a large fraction of relativistic plasma carried by the jet and therefore the formation of a diffuse, faint lobe.

In the same scenario, the more compact and regular morphology of the eastern lobe suggests that it is undergoing less interaction with the ISM. The deep hole close to the hot spot becomes an even more interesting feature. Could it be due to foreground absorption or is it truly a large region in the lobe devoid of any radio emitting plasma? The steep spectral index of 1.7 ± 0.04 found from the spectral index image (Fig. 7.7), argues against foreground absorption by thermal electrons which would produce an inverted spectrum. This leaves us with a remarkable hole in the lobe. It would be interesting to search for the presence of dense molecular gas that might be impenetrable by the radio plasma.

7.4.3 Evolution of CSOs

Despite uncertainties and some discrepancy between kinematic and spectral age for 4C 31.04, our results clearly indicate that it is indeed a very young source. Most of the known Compact Symmetric Objects have been selected from flux limited samples, so that they are usually quite bright and they will likely evolve into FR II radio galaxies. It is interesting to ask what will be the fate of the weaker 4C 31.04, and try to learn more on the relation between 'child' and 'adult' stages of radio sources.

One of the problems with the youth scenario is given by the relative numbers of small sources (CSOs, CSS) and large classical double radio galaxies. This has been explained by models (e.g. Fanti et al., 1995) in which the total power P of the source decreases as a power law function of linear size LS: $P \propto (LS)^{-h}$. As a consequence of variations of external density and pressure, the index h is not very strictly constrained and it may actually change on different scales and for different sources.

If we roughly use $P \propto (LS)^{-0.5}$ as a law for radio power evolution (O'Dea, 1998), we find that 4C 31.04 will drop below the power of $10^{24.5}$ W/Hz as soon as it will be $\sim$40 times larger than its actual size. In other words, by the time 4C 31.04 will be 5 kpc large, its power will be similar to that of edge darkened FR I radio galaxies. Even if this threshold is actually not so sharp and the numbers vary, it is interesting to speculate that 4C 31.04 may have an FR I morphology in the future. In fact, based on pc-scale jet velocities and properties, Giovannini et al. (2001) argued that there are no significant differences between FR I and FR II radiogalaxies on pc-scales. It is then interesting to note that a possible future FR I radio galaxy now has the same edge brightened look of CSOs evolving into FR IIs. Thus, even in a completely different evolutionary stage, there would seem to be no difference on the small scale between FR Is and FR IIs. The discovery of other CSOs among samples of low-power sources is needed to better understand the evolution of low-power radio galaxies.

7.4.4 Lack of Polarization

Synchrotron emission is intrinsically polarized up to 70%, depending on the amount of order in the source magnetic fields (Burn, 1966). Why is there so little polarized emission from 4C 31.04 and other CSOs (Peck & Taylor, 2000)? From the H I observations we know that 4C 31.04 is viewed through a moderate density of atomic gas. If there is ionized gas present as well along with a magnetic field, then the radiation from 4C 31.04 that we observe could have been depolarized by a change in polarization angle within each 8 MHz IF, or by a gradient in the foreground Faraday screen. For bandwidth depolarization to be effective at 5 GHz requires RMs of 10^5

rad m^{-2}, while beam-width depolarization requires gradients in the RM of 300 rad m^{-2} mas^{-1} or more.

7.5 Conclusions

From the comparison of the two VLBI images at 5 GHz, a small but significant expansion appears to be present in the Compact Symmetric Object 4C 31.04. From the derived expansion rate and the current size of the source we calculate an age of 550 years. A somehow larger value of the age (3000 – 5000 yrs) is derived from spectral index analysis. Despite a significant difference, both results agree that the source is very young, as already demonstrated for other CSOs in the literature. However, the relatively high hot spots velocity and its low power make of 4C 31.04 a peculiar case among CSOs.

The discrepancy and uncertainty in the age estimates, the uncommon presence of a deep 'hole' in the East lobe, the detection and the variability of the compact core suggest that it may be worth observing this source again in the future. New VLBI observations will be of interest to look for free–free absorption at low frequency, to confirm the expansion, and to look for spectral aging at high frequency.

Conclusions

In this thesis we have studied the properties of various compact radio loud Active Galactic Nuclei (AGN), focusing on the lowest power sources. In particular, we have presented a new sample of low redshift BL Lac objects with no selection bias on their nuclear radio properties and high quality Hubble Space Telescope optical images. Besides the study of the sample properties, we have analysed in detail two peculiar sources: the outstanding TeV BL Lac object Markarian 501 and the beautiful Compact Symmetric Object 4C 31.04. All the studies are based on new radio data, obtained with various interferometers, including VLBI arrays with milliarcsecond resolution: the Very Long Baseline Array, the European VLBI Network, and the VLBI Space Observatory Program.

A sample of nearby BL Lacs

We have selected a sample of nearby ($z < 0.2$) BL Lacs, in order to extend the current knowledge to low redshift, weak objects and to test the unified scheme in the low luminosity range. Hubble Space Telescope observations have been previously presented, as well as radio observations of a few well known objects. After collecting the main results from the literature, we have obtained new observations, resulting in a complete set of parsec and kiloparsec scale images of all the objects in the sample. From the analysis of these data, we obtain the following main conclusions:

- **Morphology on kpc scale:** objects are typically dominated by a compact core, although not as extremely as other brighter samples. The mean core dominance parameter is $\langle R \rangle \geq 3.2$. Therefore, the core is frequently associated to a resolved radio morphology, including halos, secondary components, and symmetric two-sided jets; this suggests that kiloparsec scale jets may have different properties, being either non-relativistic or still mildly relativistic in different sources. This suggests that the decrease in jet velocity is related to the ISM properties, which can vary among galaxies. Finally, a few objects show a Wide Angle Tail or Head Tail morphology, suggesting that they are radio galaxies belonging to galaxy cluster.

- **Morphology on parsec scale:** most of the arcsecond core flux density is present in our VLBA or EVN images, which implies that we have not missed considerable sub-arcsecond structure. The largest fraction of flux density is in a parsec scale core, occasionally associated to one-sided jets; many extremely weak objects possess however only the few mJy core. When a jet is present, it does not show evidence of large bending, although some remarkable exceptions do exist (see Markarian 501 below). The kiloparsec scale structure is also quite well aligned with the inner direction, which makes nearby BL Lacs quite different from, e.g., the objects in the 1 Jy sample.

- **Beaming factors:** radio emission presents the features characteristic of relativistic beaming; the study of core dominance, jet/counter-jet ratio, SSC model yields consistent results, with Doppler factors in the range $1 < \delta < 10$. We find one object with $\delta < 1$ and show that it is actually a misidentification. However, the required beaming is somehow smaller for the low redshift objects than for the more distant ones.

- **Parent population:** given the observed radio properties, we conclude that our BL Lacs are clearly aligned objects, as expected by the unified schemes. De-beaming the observed radio power, and considering isotropic properties such as the low frequency radio power and host galaxy properties, we do not find any difference with Fanaroff-Riley I radio galaxies. No FR II is allowed as the misaligned counterpart of a low redshift BL Lac.

- **HBL and LBL:** although our sample is mostly composed of High frequency peaked BL Lacs, it also contains seven Low frequency peaked objects, whose properties are slightly different; they are more powerful, core-dominated, and brighter. Under the assumption that all jets possess the same Lorentz factor $\Gamma = 5$, LBL need to be oriented at smaller viewing angles than HBL; by contrast, if we allow both Γ and θ to vary, we derive similar orientation and a difference in velocity: interestingly, LBL would have larger bulk velocities (up to $\Gamma \lesssim 7$) than HBL, including TeV sources ($\langle\Gamma\rangle \sim 3$). In both cases, the Doppler factor of BL Lacs is considerably smaller in radio jets than in the $\gamma-$ray emitting region.

Markarian 501

Markarian 501 is one of the most outstanding sources in our sample, for its extremely low redshift, TeV emission, misalignment between parsec and kiloparsec scale. We have studied this source in detail, considering new Space VLBI observations as well as collecting a large number of multi-frequency Earth-based VLBI experiments. The parsec scale properties of Markarian 501 suggest the following, interesting conclusions:

- **Motion of components:** similarly to what happens in other TeV sources, our large number of high resolution observations, separated by small time intervals, have shown that no superluminal pattern velocity is present in the parsec scale jet of Markarian 501.

- **Velocity structure:** as a matter of fact, our high frequency observations reveal that milliarcsecond size components are actually resolved into smaller compact regions blended together; the real jet structure appears limb-brightened from the very inner jet region: the transverse velocity structure (fast inner spine and slower external layer) necessary to account for this effect needs to develop on very small scale, if not to be intrinsic to the jet launch mechanism.

- **Viewing angle and Lorentz factor:** in order for the limb brightening to be visible, and from other observational constraints, we derive that the observing angle of the parsec scale jet can not be too small ($15^\circ < \theta < 25^\circ$); the viewing angle is probably smaller in the inner $\gamma-$ray region and we suggest a jet reorientation leading to the derived parsec scale θ. The Lorentz factor is larger in the inner spine than in the external layer; in any case, the jet is initially strongly relativistic ($\Gamma \sim 15$), slows down on scales ~ 100 mas but remains at least mildly relativistic.

4C 31.04

The Compact Symmetric Object 4C 31.04 is the first low power CSO in which it has been possible to measure hot spot advance velocity, moreover on a time baseline as short as five years. The resulting dynamic age of the source is ~ 550 years; although somehow discrepant from the spectral estimate of the age (3000-5000 years), this result supports the youth scenario for the explanation of the small size of CSO, even in a relatively low power range. Future developments of unified schemes will have to try and include age as a key parameter for comprehensive view of the radio loud Active Galactic Nuclei.

Acknowledgments

This research has made use of the NASA/IPAC Extragalactic Database (NED) which is operated by the Jet Propulsion Laboratory, Caltech, under contract with NASA and of NASA's Astrophysics Data System (ADS) Bibliographic Services. The National Radio Astronomy Observatory is operated by Associated Universities, Inc., under cooperative agreement with the National Science Foundation. The European VLBI Network is a joint facility of European, Chinese, South African and other radio astronomy institutes funded by their national research councils. MERLIN is a National Facility operated by the University of Manchester at Jodrell Bank Observatory on behalf of PPARC. We gratefully acknowledge the VSOP Project, which is led by the Japanese Institute of Space and Astronautical Science in cooperation with many organizations and radio telescopes around the world. This research has made use of the United States Naval Observatory (USNO) Radio Reference Frame Image Database (RRFID). This research has made use of data from the University of Michigan Radio Astronomy Observatory which is supported by funds from the University of Michigan.

Various collaborators have contributed to the results published in this thesis: first and foremost, the supervisor of this project, Prof. Gabriele Giovannini; then Greg B. Taylor, J.E. Conway, W.D. Cotton, P.G. Edwards, R. Falomo, L. Feretti, L. Lara, A.P. Marscher, J.R. Mattox, B.G. Piner, and T. Venturi.

This work was partly supported by the Italian Ministry for University and Research (MIUR) under grant COFIN 2001-02-8773. The material in Chapter 6 is based in part upon work supported by the U.S. National Science Foundation under Grant No. 0098579.

Desidero infine ringraziare in modo speciale tutti coloro che in vario modo hanno contribuito alla stesura di questa tesi: per primo, Gabriele Giovannini, che pazientemente mi ha guidato in questo lavoro e nella mia preparazione; i miei amici *e colleghi all'Istituto di Radioastronomia; in particolare Federica, che mi e' stata vicina in questi tre anni, non solo in ufficio ma anche nei divertimenti e nelle fantasticherie. Non so trovare le parole giuste per rendere grazie alla mia famiglia per tutto il sostegno e l'affetto che mi ha dato da sempre; spero di averla resa orgogliosa. Un grazie ancora piu' grande e' per Maria Teresa, che mi ha stimolato, sopportato, incoraggiato, sostenuto, sorriso e fatto sorridere; senza di lei, questa tesi sarebbe stata piu' povera... ed io ancor piu'.*

Bibliography

Aaron, S. 1999, ASP Conf. Ser. 159: BL Lac Phenomenon, 427

Antonucci, R. R. J. & Ulvestad, J. S. 1985, ApJ, 294, 158

Appl, S., Sol, H., & Vicente, L. 1996, A&A, 310, 419

Barth, A. J., Ho, L. C., & Sargent, W. L. W. 2003, ApJ, 583, 134

Baum, S. A. et al. 1997, ApJ, 483, 178

Becker, R. H., White, R. L., & Edwards, A. L. 1991, ApJS, 75, 1

Becker, R. H., White, R. L., & Helfand, D. J. 1995, ApJ, 450, 559

Beckmann, V., Engels, D., Bade, N., & Wucknitz, O. 2003, A&A, 401, 927

Bettoni, D., Falomo, R., Fasano, G., & Govoni, F. 2003, A&A, 399, 869

Bicknell, G. V., Saxton, C. J., Sutherland, R. S., Midgley, S., & Wagner, S. J. 2003, New Astronomy Review, 47, 537

Brunetti, G., Cappi, M., Setti, G., Feretti, L., & Harris, D. E. 2001, A&A, 372, 755

Burn, B. F. 1966, MNRAS, 133, 67

Caccianiga, A., Maccacaro, T., Wolter, A., della Ceca, R., & Gioia, I. M. 1999, ApJ, 513, 51

Caccianiga, A. & Marchã, M. J. M. 2004, MNRAS, 348, 937

Cassaro, P., Stanghellini, C., Bondi, M., Dallacasa, D., della Ceca, R., & Zappalà, R. A. 1999, A&AS, 139, 601

Cassaro, P., Stanghellini, C., Dallacasa, D., Bondi, M., & Zappalà, R. A. 2002, A&A, 381, 378

Catanese, M. et al. 1998, ApJ, 501, 616

Chadwick, P. M. et al. 1999, ApJ, 513, 161

Chiaberge, M., Capetti, A., & Celotti, A. 1999, A&A, 349, 77

Chiaberge, M., Celotti, A., Capetti, A., & Ghisellini, G. 2000, A&A, 358, 104

Condon, J. J., Cotton, W. D., Greisen, E. W., Yin, Q. F., Perley, R. A., Taylor, G. B., & Broderick, J. J. 1998, AJ, 115, 1693

Conway, J. E. 1996 in The Second Workshop on Gigahertz Peaked Spectrum and Compact Steep Spectrum Radio Sources, ed. I. A. G. Snellen, R. T. Schilizzi, H. J. A. Rottgering and M. N. Bremer [Leiden Observatory], 198

Conway, J. E. 1999, New Astronomy Review, 43, 509

Conway, J. E. 2002, New Astronomy Review, 46, 263

Conway, J. E. & Wrobel, J. M. 1995, ApJ, 439, 98

Costamante, L. & Ghisellini, G. 2002, A&A, 384, 56

Cotton, W. D., Feretti, L., Giovannini, G., et al. 1995, ApJ, 452, 605

Cotton, W. D., Feretti, L., Giovannini, G., Lara, L., & Venturi, T. 1999, ApJ, 519, 108

Dallacasa, D. 2003, Publications of the Astronomical Society of Australia, 20, 79

de Ruiter, H. R., Parma, P., Fanti, C., & Fanti, R. 1990, A&A, 227, 351

Donato, D., Ghisellini, G., Tagliaferri, G., & Fossati, G. 2001, A&A, 375, 739

Donato, D., Gliozzi, M., Sambruna, R. M., & Pesce J. E. 2003, A&A, 407, 503

Douglas, J. N., Bash, F. N., Bozyan, F. A., Torrence, G. W., & Wolfe, C. 1996, AJ, 111, 1945

Edwards, P. G., Giovannini, G., Cotton, W. D., Feretti, L., Fujisawa, K., Hirabayashi, H., Lara, L., & Venturi, T. 2000, PASJ, 52, 1015

Edwards, P. G. & Piner, B. G. 2002, ApJ, 579, L67

Elvis, M., Plummer, D., Schachter, J., & Fabbiano, G. 1992, ApJS, 80, 257

Falomo, R., Pesce, J. E., & Treves, A. 1995, ApJ, 438, L9

Falomo, R., Scarpa, R., Treves, A., & Urry, C. M. 2000, ApJ, 542, 731

Falomo, R., Kotilainen, J. K., & Treves, A. 2002, ApJ, 569, L35

Falomo, R., Carangelo, N., & Treves, A. 2003, MNRAS, 343, 505

Falomo, R., Kotilainen, J. K., Carangelo, N., & Treves, A. 2003, ApJ, 595, 624

Fanaroff, B. L. & Riley, J. M. 1974, MNRAS, 167, 31P

Fanti, C., Fanti, R., Dallacasa, et al. 1995, A&A, 302, 317

Fassnacht, C. D., & Taylor, G. B. 2001, AJ, 122, 1661

Feretti, L., Giovannini, G., Gregorini, L., Parma, P., & Zamorani, G. 1984, A&A, 139, 55

Feretti, L., Perley, R., Giovannini, G., & Andernach, H. 1999, A&A, 341, 29

Ferrarese, L. & Merritt, D. 2000, ApJ, 539, L9

Fey, A. L. & Charlot, P. 1997, ApJS, 111, 95

Fey, A. L. & Charlot, P. 2000, ApJS, 128, 17

Ficarra, A., Grueff, G., & Tomassetti, G. 1985, A&AS, 59, 255

Fossati, G., Maraschi, L., Celotti, A., Comastri, A., & Ghisellini, G. 1998, MNRAS, 299, 433

Gabuzda, D. C., Pushkarev, A. B., & Cawthorne, T. V. 2000, MNRAS, 319, 1109

Gabuzda, D. C. & Cawthorne, T. V. 2003, MNRAS, 338, 312

Gabuzda, D. C. & Murray, E. 2004, in press (astro-ph/0309668)

Gebhardt, K. et al. 2000, ApJ, 539, L13

Ghisellini, G. & Celotti, A. 2001, A&A, 379, L1

Ghisellini, G., Celotti, A., Fossati, G., Maraschi, L. & Comastri, A. 1998, MNRAS, 301, 451

Ghisellini, G., Padovani, P., Celotti, A., & Maraschi, L. 1993, ApJ, 407, 65

Giommi, P., Menna, M. T., & Padovani, P. 1999, MNRAS, 310, 465

Giovannini, G. 1999 in *BL Lac Phenomenon*, ASP Conf. Ser., 159, 439

Giovannini, G. 2003, NewAR, 47, 551

Giovannini, G., Feretti, L., Gregorini, L., & Parma, P. 1988, A&A, 199, 73

Giovannini, G., Cotton, W. D., Feretti, L., Lara, L., & Venturi, T. 2001, ApJ, 552, 508

Gómez, J. & Marscher, A. P. 2000, ApJ, 530, 245

van Gorkom, J. H., Knapp, G. R., Ekers, R. D., et al. 1989, AJ, 97, 708

Green, R. F., Schmidt, M., & Liebert, J. 1986, ApJS, 61, 305

Gregory, P. C., & Condon, J. J. 1991, ApJS, 75, 1011-1291

Hartman, R. C. et al. 1999, ApJS, 123, 79

Hirabayashi, H. et al. 2000, PASJ, 52, 955

Hirabayashi, H. et al. 1998, Science, 281, 1825 and erratum 282, 1995

Holder, J. et al. 2003, ApJ, 583, L9

Homan, D. C., Ojha, R., Wardle, J. F. C., Roberts, D. H., Aller, M. F., Aller, H. D., & Hughes, P. A. 2001, ApJ, 549, 840

Horan, D. et al. 2002, ApJ, 571, 753

Horan, D. & Weekes, T. C. 2003, Proc. 2nd VERITAS Symposium on TeV Astrohysics of Extragalactic Sources (astro-ph/03100391)

Horan, D. et al. 2004, ApJ, 603, 51

Jaffe, W. J., & Perola, G. C. 1973, A&A, 26, 423

Jorstad, S. G., Marscher, A. P., Mattox, J. R., Wehrle, A. E., Bloom, S. D., & Yurchenko, A. V. 2001, ApJS, 134, 181

Junor, W., Biretta, J. A., & Livio, M. 1999, Nature, 401, 891

Katarzyński, K., Sol, H., & Kus, A. 2001, A&A, 367, 809

Kellermann, K. I., Vermeulen, R. C., Zensus, J. A., & Cohen, M. H. 1998, AJ, 115, 1295

Killeen, N. E. B., Bicknell, G. V., & Carter, D. 1986, ApJ, 309, 45

Kollgaard, R. I., Gabuzda, D. C., & Feigelson, E. D. 1996, ApJ, 460, 174

Kormendy, J. & Gebhardt, K. 2001, AIP Conf. Proc. 586: 20th Texas Symposium on relativistic astrophysics, 586, 363

Kuehr, H., Witzel, A., Pauliny-Toth, I. I. K., & Nauber, U. 1981, A&AS, 45, 367

Kubo, H., Takahashi, T., Madejski, G., Tashiro, M., Makino, F., Inoue, S., & Takahara, F. 1998, ApJ, 504, 693

Laing, R. A., Parma, P., de Ruiter, H. R., & Fanti, R. 1999, MNRAS, 306, 513

Laing, R. A. & Bridle, A. H. 2002a, MNRAS, 336, 328

Laing, R. A. & Bridle, A. H. 2002b, MNRAS, 336, 1161

Landt, H., Padovani, P., Perlman, E. S., Giommi, P., Bignall, H., & Tzioumis, A. 2001, MNRAS, 323, 757

Lara, L., Giovannini, G., Cotton, W. D., Feretti, L., Marcaide, J. M., Márquez, I., Taylor, G. B., & Venturi, T. 2002, New Astronomy Review, 46, 89

Laurent-Muehleisen, S. A., Kollgaard, R. I., Moellenbrock, G. A., & Feigelson, E. D. 1993, AJ, 106, 875

Laurent-Muehleisen, S. A., Kollgaard, R. I., Feigelson, E. D., Brinkmann, W., & Siebert, J. 1999, ApJ, 525, 127

Ledlow, M. J. & Owen, F. N. 1996, AJ, 112, 9

Lin, Y. C. et al. 1995, ApJ, 442, 96

Lister, M. L., Marscher, A. P., & Gear, W. K. 1998, ApJ, 504, 702

Ma, C. et al. 1998, AJ, 116, 516

Magorrian, J. et al. 1998, AJ, 115, 2285

Marchã, M. J., Caccianiga, A., Browne, I. W. A., & Jackson, N. 2001, MNRAS, 326, 1455

Marscher, A. P. 1987, Superluminal Radio Sources, 280

Marscher, A. P. 1999, APh, 11, 19

McLure, R. J. & Dunlop, J. S. 2002, MNRAS, 331, 795

Meier, D. L. 2003, New Astronomy Review, 47, 667

Morganti, R., Killeen, N. E. B., & Tadhunter, C. N. 1993, MNRAS, 263, 1023

Morganti, R., Oosterloo, T. A., Fosbury, R. A. E., & Tadhunter, C. N. 1995, MNRAS, 274, 393

Morris, S. L., Stocke, J. T., Gioia, I. M., Schild, R. E., Wolter, A., Maccacaro, T., & della Ceca, R. 1991, ApJ, 380, 49

Murgia, M., & Fanti, R. 1996, Rapporto Interno IRA, 228/96

Murgia, M., Fanti C., Fanti R., et al. 1999, A&A, 345, 769

Murphy, D. W., Browne, I. W. A., & Perley, R. A. 1993, MNRAS, 264, 298

Myers, S. T. et al. 2003, MNRAS, 341, 1

Narayan, R. & Yi, I. 1995, ApJ, 452, 710

Nass, P., Bade, N., Kollgaard, R. I., Laurent-Muehleisen, S. A., Reimers, D., & Voges, W. 1996, A&A, 309, 419

Nishiyama, T., et al. 2000, AIP Conf. Proc. 516, Proc. 26th International Cosmic Ray Conference, ed. B. L. Dingus, D. B. Kieda, & M. H. Salamon (Melville: AIP), 370

O'Dea, C. P. 1998, PASP, 110, 493

Orr, M. J. L. & Browne, I. W. A. 1982, MNRAS, 200, 1067

Owsianik, I., & Conway, J. E. 1998, A&A, 337, 69

Pacholczyk, A. G. 1970, Radio Astrophysics (San Francisco: Freeman & Co.)

Padovani, P. & Giommi, P. 1995, MNRAS, 277, 1477

Padovani, P. et al. 2001, MNRAS, 328, 931

Padovani, P., Perlman, E. S., Landt, H., Giommi, P., & Perri, M. 2003, ApJ, 588, 128

Padovani, P., Costamante, L., Giommi, P., Ghisellini, G., Celotti, A., & Wolter, A. 2004, MNRAS, 347, 1282

Peck, A. B., & Taylor, G. B. 2000, ApJ, 534, 90

Perlman, E. S. et al. 1996, ApJS, 104, 251

Perlman, E. S., Padovani, P., Giommi, P., Sambruna, R., Jones, L. R., Tzioumis, A., & Reynolds, J. 1998, AJ, 115, 1253

Perlman, E. S., Stocke, J. T., Conway, J., & Reynolds, C. 2001, ApJ, 122, 536

Pesce, J. E., Sambruna, R. M., Tavecchio, F., Maraschi, L., Cheung, C. C., Urry, C. M., & Scarpa, R. 2001, ApJ, 556, L79

Pian, E., Falomo, R., Ghisellini, G., Maraschi, L., Sambruna, R. M., Scarpa, R., & Treves, A. 1996, ApJ, 459, 169

Piccinotti, G., Mushotzky, R. F., Boldt, E. A., Holt, S. S., Marshall, F. E., Serlemitsos, P. J., & Shafer, R. A. 1982, ApJ, 253, 485

Pihlström, Y. M. 2001, Radio Studies of Circumnuclear Gas in Active Galaxies, Ph.D. Thesis, Chalmers University of Technology, Göteborg

Piner, B. G., Unwin, S. C., Wehrle, A. E., Edwards, P. G., Fey, A. L., & Kingham, K. A. 1999, ApJ, 525, 176

Piner, B. G. & Edwards, P. G. 2004, ApJ, 600, in press (astro-ph/0309547)

Polatidis, A., Conway, J. E., & Owsianik, I. 2002, in Proceedings of 6th EVN Symposium, edited by E. Ros, E.W. Porcas, A.P. Lobanov and J.A. Zensus, p. 139

Polatidis, A., & Conway, J. E. 2002, in The Third Workshop on Compact Steep Spectrum and GHz-Peaked Spectrum Radio Sources, PASA

Pollack, L. K., Taylor, G. B., & Zavala, R. T. 2003, ApJ, 589, 733

Punch, M. et al. 1992, Nature, 358, 477

Quinn, J. et al. 1996, ApJ, 456, L83

Readhead, A. C. S., Taylor, G. B., Xu, W., et al. 1996a, ApJ, 460, 612

Readhead, A. C. S., Taylor, G. B., Pearson, T. J., & Wilkinson, P. N. 1996b, ApJ, 460, 634

Rector, T. A., Stocke, J. T., Perlman, E. S., Morris, S. L., & Gioia, I. M. 2000, AJ, 120, 1626

Rector, T. A. & Stocke, J. T. 2001, AJ, 122, 565

Rector, T. A., Gabuzda, D. C., & Stocke, J. T. 2003, AJ, 125, 1060

Reid, R. I., Kronberg, P. P., & Perley, R. A. 1999, ApJS, 124, 285

Remillard, R., et al. 1999, unpublished

Rengelink, R. B., Tang, Y., de Bruyn, A. G., Miley, G. K., Bremer, M. N., Roettgering, H. J. A., & Bremer, M. A. R. 1997, A&AS, 124, 259

Rieger, F. M. & Mannheim, K. 2003, A&A, 397, 121

Salvati, M., Spada, M., & Pacini, F. 1998, ApJ, 495, L19

Scarpa, R., Urry, C. M., Falomo, R., Pesce, J. E., Webster, R., O'Dowd, M., & Treves, A. 1999, ApJ, 521, 134

Scarpa, R., Urry, C. M., Falomo, R., & Treves, A. 1999, ApJ, 526, 643

Scarpa, R., Urry, C. M., Falomo, R., Pesce, J. E., & Treves, A. 2000, ApJ, 532, 740

Schachter, J. F. et al. 1993, ApJ, 412, 541

Shen, Z.-Q. et al. 1998, AJ, 115, 1357

Shepherd, M. C., Pearson, T. J., & Taylor, G. B. 1994, BAAS, 26, 987

Shepherd, M. C., Pearson, T. J., & Taylor, G. B. 1995, BAAS, 27, 903

Slinglend, K., Batuski, D., Miller, C., Haase, S., Michaud, K., & Hill, J. M. 1998, ApJS, 115, 1 1

Snellen, I. & Schilizzi, R. 2002, NewAR, 46, 61

Stickel, M., Fried, J. W., Kuehr, H., Padovani, P., & Urry, C. M. 1991, ApJ, 374, 431

Stickel, M. & Kuehr, H. 1994, A&AS, 103, 349

Stirling, A. M. et al. 2003, MNRAS, 341, 405

Stocke, J. T., Morris, S. L., Gioia, I. M., Maccacaro, T., Schild, R., Wolter, A., Fleming, T. A., & Henry, J. P. 1991, ApJS, 76, 813

Tavecchio, F., Maraschi, L., & Ghisellini, G. 1998, ApJ, 509, 608

Tavecchio, F., Maraschi, L., Pian, E. et al. 2001, ApJ, 554, 725

Taylor, G. B. 2000, ApJ, 533, 95

Taylor, G. B., Readhead, A. C. S., & Pearson, T. J. 1996, ApJ, 463, 95

Taylor, G. B., Marr, J. M., Pearson, T. J. 2000, ApJ, 541, 112

Tingay, S. J. & Edwards, P. G. 2002, AJ, 124, 652

Ulvestad, J. S., Johnston, K. J. & Weiler, K. W. 1983, ApJ, 266, 18

Urry, C. M. & Padovani, P. 1995, PASP, 107, 803

Urry, C. M., Sambruna, R. M., Worrall, D. M., Kollgaard, R. I., Feigelson, E. D., Perlman, E. S., & Stocke, J. T. 1996, ApJ, 463, 424

Urry, C. M., Scarpa, R., O'Dowd, M., Falomo, R., Pesce, J. E., & Treves, A. 2000, ApJ, 532, 816

Van Breugel, W. & Schilizzi R. 1986, ApJ, 301, 834

Venturi, T. et al. 2001, A&A, 379, 755

Veron-Cetty, M.-P. & Veron, P. 1993, A&AS, 100, 521

Villata, M. & Raiteri, C. M. 1999, A&A, 347, 30

Voges, W. et al. 1999, A&A, 349, 389

Wardle, J. F. C., Moore, R. L., & Angel, J. R. P. 1984, ApJ, 279, 93

Willott, C. J., Rawlings, S., Blundell, K. M., & Lacy, M. 1999, MNRAS, 309, 1017

Wrobel, J. M. & Simon, R. S 1986, ApJ, 309, 593

Wu, X., Liu, F. K., & Zhang, T. Z. 2002, A&A, 389, 742

Zirbel, E. L. & Baum, S. A. 1995, ApJ, 448, 521